

Interfacial Behavior of Cholesterol, 7-Ketocholesterol and  $5\beta,6\beta$ -Epoxycholesterol in  
Phosphatidylcholine Monolayers

DISSERTATION

Presented in Partial Fulfillment of the Requirements for the Degree Doctor of Philosophy  
in the Graduate School of The Ohio State University

By

Dana-Marie Telesford, M.S.

Graduate Program in Chemistry

The Ohio State University

2014

Dissertation Committee:

Prof. Heather C. Allen, Advisor

Prof. Barbara E. Wyslouzil

Prof. Dennis Bong

Prof. Michael C. Ostrowski

Copyright by  
Dana-Marie Telesford  
2014

## ABSTRACT

Cholesterol (Chol) is the most ubiquitous sterol in various systems such as biomembranes, pulmonary surfactant, and marine aerosols. In biomembranes, the primary role of Chol is to modulate physico-chemical properties (i.e., fluidity, permeability, and mechanical strength). Another important function of Chol in biomembranes is to sequester saturated phospholipids into microdomains commonly referred to as lipid rafts. Many studies have placed an emphasis on elucidating these structures because of their ability, to some extent, to recruit specialized intramembraneous proteins. It is known that the ability of Chol to successfully perform all these functions hinges on its molecular structure. However, like any other unsaturated lipid, Chol is susceptible to auto-oxidation by reactive oxygen species to form oxidized derivatives or oxysterols. Not only is the hydrophilicity of the parent molecule increased, but also its volume, thereby affecting lipid/sterol interactions.

In the first part of this study, the interactions between Chol and two of its oxidized derivatives, 7-ketocholesterol (7-KChol) and  $5\beta,6\beta$ -epoxycholesterol ( $5,6\beta$ -EChol), with 1,2-dipalmitoyl-*sn*-glycero-3-phosphocholine (DPPC), a lipid prominent in biomembranes and pulmonary surfactant, were investigated by using compression isotherm measurements and Brewster angle microscopy (BAM) on mixed monolayers at

the air/water interface. The compression isotherms and BAM images revealed that each sterol exhibited different interfacial behavior. The experiments on mixed monolayer experiments also revealed differences with the sterols condensing abilities (attractive interactions), interfacial rigidity (hydrocarbon chain ordering), and domain morphology (phase separation). Chol demonstrated the greatest ability in condensing DPPC monolayers in comparison to oxysterols at low surface pressures (i.e., low lipid surface coverage), however, at higher surface pressures relevant to biomembranes, condensing abilities were markedly reduced. Also, both oxysterols were unable to rigidify DPPC monolayers with the same efficiency as Chol. Finally, BAM images showed that oxysterols were less effective in causing the phase separation of DPPC monolayers.

In the second part of this study, a more comprehensive approach was taken to understand how increasing the chain length of saturated phosphatidylcholines (C12 to C20-PCs) can affect their molecular-level interactions with Chol, 7-KChol and 5,6 $\beta$ -EChol. The results here show that the efficiency of PCs to form stable complexes with sterols is related to the hydrophobic mismatch between PC and sterols. Additionally, condensing abilities were shown to exhibit PC and sterol type dependency, however, Chol still demonstrated superiority in terms of rigidity. Furthermore, with the longest PC analyzed (C20-PC), the oxysterols demonstrated greater ability in fluidizing the monolayer.

In the third part of this study, vibrational sum frequency generation (VSFG) spectroscopy was used to obtain the pure spectra of all three sterols. The results here show that all sterols exhibited different spectra in the C-H stretching region. These results

were quite interesting because of the fact that while these modifications to the Chol molecule were not major, VSFG was sensitive enough to distinguish these subtle differences.

These findings have great significance for understanding if oxysterols can impact the proper functioning of membranes with respect to lipid raft promoting and fluidizing capabilities. Previous studies have indicated that the aqueous core of marine aerosols are coated with a thin layer of organic surfactants. The extent of surfactant packing on aerosols can affect their aging, reactivity, and reflectivity, and, in turn, influence atmospheric chemistry and climate change. Because these PC/oxysterols demonstrated reduced interfacial rigidity, one can infer that they can affect the atmospheric processing of aerosols.

## DEDICATION

*This dissertation is dedicated to my family and friends.*

## ACKNOWLEDGMENTS

In the writing of this dissertation I would like to thank various members in the Allen lab. First and foremost, I would like to thank my advisor Dr. Heather C. Allen for believing in me and providing words of encouragement when needed for the past five years. I would also like to thank my fellow colleagues in the Allen lab in particular, Dr. Dominique Verreault for his help in proofreading and making corrections to this dissertation. I would also like to thank Ms. Victoria Reick-Mitrisin for helping me acquire some of the experimental data that is presented here in this dissertation. In this dissertation, the VSFG data was collected and analyzed at the Pacific Northwest National Laboratory (PNNL) and used under the helpful guidance of Drs. Hongfei Wang and Li Fu. And finally, to my family for giving me the strength and courage to pursue a higher education and for all their love and support.

## VITA

May 12<sup>th</sup>, 1981 .....Born – Port-of-Spain, Trinidad & Tobago

2005-2009 .....B.S. University, Orangeburg, S.C.

2009-2012 .....M.S. Chemistry, The Ohio State University

2009 to present .....Graduate Teaching Associate, Department  
of Chemistry and Biochemistry, The Ohio  
State University – Columbus, Ohio, USA

2010 to present .....Graduate Research Assistant, Department of  
Chemistry and Biochemistry, The Ohio  
State University – Columbus, Ohio, USA

## Publications

- D. Telesford, D. Verreault, V. Reick-Mitrisin, H.C. Allen, Condensing and Ordering Effects of Cholesterol, 7-Ketocholesterol and  $5\beta,6\beta$ -Epoxycholesterol on DPPC, *under review* (2014).
- E. C. Griffith, R. J. Perkins, D. Telesford, E. M. Adams, L. Cwiklik, H. C. Allen, M. Roeselová, V. Vaida, Interaction of L-phenylalanine with a Phospholipid Monolayer at the Water-Air Interface, *under review* (2014).

## Field of Study

Major Field: Chemistry.

## TABLE OF CONTENTS

Abstract .....	ii
Dedication .....	v
Acknowledgments.....	vi
Vita.....	vii
Publications .....	vii
Field of Study .....	vii
Table of Contents .....	viii
List of Figures .....	xii
List of Tables .....	xix
List of Abbreviations and Symbols.....	xx
1. Chapter : Introduction.....	1
1.1 Cellular Membranes .....	2
1.2 Pulmonary Surfactant.....	11
1.3 Marine aerosols .....	13
1.4 Langmuir Monolayers .....	16
2. Chapter : Theoretical Background and Instrumentation.....	18
2.1 Surface Tensiometry theory .....	18

2.2 Surface Tensiometry Instrumentation .....	22
2.3 Brewster Angle Microscopy Theory .....	23
2.4 Brewster Angle Microscopy Instrumentation .....	30
2.5 Vibrational Sum Frequency Generation (VSFG) Spectroscopy Theory.....	32
2.6 Vibrational Sum Frequency Generation (VSFG) Instrumentation .....	34
3. Chapter : Experimental Methods.....	36
3.1 Methods.....	36
3.1.1 Compression isotherm measurements .....	36
3.1.2 Isotherm analysis .....	37
3.1.3 High-Resolution, Broad-Bandwidth Vibrational Sum Frequency Generation (HR-BB-VSFG) measurements were performed at the Pacific Northwest National Laboratory under the guidance of Hong-fei Wang and Li Fu. ....	39
3.1.4 Propagation of Error .....	40
4. Chapter :Condensing and Ordering Effects of Cholesterol, 7-Ketocholesterol and 5 $\beta$ ,6 $\beta$ -Epoxycholesterol on DPPC .....	42
4.1 Materials.....	43
4.2 Results.....	44
4.2.1 Pressure-area compression isotherms of sterols in mixed monolayers with DPPC .....	44
4.2.2 Interfacial compressibility modulus .....	50

4.2.3 Excess free energy of mixing .....	52
4.2.4 BAM images.....	53
4.3 Discussion .....	60
5. Chapter : Dependence on the Condensing and Ordering Effects on Fluid and Condensed Saturated Phosphatidylcholines in mixed films with Cholesterol, 7- Ketocholesterol and 5 $\beta$ ,6 $\beta$ -Epoxycholesterol.....	68
5.1 Materials.....	69
5.2 Results and Discussion. Part I.....	70
5.2.1 Surface Pressure-Area Isotherms of Pure DLPC, DMPC, and Sterols Monolayers .....	70
5.2.2 Condensing Effect .....	73
5.2.3 Interfacial Area Compressibility Modulus of DLPC, DMPC, Sterols, and their Mixtures.....	79
5.2.4 Excess Free Energy of Mixing of DLPC, DMPC, Sterols, and their Mixtures	85
5.2.5 BAM Images of DLPC, DMPC, Sterols, and their Mixtures.....	88
5.3 Results and Discussion. Part II.....	93
5.3.1 Surface Pressure-Area Isotherms of Pure DSPC, DAPC, and their Mixtures with Sterols .....	93
5.3.2 Condensing Effect .....	95
5.3.3 Interfacial Area Compressibility Modulus of DSPC, DAPC, Sterols, and their Mixtures.....	98

5.3.3 Excess Free Energy of Mixing of DSPC, DAPC, Sterols, and their Mixtures	104
5.4 Conclusions .....	107
6. Chapter : High-Resolution Broad-Bandwidth VSFG spectroscopy of Pure Cholesterol, 7-Ketocholesterol and 5 $\beta$ ,6 $\beta$ -Epoxycholesterol Monolayers at the Air/Water Interface .....	109
6.1 Materials.....	111
6.2 Results and Discussion.....	111
6.2.1 VSFG Spectra of Pure Sterol Monolayers.....	111
7. Chapter : Conclusions and Implications .....	120
References.....	123
Appendix.....	134
Appendix A BAM Images of Mixed DPPC/Sterols Monolayers .....	134
Appendix B BAM Images of Mixed DLPC and DMPC/5,6 $\beta$ -EChol Monolayers....	137

## LIST OF FIGURES

Figure 1.1	Illustration of the complex structure of a cellular membrane. <sup>39</sup> .....	7
Figure 1.2	Chemical structures of phospholipids commonly found in eukaryotic biological membranes. <sup>40</sup> .....	8
Figure 1.3	Chemical structures of (A) DLPC (12C), (B) DMPC (14C), (C) DPPC (16C), (D) DSPC (18C)and (E) DAPC (20C) .....	9
Figure 1.4	Chemical structures of (A) Chol, (B) 7-KChol, and (C) 5,6 $\beta$ -EChol. ....	10
Figure 1.5	Generalized illustration of the processes that govern heterogeneous radical uptake by an aerosol particle. <sup>82</sup> .....	15
Figure 2.1	Liquid column made of two phases g and l .....	19
Figure 2.2	Reflectance of <i>p</i> -polarized light beam incident at the Brewster angle at the bare and monolayer-covered air/water interfaces. The multiple reflections in the lipid monolayer are not shown for clarity. ....	25
Figure 2.3	(A) Reflectance of <i>p</i> -polarized light beam incident at the Brewster angle at the bare and monolayer-covered air/water interfaces, (B) change and (C) relative change in reflectance of the air/water interface due to the presence of a lipid monolayer. The parameters used for the calculations were $n_a = 1.00$ , $n_l = 1.5$ , $n_w = 1.33$ , and $\lambda = 633$ nm. The inset shows the minimal <i>but non-zero p</i> -reflectance at the neat and monolayer-covered air/water interfaces. ....	29

Figure 2.4	Image of the Brewster angle microscope setup and KSV Langmuir trough. .	32
Figure 4.1	Compression isotherms of pure Chol, 7-KChol, and 5,6 $\beta$ -EChol monolayers. ....	47
Figure 4.2	Compression isotherms of (A) Chol, (B) 7-KChol, and (C) 5,6 $\beta$ -EChol mixed with DPPC monolayers.....	48
Figure 4.3	Variations of mean molecular area with sterol composition for (A) Chol, (B) 7-KChol, and (C) 5,6 $\beta$ -EChol in binary mixed DPPC monolayers.....	49
Figure 4.4	Variations of monolayer compressibility modulus with (A–C) surface pressure and (D–F) sterol composition for (A, D) Chol, (B, E) 7-KChol, and (C, F) 5,6 $\beta$ -EChol in binary mixed DPPC monolayers. The compressibility data were calculated from the compression isotherms in Fig. 4.2. The position of the LE-LC phase transition in the compressibility plots is indicated by an arrow.....	51
Figure 4.5	Variations of excess free energy of mixing with sterol composition for (A) Chol, (B) 7-KChol, and (C) 5,6 $\beta$ -EChol in binary mixtures with DPPC. (D) Excess free energy of mixing values for Chol, 5,6 $\beta$ -EChol and 7-KChol at 30 and 40 mN/m. ....	53
Figure 4.6	BAM images of pure (A) DPPC, (B) Chol, (C) 7-KChol, and (D) 5,6 $\beta$ -EChol monolayers at different stages of compression. Numbers in the lower left and upper right corners indicate the mean molecular area and the surface pressure, respectively. ....	56

Figure 4.7	BAM images of DPPC/sterol monolayers with (A) $X_{\text{sterol}} = 0.05$ and (B) $X_{\text{sterol}} = 0.3$ at different stages of compression. Numbers in the lower left and upper right corners indicate the mean molecular area and the surface pressure, respectively. ....	59
Figure 5.1	Compression isotherms of (A) Chol, (B) 7-KChol, (C), 5,6 $\beta$ -EChol mixed with DLPC monolayers. Compression isotherms of (D) Chol, (E) 7-KChol, (F), 5,6 $\beta$ -EChol mixed with DMPC monolayers. ....	73
Figure 5.2	Excess molecular area with sterol composition for (A) Chol, (B) 7-KChol, and (C) 5,6 $\beta$ -EChol mixed with DLPC monolayers. Excess molecular area with sterol composition for (D) Chol, (E) 7-KChol, and (F) 5,6 $\beta$ -EChol mixed with DMPC monolayers. ....	77
Figure 5.3	Partial molecular area with sterol composition for (A) Chol, (B) 7-KChol, and (C) 5,6 $\beta$ -EChol mixed with DLPC monolayers. Partial molecular area with sterol composition for (D) Chol, (E) 7-KChol, and (F) 5,6 $\beta$ -EChol mixed with DMPC monolayers. ....	79
Figure 5.4	Variations of monolayer compressibility modulus with (A–C) surface pressure and (D–F) sterol composition for (A and D) Chol, (B and E) 7-KChol, and (C and F) 5,6 $\beta$ -EChol mixed with DLPC monolayers. The compressibility data was calculated from the compression isotherms shown in Fig. 5.1. ....	82
Figure 5.5	Variations of monolayer compressibility modulus with (A–C) surface pressure and (D–F) sterol composition for (A and D) Chol, (B and E) 7-KChol, and (C and F) 5,6 $\beta$ -EChol mixed with DMPC monolayers. The compressibility data was calculated from the compression isotherms shown in Fig. 5.1. ....	83

Figure 5.6	Variations of excess free energy of mixing of sterol composition for (A) Chol, (B) 7-KChol, and (C) 5,6 $\beta$ -EChol mixed with DLPC monolayers. Variations of excess free energy of mixing of sterol composition for (D) Chol, (E) 7-KChol, and (F) 5,6 $\beta$ -EChol mixed with DMPC monolayers. ....	84
Figure 5.7	BAM images of DLPC and DLPC/Chol monolayers with $X_{\text{Chol}} = 0.3\text{--}0.7$ and Chol at different stages of compression. Numbers in the lower left and upper right corners indicate the mean molecular area and the surface pressure, respectively. ....	89
Figure 5.8	BAM images of DLPC and DLPC/7-KChol monolayers with $X_{7\text{-KChol}} = 0.3\text{--}0.7$ and 7-KChol at different stages of compression. Numbers in the lower left and upper right corners indicate the mean molecular area and the surface pressure, respectively. ....	90
Figure 5.9	BAM images of DMPC and DMPC/Chol monolayers with $X_{\text{Chol}} = 0.3\text{--}0.5$ and Chol at different stages of compression. Numbers in the lower left and upper right corners indicate the mean molecular area and the surface pressure, respectively. ....	91
Figure 5.10	BAM images of DMPC and DMPC/7-KChol monolayers with $X_{7\text{-KChol}} = 0.3\text{--}0.5$ and Chol at different stages of compression. Numbers in the lower left and upper right corners indicate the mean molecular area and the surface pressure, respectively. ..	92
Figure 5.11	Compression isotherms of (A) Chol, (B) 7-KChol, (C), 5,6 $\beta$ -EChol mixed with DSPC monolayers. Compression isotherms of (D) Chol, (E) 7-KChol, (F), 5,6 $\beta$ -EChol mixed with DAPC monolayers. ....	94
Figure 5.12	Excess molecular area with sterol composition for (A) Chol, (B) 7-KChol, and (C) 5,6 $\beta$ -EChol mixed with DSPC monolayers. Excess molecular area with sterol	

composition for (D) Chol, (E) 7-KChol, and (F) 5,6 $\beta$ -EChol mixed with DAPC monolayers. ....	97
Figure 5.13 Partial molecular area with sterol composition for (A) Chol, (B) 7-KChol, and (C) 5,6 $\beta$ -EChol mixed with DSPC monolayers. Partial molecular area with sterol composition for (D) Chol, (E) 7-KChol, and (F) 5,6 $\beta$ -EChol mixed with DAPC monolayers. ....	98
Figure 5.14 Variations of monolayer compressibility modulus with (A–C) surface pressure and (D–F) sterol composition for (A and D) Chol, (B and E) 7-KChol, and (C and F) 5,6 $\beta$ -EChol mixed with DSPC monolayers. The compressibility data was calculated from the compression isotherms shown in Fig. 5.11. ....	102
Figure 5.15 Variations of monolayer compressibility modulus with (A–C) surface pressure and (D–F) sterol composition for (A and D) Chol, (B and E) 7-KChol, and (C and F) 5,6 $\beta$ -EChol mixed with DAPC monolayers. The compressibility data was calculated from the compression isotherms shown in Fig. 5.11. ....	103
Figure 5.16 Variations of excess free energy of mixing of sterol composition for (A) Chol, (B) 7-KChol, and (C) 5,6 $\beta$ -EChol in binary mixtures with DSPC. Variations of excess free energy of mixing of sterol composition for (D) Chol, (E) 7-KChol, and (F) 5,6 $\beta$ -EChol in binary mixtures with DAPC. ....	106
Figure 6.1 VSFG spectra of pure Chol monolayers at the air/water interface. ....	113
Figure 6.2 VSFG spectra of pure 5,6 $\beta$ -EChol monolayers at the air/water interface. ....	113
Figure 6.3 VSFG spectra of pure 7-KChol monolayers at the air/water interface. ....	114

Figure 6.4	Comparison of the <i>ssp</i> VSG spectra of pure Chol, 7-KChol, and 5,6 $\beta$ -EChol at the air/water interface. ....	118
Figure 6.5	The methyl group tilt angle of sterol ( $\theta_{\text{CH}_3}$ ) is defined as the angle between the surface normal and the vector <b>T</b> joining C3 to C17 for (A) Chol, (B) 7-KChol, and (C) 5,6 $\beta$ -EChol.....	119
Figure 6.6	The tilt angle of the molecular plane formed by the steroid nucleus relative to the surface normal.....	119
Figure A.1	BAM images of a DPPC monolayer mixed with Chol at different stages of compression. Numbers in the lower left and upper right corners indicate the mean molecular and the surface pressure, respectively.....	127
Figure A.2	BAM images of a DPPC monolayer mixed with 7-KChol at different stages of compression. Numbers in the lower left and upper right corners indicate the mean molecular and the surface pressure, respectively.....	128
Figure A.3	BAM images of a DPPC monolayer mixed with 5,6 $\beta$ -EChol at different stages of compression. Numbers in the lower left and upper right corners indicate the mean molecular and the surface pressure, respectively.....	129
Figure B.1	BAM images of DLPC and DLPC/5,6 $\beta$ -EChol monolayers with $X_{5,6\beta\text{-EChol}} = 0.3\text{--}0.5$ and Chol at different stages of compression. Numbers in the lower left and upper right corners indicate the mean molecular area and the surface pressure, respectively.....	130
Figure B.2	BAM images of DMPC and DMPC/5,6 $\beta$ -EChol monolayers with $X_{5,6\beta\text{-EChol}} = 0.3\text{--}0.5$ and Chol at different stages of compression. Numbers in the lower left and	

upper right corners indicate the mean molecular area and the surface pressure,  
respectively.....131

## LIST OF TABLES

Table 6.1	Peak frequencies and spectral assignment of VSFG spectra of Chol, 7-KChol, and 5,6 $\beta$ -EChol monolayers at the air/water interface. <sup>154, 156, 157</sup> .....	114
Table 6.2	Sterol CH <sub>3</sub> groups and sterol molecule tilt angles. Parentheses indicate extrapolated values.....	118

## LIST OF ABBREVIATIONS AND SYMBOLS

### Abbreviations

AFM	atomic force microscopy
ARDS	acute respiratory distress syndrome
BAM	Brewster angle microscopy
CCD	charge-coupled device
CF	chrome-free
Chol	cholesterol
DAPC	1,2-dimyristoyl- <i>sn</i> -glycero-3-phosphocholine
DLPC	1,2-dilauroyl- <i>sn</i> -glycero-3-phosphocholine
DMPC	1,2-dimyristoyl- <i>sn</i> -glycero-3-phosphocholine
DPPC	1,2-dipalmitoyl- <i>sn</i> -glycero-3-phosphocholine
DSC	differential scanning calorimetry
DSPC	1,2-distearoyl- <i>sn</i> -glycero-3-phosphocholine
FR	Fermi resonance
G	gas
5,6 $\beta$ -EChol	5 $\beta$ ,6 $\beta$ -epoxycholesterol
IR	infrared
7-KChol	7-ketocholesterol
LC	liquid-condensed
LE	liquid-expanded
MMA	Mean molecular area
NA	numerical aperture

NSOM	near-field scanning optical microscopy
PC	phosphatidylcholine
PS	pulmonary surfactant
RNS	reactive nitrogen species
ROS	reactive oxygen species
S	solid
SNR	signal-to-noise ratio
SSML	sea surface microlayer
VIS	visible

## Symbols

$\gamma$	surface tension
$\gamma_0$	surface tension of the subphase (water or aqueous solution)
$\gamma_s$	surface tension of the subphase covered with surfactant
$\lambda$	wavelength
$\Pi$	surface pressure
$\theta_i$	incident angle
$\theta_{i,B}$	Brewster angle
$\theta_r$	reflected angle
$\theta_t$	transmitted angle
$\rho_p$	density of plate
$\rho_w$	density of subphase (water or aqueous solution)
$\omega$	frequency
$\sigma_x^2$	variance
$A$	area, molecular area
$A_{PC}^*$	partial molecular area
$c$	speed of light
$E$	total internal energy
$E^{(g)}$	internal energy of phase $g$
$E^{(l)}$	internal energy of phase $l$
$E^{(g/l)}$	surface excess internal energy
$k_B$	Boltzmann constant
$l$	liquid phase
$L$	length of plate

$n$	refractive index
$n_i$	refractive index of the incident medium
$n_t$	refractive index of the transmitted medium
$r^p$	$p$ -polarized Fresnel reflection coefficient
$r^s$	$s$ -polarized Fresnel reflection coefficient
$R^p$	$p$ -polarized reflectance
$R^s$	$s$ -polarized reflectance
$t^p$	$p$ -polarized Fresnel transmission coefficient
$t^s$	$s$ -polarized Fresnel transmission coefficient
$T$	temperature (absolute), thickness of plate
$V$	volume

## 1. Chapter : Introduction

The motivation behind this study is to provide a better understanding of molecular-level interactions of cholesterol (Chol) and some of its oxidized derivatives (or oxysterols) mixed with physiologically-relevant phospholipid monolayers, specifically phosphatidylcholines (PCs), at the air/water interface. In achieving this goal, this dissertation thoroughly examines the presence of condensing, ordering, and stability effects, as well as changes in domain morphology caused by these sterols when mixed PC monolayers of varying saturated acyl chain lengths. The results shown in this work were obtained by using a combination of compression isotherm measurements on a Langmuir trough and Brewster angle microscopy (BAM). Studies involving Langmuir monolayers have been proven to be quite successful in mimicking biomembranes, where physiologically relevant surface pressures ( $\Pi \geq 30$  mN/m) are easily attained.<sup>1 2</sup> At the surface of an alveolus, pulmonary surfactant exists as a monolayer and are known to reduce surface tension forces to very low values. Finally, lipids on the sea surface microlayer (SSML) have been identified at surfaces of aerosols and may influence atmospheric chemistries. Studies that focus on phospholipid/sterol interactions at the air/aqueous interface are therefore of the utmost importance to biomembranes, pulmonary surfactant and environmental systems and many others. The introduction of this

dissertation, therefore serves as a brief summary of many lipid-rich systems where fundamental studies on aqueous surfaces are quite informative.

## 1.1 Cellular Membranes

Biological membranes (biomembranes) are complex structures with a wide array of lipids and proteins that are arranged in an asymmetric bilayer (Fig. 1.1).<sup>3, 4</sup> The lipid constituents are quite diverse because of their varying chemical structures and different degrees of polarity as they can either be nonpolar or amphiphilic (i.e., containing both polar and nonpolar parts). The predominant types of lipids in biomembranes are phospholipids and sphingolipids. Phospholipids are composed of a glycerol backbone where two long fatty acyl chains are esterified at the C-1 and C-2 positions and a negatively-charged phosphate group that is esterified at the C-3 position (Fig. 1.2). In biomembranes, usually two long fatty acids chains are attached to the glycerol backbone with approximately the same length, however, difference do arise with respect to their relative saturation levels. Typically, the fatty acid chain length in eukaryotes lies between 12 and 20 carbon atoms, with 16–18 being the most common (Fig 1.3).<sup>5</sup> On the phosphate group, different polar moieties can be attached that contain a variety of chemical groups. In eukaryotic organisms, PCs are the major phospholipid constituent with more than 50% of total membrane phospholipids.<sup>6</sup> In PCs, a positively-charged choline group is attached to the phosphate group by a phosphodiester bond. Both phosphate and choline groups collectively result in PC being a zwitterionic molecule at

physiologically-relevant pH. In biomembranes, PCs are required to maintain membrane structure.<sup>6, 7</sup>

Another essential constituent of biomembranes are sterols. Sterols are abundant in the plasma membranes of eukaryotes and are essential for proper membrane function.<sup>6, 8</sup> Chol is the most abundant sterol in eukaryotic cell membranes and can amount to as much as 30–40 mol % of the total lipid fraction.<sup>6</sup> Because of its relatively high levels, Chol plays a key role in modulating some important physico-chemical properties of cellular membranes including fluidity, permeability, and mechanical strength. However, one key structural role of Chol concerns its involvement in the formation of microdomains such as lipid rafts. Lipid rafts are enriched in sphingolipids as well Chol, and are believed to sequester and regulate the function of various intramembraneous proteins.<sup>9, 10</sup> These properties, in turn, affect many vital cellular processes such as molecular trafficking, cell signaling and proliferation.<sup>10, 11, 12, 13</sup> Even though Chol plays such an essential role in cells, its presence in excess concentrations is known to be a factor in the onset of atherosclerosis.<sup>10, 14</sup> This process occurs as Chol was shown to aggregate in plasma membranes and form monohydrate crystals.<sup>15</sup> However, the nucleation mechanism by which this aggregation occurs is not well understood.

A considerable amount of research has been devoted towards understanding Chol and its interactions with other lipid components in biomembranes as well as in simplified model membrane systems. Model membrane systems consisting of saturated sphingolipids and phospholipids with sterols have proven invaluable in gaining insight into membrane lipid interactions. Among these phospholipids, saturated chain PCs and

their interactions with Chol have been extensively studied in model bilayers and monolayers with various computational and experimental methods.<sup>16, 17, 18, 19</sup> While sphingolipids are necessary for raft formation, saturated PCs can mimic some of their structural properties by sharing similar phosphorylcholine headgroup and saturated tails.<sup>1</sup> In all the PCs, dipalmitoylphosphatidylcholine (DPPC) has been a widely used model lipid in many studies because of its prevalence in biological membranes and pulmonary surfactant.<sup>20</sup> Model membranes studies with DPPC and other saturated PCs have revealed that the incorporation of Chol into a monolayer leads to a reduction in the mean molecular area occupied by the lipids, a phenomenon commonly referred to as the “condensing effect”. This also increases the conformational ordering of the lipid acyl chains that then leads to an enhanced packing efficiency modulated by Chol. Both condensing and ordering effects attributed to Chol are highly dependent upon its molecular structure therefore small modifications in the latter can have implications for the interactions with lipid and protein components in biomembranes.<sup>21,22</sup>

Oxidized derivatives of Chol or oxysterols are the results of modifications to the molecular structure of Chol that contain an additional oxygen atom in the form of a ketone, hydroxyl, hydroperoxy, or epoxy group.<sup>23</sup> The additional oxygen moiety not only increases the hydrophilicity of oxysterols in comparison to Chol, but it can also alter their three-dimensional (3D) shape.<sup>24</sup> Previous studies on the effects of oxysterols in membrane systems have demonstrated that they exhibit weaker membrane condensing and ordering abilities than Chol and therefore have reduced capabilities to promote lipid raft formation.<sup>25, 26, 27, 28</sup>

The presence of oxysterols in biomembranes has been known for decades, but it is only recently that their role as biomarkers of cellular oxidative stress has been recognized.<sup>29, 30</sup> Chol in biomembranes is susceptible to oxidation via enzymatic and non-enzymatic (auto-oxidation) pathways to form oxysterols.<sup>22</sup> The structural parts of Chol that are easily oxidized are the double bond between C5 and C6 and the vinylic methylene group at C7.<sup>30</sup> In humans, 7-ketocholesterol (7-KChol) is primarily formed via the auto-oxidation pathway of Chol at the C7 position.<sup>31, 32</sup> It is also the major oxysterol species in oxidized low-density lipids (LDL) and atherosclerotic plaques, and has been implicated in neurodegenerative diseases, apoptosis in various cells types, and the formation of crystalline domains in the aortic muscle cells.<sup>31, 33, 34, 35</sup> Another oxysterol, 5 $\beta$ ,6 $\beta$ -epoxycholesterol (5,6 $\beta$ -EChol), is formed via the auto-oxidation pathway at the C5-C6 double bond of the  $\beta$ -face of the steroid backbone.<sup>36</sup> Previous studies have suggested that 5,6 $\beta$ -EChol might be involved in several human pathologies which include diabetes, Alzheimer's disease, reproductive disorders, and cancer.<sup>37</sup> In an *in vitro* study by Pulfer and co-workers, 5,6 $\beta$ -EChol was also identified as one of the major end products formed from the oxidation by ozone of Chol present in lung surfactant.<sup>38</sup>

To understand how 7-KChol and 5,6 $\beta$ -EChol can have differing interactions with phospholipids relative to Chol, it is important to look at structural differences and similarities. Chol has four fused rings designated A, B, C and D (steroid nucleus), a 3 $\beta$ -OH group, a double bond between C5 and C6, and an isooctyl side chain at C17 (Fig. 1.4A).<sup>6, 10</sup> The steroid nucleus is planar and rigid, however, the isooctyl hydrocarbon chain is quite flexible.<sup>8</sup> On the  $\beta$ -face of Chol there are two methyl groups at C10 and

C13 that make this side of the molecule somewhat “rough”. The molecular structure of 7-KChol is quite similar to Chol as the planarity of the A and B rings is preserved; however, differences arise with respect to the additional ketone group at C7 (Fig. 1.4B). With regards to 5,6 $\beta$ -EChol, the molecular structure differs from Chol as there is no double bond between C5 and C6 and also by the presence of an epoxy group that projects out of the  $\beta$ -face of the steroid ring (Fig.1.4C). In addition, the absence of the double bond between C5 and C6 in 5,6 $\beta$ -EChol destroys the planarity of the A and B rings.<sup>21</sup> Typically, the 3 $\beta$ -OH group of the sterols prefers to reside closer to the phospholipid ester carbonyl group and the aqueous subphase, whereas the steroid nucleus remains embedded in the hydrophobic core of the phospholipid tails.<sup>10</sup> Earlier studies have shown that raft promoting abilities of oxysterols are dependent on the chemical structure and position of the oxygen moiety within the molecular structure of Chol.<sup>27, 28</sup> Therefore in depth studies are required to fully understand how different oxysterols can impact membrane function.

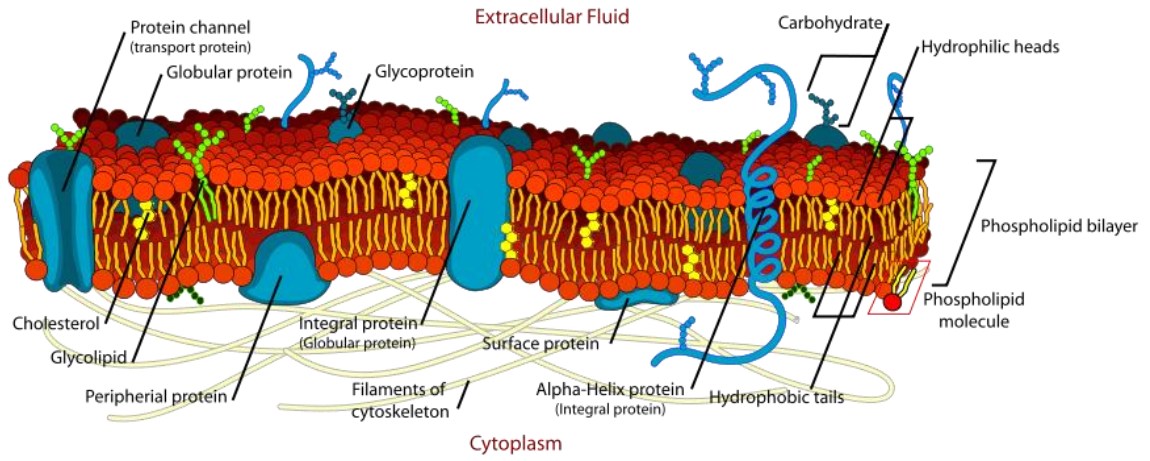


Figure 1.1 Illustration of the complex structure of a cellular membrane.<sup>39</sup>

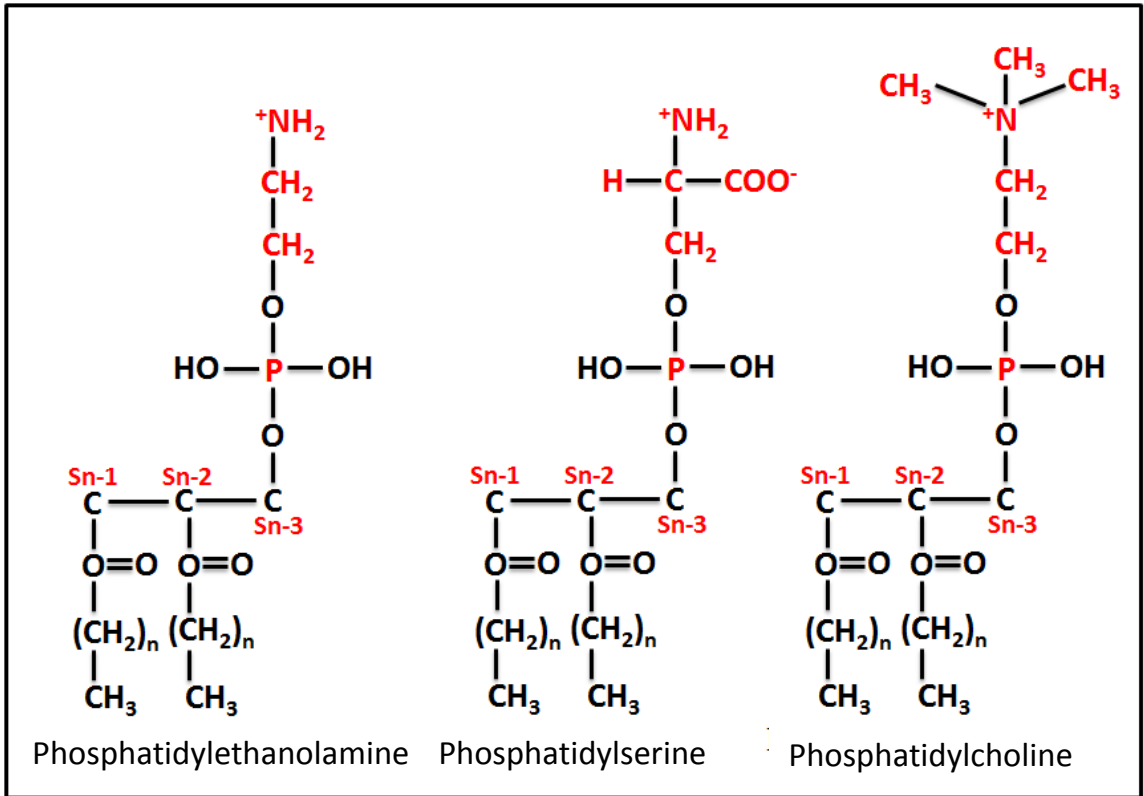


Figure 1.2 Chemical structures of phospholipids commonly found in eukaryotic biological membranes.<sup>40</sup>

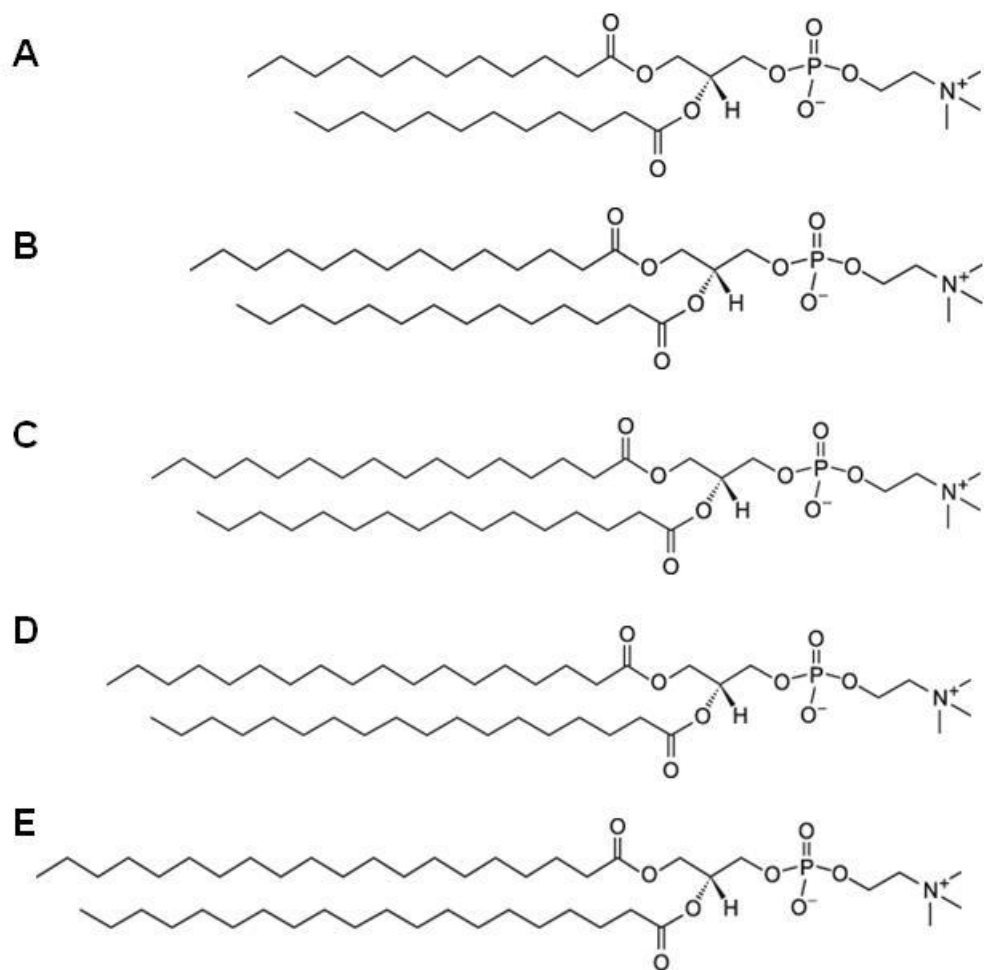


Figure 1.3 Chemical structures of (A) DLPC (12C), (B) DMPC (14C), (C) DPPC (16C), (D) DSPC (18C) and (E) DAPC (20C)

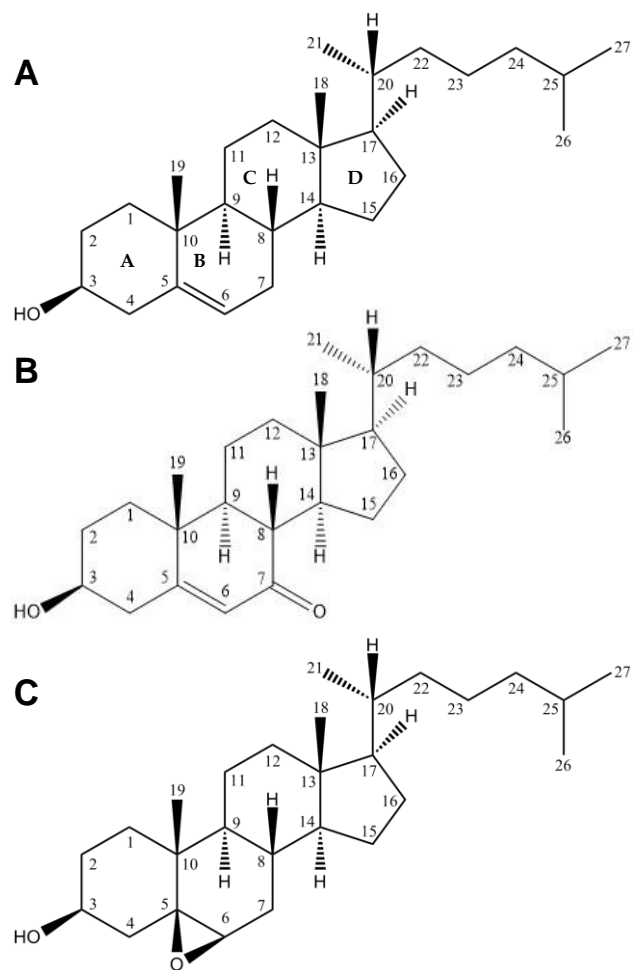


Figure 1.4 Chemical structures of (A) Chol, (B) 7-KChol, and (C) 5,6 $\beta$ -EChol.

## 1.2 Pulmonary Surfactant

The air/aqueous interface of mammalian lungs contains a complex mixture of lipids and proteins collectively called pulmonary surfactant (PS).<sup>41, 42, 43, 44</sup> PS is required to reduce surface tension forces at the air/aqueous interface of alveoli to very low values (~1 mN/m), thereby facilitating the breathing process and preventing the alveoli from collapsing during the expiration phase.<sup>45, 46, 47 48, 49</sup>

The composition of PS is ~90 % lipids and ~10 % proteins by weight, however, the most prevalent lipid constituent has a PC headgroup.<sup>42</sup> The fatty acid component of the PC can be saturated or unsaturated as well as having different acyl chain lengths. The dominant lipid component in PS is DPPC, which has two 16 carbons fatty acid chains. This molecule is of absolute necessity in PS as it is the only lipid that can lower surface tension to near zero values in a highly compressed state.<sup>50</sup> While the strength of DPPC lies in its ability to lower surface tension forces, its weak point is its inability to absorb or respread at the air/aqueous interface quickly enough as physiologically required. At 37 °C, DPPC is still quite rigid because it exists in the S phase which explains its poor respreading abilities. Unsaturated lipids components are required to facilitate this process. While PCs are the major phospholipid class in PS, other components include phosphatidylglycerol, phosphatidylethanolamine, phosphatidylinositol, and phosphatidylserine.<sup>51</sup> These phospholipids have also been revealed to help in modulating the respreading and absorption of DPPC. Another constituent present at the air/aqueous interface of alveoli is Chol. Its main function is to maintain the balance between the fluidic and rigid lipid phases in PS.<sup>20</sup>

The total surface area of the human lungs is quite large ( $\sim 70 \text{ m}^2$ ), therefore leaving it quite susceptible to toxins from exogenous and endogenous sources.<sup>52</sup> Some exogenous sources include tobacco smoke, toxic gases, vapors, chemicals, dust particles and ambient air toxins.<sup>53</sup> Also in the body, ROS are constantly generated from many endogenous sources that include mitochondria, phagocytic cells, and the nuclei.<sup>54</sup> While the human body has an elaborate mechanism in place to reduce the impact of tissue damage caused by ROS and other toxins, there are instances where this mechanism can become overwhelmed and as such can lead to injury. One possible way for toxic gases and ROS to exert their toxic effects are via lipid mediators that are formed during their interactions with the lipid component of PS.<sup>55</sup> The target components of PS that are more susceptible to toxic effects are the unsaturated phospholipids and Chol. One previous study revealed that ozone can react with Chol in PS to yield 5,6 $\beta$ -EChol.<sup>56</sup> This observation was made by Pulfer et al. who demonstrated that when the bronchoalveolar lavage fluid from mice was exposed to precise levels of ozone, 5,6 $\beta$ -EChol was identified as the major ozonolysis products.<sup>38</sup> Various *in vitro* studies have also demonstrated that 5,6 $\beta$ -EChol can cause cytotoxicity.<sup>57</sup> In recent years, there has been increasing evidence to suggest that free radicals in the initiation of cellular injury can lead to the development of several lung diseases, for example, acute respiratory distress syndrome (ARDS).<sup>58</sup>

ARDS is a lung disease that affects  $\sim 150,000$  people per year in the USA and has a fatality rate of approximately 30–40%.<sup>59, 60</sup> A patient suffering with ARDS has inhibition of the surfactant components resulting from leakage of serum proteins, hemoglobin, and certain lipids from the small capillaries that surround the alveoli.<sup>59, 61</sup>

The leakage of these components in the lungs is generally the result of the inhalation of toxic gases, severe lung infection, inhalation of gastric contents, and circulatory shock near drowning or radiation damage.<sup>60, 62</sup> Persons diagnosed with ARDS show signs of progressive lung failure, which is an indication of collapsed alveoli, decreased lung compliance, decreased functional residual capacity, and lung edema.<sup>63</sup> At present, no drug has proved beneficial in the prevention or management of ARDS. The current treatment options for ARDS include using noninvasive ventilation or mechanical ventilation with low tidal volumes.<sup>64</sup> However, studies have shown that the ventilation methods used to treat ARDS can lead to ventilator-induced lung injury.<sup>65</sup> For instance, a study by Klimenko et al. observed how different mechanical ventilation methods can cause injurious effects by monitoring the production of 7-KChol, a stable by-product from the oxidation of Chol and indicator of toxicity.<sup>55</sup> This particular oxysterol was monitored because of its high activity and increased ability to penetrate into the cell to cause increased cytotoxicity.

### 1.3 Marine aerosols

Given the vastness of the oceans, marine aerosols constitute the most important and largest reservoir of atmospheric aerosols on a global scale.<sup>66</sup> Marine aerosols have garnered a lot of interest because of their crucial implication in atmospheric chemistry, biogeochemical cycling of nutrients (e.g., C, N and S), as well as in global climate change through their effect on cloud condensation nuclei, radiative balance, and level of precipitation.<sup>66</sup> Primary marine organic aerosols originate mainly from wind-driven

turbulent wave action at the ocean surface, more specifically through the production of sea spray from breaking waves.<sup>67</sup> It is well documented that marine aerosols are enriched in organic matter originating from the sea surface microlayer (SSML), a thin organic layer present at the marine surface.<sup>68</sup> Their structure resembles that of "inverted micelles" with an aqueous core coated by an organic layer of surfactant-like molecules.<sup>69, 70, 71</sup> As these organic species can originate from both anthropogenic and biogenic sources, variability in their composition is expected and may influence aging and surface reactivity of marine aerosols.<sup>72</sup>

According to recent studies, the organic layer of marine aerosols contributed by the living and decaying organic matter present in the sea surface microlayer (SSML) typically contain mono-, di- and tricarboxylic acids, various short chain *n*-alkanes, alcohols, and fatty acids, sterols, as well as monoterpenes and primary saccharides.<sup>73, 74</sup> Earlier studies have also identified fatty acids as the most prevalent organic on the surface of marine aerosols.<sup>12, 13</sup> Tervahattu et al., with the use of TOF-SIMS went even further and labeled both palmitic acid and stearic acid as the most abundant organic component on aerosols.<sup>72, 75, 76</sup> The probable source of palmitic and stearic acids are from the degraded phospholipid components found in cellular membranes of many organisms.

Phospholipids, in particular PCs, the most prevalent lipid component in cellular membranes, has also been detected in the SSML and are also most likely on the surface of marine aerosols.<sup>77</sup> Sterols, another prominent lipid species in cellular membranes, have also been identified at the SSML and are commonly used to identify the sources of organics in sea water and sediments and serve as stable ecological biomarkers.<sup>6, 78, 79, 80</sup>

Among sterols, cholesterol is the most abundant at the marine surface.<sup>80</sup> While cholesterol and other sterols may demonstrate some stability over a period of time, oxidation into different byproducts can occur and have been detected at the SSML.<sup>81</sup> One would expect that the introduction of oxysterols into the organic layer should alter the surface chemical composition and morphology of the organic layer and, in turn, impact the reactivity of marine aerosols. Thus fundamental studies are required to understand molecular-level interactions between dissimilar lipids components that are closely affiliated with organics on the surface of aerosols.

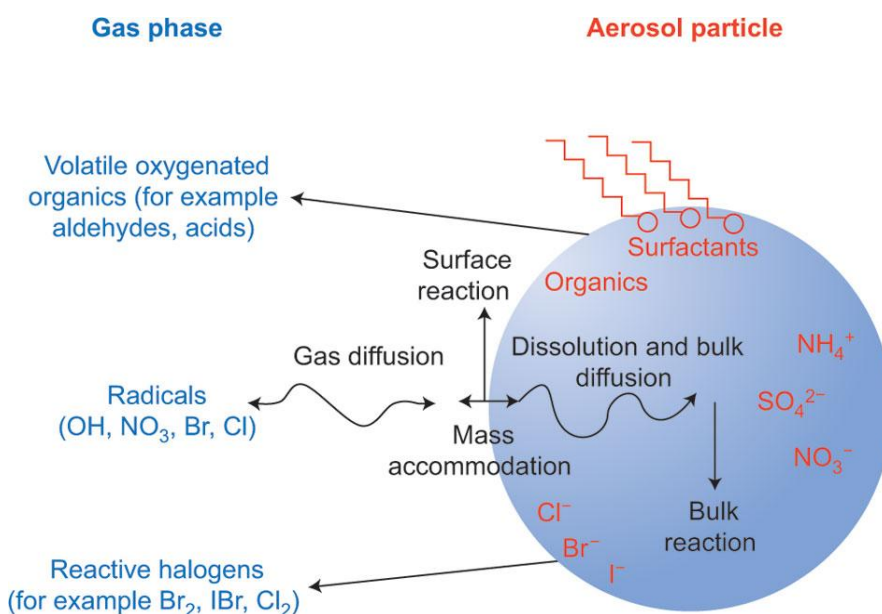


Figure 1.5 Generalized illustration of the processes that govern heterogeneous radical uptake by an aerosol particle.<sup>82</sup>

## 1.4 Langmuir Monolayers

Monolayers involving phospholipids and their mixtures at the air/aqueous interface have been studied extensively because of their ability to mimic biological membranes, PS, and organic films of marine aerosols.<sup>83, 84, 85</sup> While biological membranes typically exist as a bilayer, studies have indicated that monolayer surface pressures in the range of 30-35 mN/m are physiologically relevant to that in biomembranes.<sup>2, 86</sup> Also, monolayer studies are directly correlated to PS because it exist as a monolayer at the air/water interface. And finally, lipids at the SSML that can potentially incorporating onto the surfaces of aerosols have been shown to exist as a monolayer, again indicating the relevance of these studies. Langmuir monolayers offer many possibilities in measuring the effects of various physico-chemical parameters (lipid type, subphase, temperature, pH, composition, surface pressure, etc.) on the interactions between their constituents.<sup>87, 88</sup> Because of the complexity associated with membranes, PS, and marine aerosols, simple model lipid monolayers have been used as proxies in conjunction with many spectroscopic,<sup>89, 90, 91</sup> imaging,<sup>92, 93, 94, 95</sup> and diffractive<sup>96, 97</sup> techniques to study their various biophysical properties, phase transitions, and domain morphology changes.<sup>98, 99, 100</sup>

To the author's knowledge, no systematic study has been done to understand the effects of all three sterols in mixed monolayers with the PCs used in this study. Questions therefore still persist as to how the interfacial behavior of commonly occurring phospholipids are affected by the additional oxygen moiety in oxysterols and therefore needs to be addressed. The choice of PCs as phospholipids comes from the fact that they

are important structural lipids in many different biological and environmental systems. With regards to sterols, Chol is a logical choice because of its importance and ubiquity in a wide array of lipid systems. As for the oxysterols, both 7-KChol and 5,6 $\beta$ -EChol are easily formed by the auto-oxidation of Chol, and have been shown to cause cytotoxic effects both *in vivo* and *in vitro*.

Here we were able to delineate differences in the sterols condensing and ordering abilities when mixed with PC monolayers. In Chapter 2, the basic theoretical theory and instrumentation of surface tensiometry, Brewster angle microscopy (BAM) and vibrational sum frequency generation (VSFG) spectroscopy are discussed. In Chapter 3, the experimental methods used in extracting data from the isotherm curves are discussed. In Chapter 4, the main focus was to investigate the sterols interaction with DPPC. From this particular study, all three sterols demonstrated almost equal thermodynamic stabilities when mixed with DPPC at high surface pressures. However, disparities were observed with oxysterol incapability in duplicating interfacial rigidity demonstrated by Chol. The focus of Chapter 5 involved a more comprehensive understanding of the hydrophobic mismatch between sterols and PCs of different acyl chain lengths. Differences in the relative interactions of the PCs with sterols were also asserted. The focus of Chapter 6 involved the spectral peak assignments of all pure sterols. And finally Chapter 7 discusses the conclusions and implications from this study.

## 2. Chapter : Theoretical Background and Instrumentation

In this chapter, a brief overview of the theory and instrumentation of surface tensiometry, BAM, and VSFG spectroscopy is presented.

### 2.1 Surface Tensiometry theory

When a surfactant molecule is adsorbed to an interface, it can affect the surface tension and hence the surface pressure. To have a greater appreciation for this process, it is important to first understand how the thermodynamic parameters between two bulk phases can influence the interactions at an interface. In a two bulk system, there is no sharp change moving from one bulk phase to another bulk phase at the interface but instead demonstrates a gradual change in the density and the local pressure that is quite inhomogeneous. To illustrate a real interface, a liquid column system containing the two bulk phases  $g$  and  $l$ , each with a number of components ( $n_i$ ), and separated by an interfacial region  $g/l$  (Fig. 2.1); can be used. However, because the interfacial region is not homogeneous, a simplified system is typically used. Inhomogeneity of the interface is a result of the variation of molar ratios. In the ideal system, the two phases  $g$  and  $l$  are separated by the Gibbs dividing surface (GDS), an infinitesimal thin boundary layer, that is placed at an arbitrary position and has zero thickness. This system assumes that the bulk phases in the ideal system remain unchanged up until the GDS:

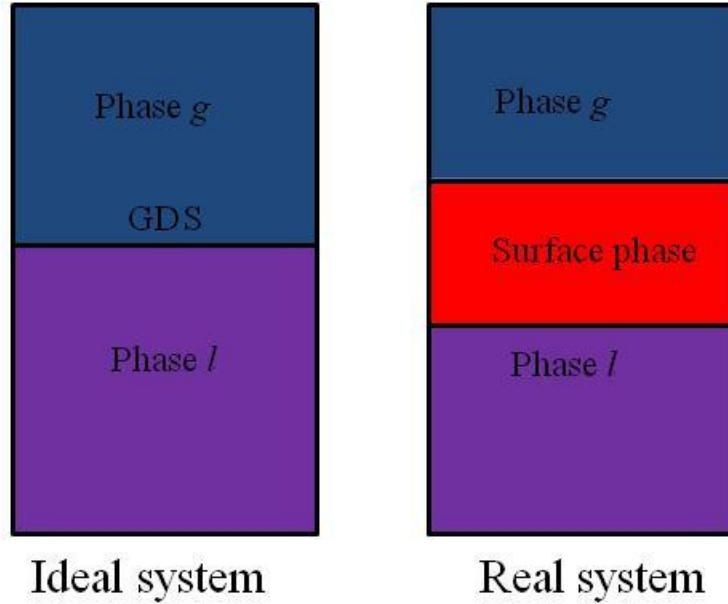


Figure 2.1 Liquid column made of two phases  $g$  and  $l$

The surface excess internal energy  $E^{(g/l)}$  and the entropy  $S^{(g/l)}$  of a real with an interface is defined by <sup>101</sup>

$$E^{(g/l)} = E - (E^{(g)} + E^{(l)}), \quad (2.1)$$

and

$$S^{(g/l)} = S - (S^{(g)} + S^{(l)}), \quad (2.2)$$

where  $E$ ,  $S$  represent the total internal energy and entropy of the actual system, and  $E^{(i)}$ , and  $S^{(i)}$  ( $i = g, l$ ) are the internal energy and entropy of phases  $g$  and  $l$  in the ideal system.

Because the internal energy and entropy depend on the placement of the plane of the GDS, it can either be negative, positive, or zero. The change in the total internal energy for the real system can be represented by

$$dE = TdS - \left( P^{(g)} dV^{(g)} + P^{(l)} dV^{(l)} - \gamma dA \right) + \sum_{i=1}^N \mu_i dn_i, \quad (2.3)$$

where  $P^{(i)}$  and  $V^{(i)}$  ( $i = g, l$ ) represent the actual volume and pressure of the phases  $g$  and  $l$  in the real system.  $A$  denotes the area with regards to the liquid surface,  $\gamma$  the surface tension of the liquid phase, and  $T$  the (absolute) temperature. The volume of the interfacial region is negligible, so therefore the total volume of the system is  $V_t \approx V^{(g)} + V^{(l)}$ . Also, if the surface is almost planar then  $P^{(g)} = P^{(l)}$ .

The differential changes in internal energy of the two phases  $g$  and  $l$  in the ideal system due to changes in heat and work can be expressed by

$$dE^{(g)} = TdS^{(g)} - PdV^{(g)} + \sum_{i=1}^N \mu_i dn_i^{(g)}, \quad (2.4)$$

and

$$dE^{(l)} = TdS^{(l)} - PdV^{(l)} + \sum_{i=1}^N \mu_i dn_i^{(l)}. \quad (2.5)$$

In the ideal system  $V_t = V_g = V_l$  and, as in the real system,  $P_g = P_l$  such that the pressure terms in Eqs. (2.4) and (2.5) can be represented by  $PdV_t$ . The surface energy term ( $\gamma dA$ ) is neglected in the ideal system because only the two bulk phases exist. The change in surface excess internal energy of the interfacial region, Eqs. (2.4) and (2.5) (ideal system) are added and then subtracted from Eq. (2.3) (real system). The final result is

$$dE^{(g/l)} = TdS^{(g/l)} + \gamma dA + \sum_{i=1}^N \mu_i dn_i^{(g/l)}. \quad (2.6)$$

Since  $E^{(g/l)} = G^{(g/l)} - PV^{(g/l)} + TS^{(g/l)}$ , then Eq. (2.6) can be rewritten as

$$dG^{(g/l)} = -S^{(g/l)} dT + V^{(g/l)} dP + \gamma dA + \sum_{i=1}^N \mu_i dn_i^{(g/l)}, \quad (2.7)$$

where  $S^{(g/l)}$ ,  $V^{(g/l)}$ , and  $n_i^{(g/l)}$  are the extensive properties that are related to the surface phase. Keeping these properties constant, Eq. (2.7) can then be reduced to:<sup>101</sup>

$$\gamma = \left( \frac{\partial G^{(g/l)}}{\partial A} \right) \Big|_{T, P, n_i^{(g/l)}}, \quad (2.8)$$

where the surface tension  $\gamma$  represents the rate of change of the Gibbs free energy of the interface per unit area at constant  $T$ ,  $P$ , and  $n_i^{(g/l)}$ . Hence, surface tension can be defined as the work required to increase the area of a surface reversibly and isothermally by a unit amount.<sup>102</sup>

The surface tension of a liquid involves the contraction of an interface and a decrease of the total interfacial area. The reduction of the area is the result of an imbalance of cohesive forces in the interfacial region. A pure liquid in contact with a vapor phase that and are immiscible with each other have different chemical potentials, densities, and molecular interactions. For instance, the bulk of a liquid phase where the attraction between the molecules are van der Waals or dispersive forces, the molecules are equally attracted to one another. This is because the molecules are surrounded by an identical force field. However, at the interface of the liquid, the molecules experience a distorted field because of differences between the forces of attraction coming from the gaseous and liquid phases. The difference in force results in the pulling of the interfacial molecules towards the bulk of the liquid.

## 2.2 Surface Tensiometry Instrumentation

Surface pressure-area per molecule ( $\pi$ -A) isotherm measurements were performed on a film balance system with a deposition apparatus (model KSV minitrough) from KSV Instruments Ltd., Finland. The Teflon trough (176.5 mm  $\times$  85 mm) has two barriers coated with Delrin, a hydrophilic material, to symmetrically compress the monolayer on the subphase. The surface pressure and mean molecular area per molecule (MMA) were monitored during compression of the monolayer via the Wilhelmy plate technique with (Ashless Whatman) Chromatography filter paper serving as plate.

The basic principle of the Wilhelmy plate measurement relies on the pulling forces, a sum of the contribution from gravity, buoyancy, and surface tension, which act on a thin, vertical plate.<sup>20</sup> Typically, the plates are made from ashless filter paper. When the filter paper comes into direct contact with the interface, an equilibrium of forces acting on the plate is established between an upward force, the buoyancy, and downward forces like gravity and surface tension pull. The contact angle of the plate relative to the subphase should be zero as the surface tension is at a maximum at this angle. The magnitude of the surface tension is also dependent on the perimeter and the depth of the plate. The resulting downward forces on the plate is given by<sup>101</sup>

$$\begin{aligned} &= F_{surf} + F_{gravity} + F_{buoyancy} \\ &= 2\gamma_w(W + T) \cos \theta + (WTL)\rho_p g - (WTh)\rho_w g, \end{aligned} \quad (2.9)$$

where  $W$ ,  $T$ , and  $L$  correspond to the width, thickness, and length of the plate,  $h$  is the height of the plate that is submerged into the subphase,  $\gamma_w$  is the surface tension of the

subphase (water or aqueous solution),  $\theta$  is the contact angle,  $\rho_p$  is the density of the plate,  $g$  is the acceleration of gravity, and  $\rho_w$  is the density of the liquid subphase. Eq. (2.9) can be used to measure the difference in the surface tension forces at the air/water interface with or without surfactant monolayer coverage. Assuming that the filter paper has constant dimensions and immersion depth as well as full wetting of the paper plate ( $\cos \theta \approx 1$ ), the difference in surface forces termed surface pressure ( $\pi$ ) is then given by

$$\Pi = \gamma_w - \gamma_s, \quad (2.10)$$

where  $\gamma_s$  is the surface tension of subphase covered with a surfactant monolayer.

### 2.3 Brewster Angle Microscopy Theory

BAM is a non-invasive imaging analytical technique that is based on the principle of minimal reflectance of  $p$ -polarized light incident at the Brewster angle on an optically denser medium.<sup>103</sup> For instance, at the neat air/water interface, there will be little to no reflection of  $p$ -polarized light at the Brewster angle of water. However, when a lipid monolayer is spread on the surface of the water, the Brewster condition is lifted allowing for reflection to occur. BAM is very similar to fluorescence microscopy as both techniques provide valuable insight into phase transitions and changes in the domain morphology that occurs in insoluble monolayers at the air/water interface. One significant difference between these two techniques is that BAM does not require the use of a probe molecule to obtain imaging contrast. In the case of BAM, the imaging contrast is based

solely on the change of reflectance between neat and monolayer-covered air/water interface. However, the reflectance from a monolayer is usually very weak as the thickness of a monolayer is typically much smaller than the optical wavelength used. The following sections give a brief outline of the principles and theory involved in BAM imaging.

Figure 2.2 illustrates a light beam of wavelength  $\lambda$  impinging at an incident angle  $\theta_i$  on the interface between a semi-infinite layer of air with refractive index  $n_a = 1$  and a semi-infinite layer of water  $n_w = 1.33$ . Water is therefore optically denser than air ( $n_w > n_a$ ). At the interface, a fraction of the light beam is reflected back in the air and the remainder is transmitted (or refracted) in water (dashed arrows in Fig.2.2). The light beam can be linearly polarized (i.e., electric field oscillates in one single plane) in the plane of incidence ( $p$ -polarized) or in the plane of the interface ( $s$ -polarized).

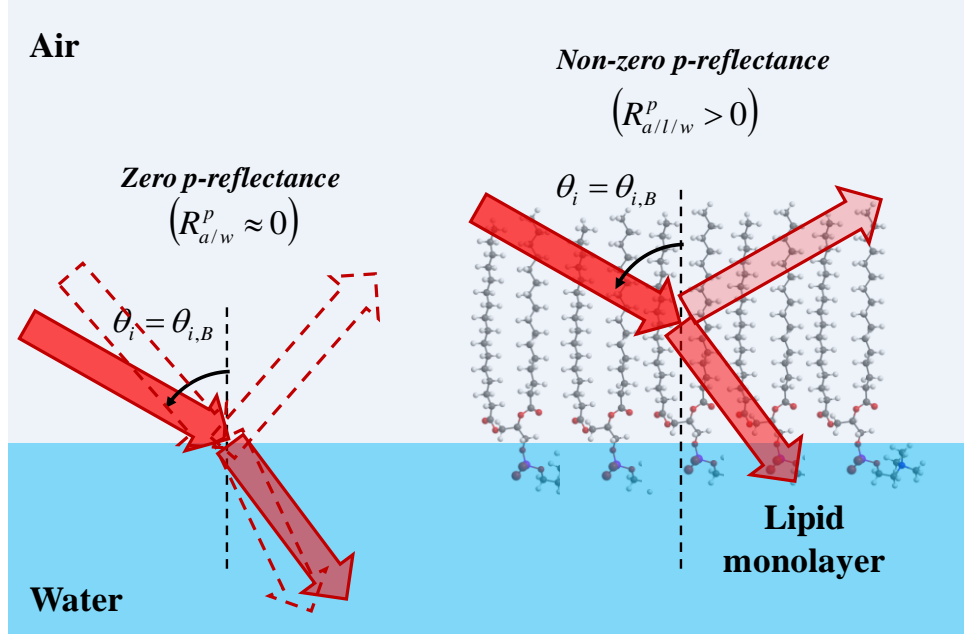


Figure 2.2 Reflectance of  $p$ -polarized light beam incident at the Brewster angle at the bare and monolayer-covered air/water interfaces. The multiple reflections in the lipid monolayer are not shown for clarity.

The reflectance of an interface is defined as the fraction of incident light intensity that is reflected from it. For  $p$ - and  $s$ -polarized light, the reflectance at the neat air/water interface is given by

$$R_{a/w}^{\alpha}(\theta_i) = \frac{I_r^{(a/w)}}{I_i} = |r_{a/w}^{\alpha}(\theta_i)|^2 \quad (\alpha: p, s), \quad (2.11)$$

with

$$r_{a/w}^p(\theta_i) = \frac{E_{r0}^p}{E_{i0}^p} = -\frac{\tan(\theta_i - \theta_t)}{\tan(\theta_i + \theta_t)}, \quad (2.12)$$

$$r_{a/w}^s(\theta_i) = \frac{E_{r0}^s}{E_{i0}^s} = -\frac{\sin(\theta_i - \theta_t)}{\sin(\theta_i + \theta_t)}, \quad (2.13)$$

where  $I_r^{(a/w)}$  is the intensity of light reflected from the air/water interface and  $r_{a/w}^\alpha$  ( $\alpha: p, s$ ) are the  $p$ - and  $s$ -polarized Fresnel reflection coefficients. The transmitted angle  $\theta_t$  is calculated through Snell's refraction law:

$$n_i \sin \theta_i = n_t \sin \theta_t. \quad (2.14)$$

From Eq. (2.11), it is clear that the amount incident light that is reflected depends on the angle and polarization state of the incident light.

From Eq. (2.11), one can show that for  $p$ -polarized light there exists a condition for which

$$R_{a/w}^p(\theta_i) = \left| \frac{\tan(\theta_i - \theta_t)}{\tan(\theta_i + \theta_t)} \right|^2 \rightarrow 0 \quad \text{when} \quad \theta_i + \theta_t = \frac{\pi}{2}. \quad (2.15)$$

This is the so-called Brewster angle or no-reflection condition of the  $p$ -polarized light. The angle of incidence that gives rise to this condition is determined by Snell's refraction law:

$$n_a \sin \theta_i = n_w \sin \left( \frac{\pi}{2} - \theta_i \right) = n_w \cos \theta_i, \quad (2.16)$$

or

$$\theta_{i,B} = \tan^{-1} \left( \frac{n_w}{n_a} \right), \quad (2.17)$$

where  $\theta_{i,B}$  is Brewster's angle. For the neat air/water interface,  $\theta_{i,B} \approx 53^\circ$ .

The reflectance of the monolayer-covered air/water interface can be modeled by a three-layer system: a lipid layer of refractive index  $n_l = 1.4\text{--}1.5$  and finite thickness  $d_l \approx 0.3$  nm embedded between semi-infinite layers of air and water.<sup>104</sup> The presence of a lipid monolayer causes the light beam to be multiply reflected. Taking into account the multiple reflections of the light beam within the lipid monolayer, the reflectance of the  $p$ - and  $s$ -polarized light incident on such as system is given by<sup>105</sup>

$$R_{a/l/w}^\alpha(\theta_i, d_l) = \frac{I_r^{(a/l/w)}}{I_i} = |r_{a/l/w}^\alpha(\theta_i, d_l)|^2 \quad (\alpha: p, s), \quad (2.18)$$

with

$$r_{a/l/w}^\alpha(\theta_i, d_l) = \frac{E_{r0}^\alpha}{E_{i0}^\alpha} = \frac{r_{a/l}^\alpha + r_{l/w}^\alpha e^{2i\delta_l}}{1 + r_{a/l}^\alpha r_{l/w}^\alpha e^{2i\delta_l}} \quad (\alpha: p, s), \quad (2.19)$$

and the phase difference induced by the multiple reflections defined as

$$\delta_l = 2\pi \frac{d_l}{\lambda} \cos\theta_l' = 2\pi \frac{d_l}{\lambda} (n_l^2 - n_a^2 \sin^2\theta_i)^{1/2}, \quad (2.20)$$

where  $I_r^{(a/l/w)}$  is the intensity of the light reflected from the monolayer-covered air/water interface and  $\theta_l'$  is the refracted angle at the air/lipid interface. For very thin films ( $d_l \ll \lambda$ ) like in the case of lipid monolayers, interference effects can be neglected.

The change in  $p$ -reflectance between the neat and monolayer-covered air/water interfaces is given by

$$\Delta R^p = R_{a/w}^p(\theta_i) - R_{a/l/w}^p(\theta_i, d_l) = R(0) - R(d) = R_0 - R, \quad (2.21)$$

where  $R_0$  and  $R$  are the reflectances of  $p$ -polarized light at the neat and monolayer-covered air/water interfaces, respectively.

As shown in Figure 2.3, the maximum change in reflectance between the neat and monolayer-covered air/water interfaces is of the order of  $10^{-9}$  and occurs at normal incidence ( $\theta_i = 0^\circ$ ). However, at normal incidence, the reflectance from the neat air/water interface is about 0.02. This means that in order to detect the presence of the lipid monolayer, the signal-to-noise ratio (SNR) would need to be of the order of  $10^7$ , which is quite impractical and beyond the detection limits of current CCD cameras. Fortunately, the maximum *relative* change in reflectance (which gives the best SNR) obtained by dividing the change of reflectance by that of the neat air/water interface is found at the Brewster angle ( $\theta_{i,B} = \tan^{-1}(1.33) \approx 53^\circ$ ).

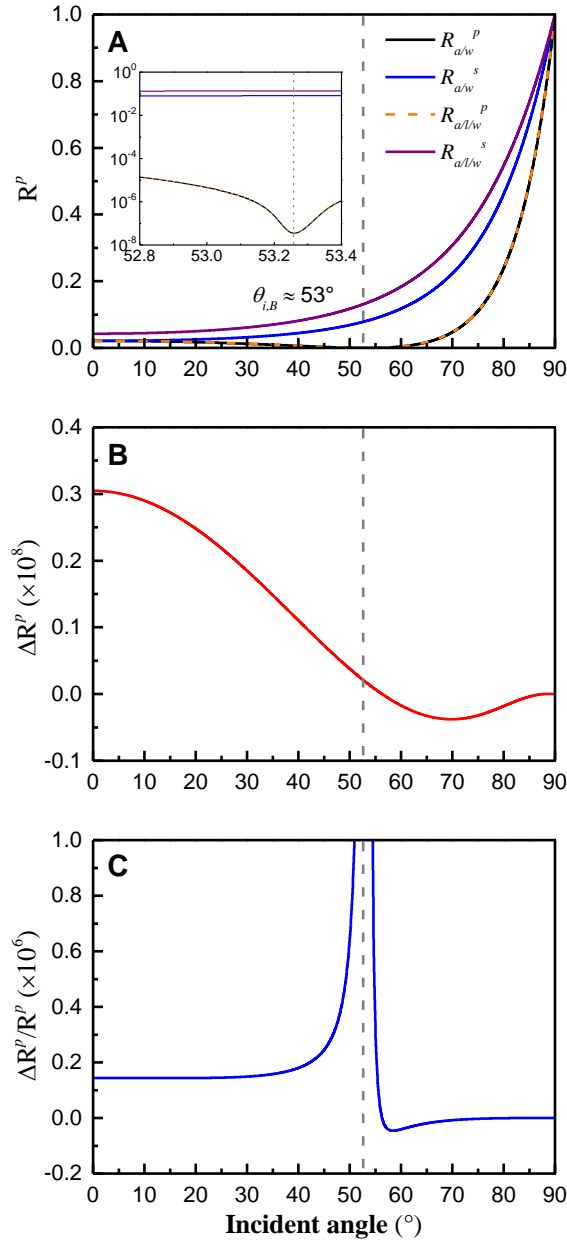


Figure 2.3 (A) Reflectance of  $p$ -polarized light beam incident at the Brewster angle at the bare and monolayer-covered air/water interfaces, (B) change and (C) relative change in reflectance of the air/water interface due to the presence of a lipid monolayer. The parameters used for the calculations were  $n_a = 1.00$ ,  $n_l = 1.5$ ,  $n_w = 1.33$ , and  $\lambda = 633$  nm. The inset shows the minimal *but non-zero*  $p$ -reflectance at the neat and monolayer-covered air/water interfaces.

The Brewster condition is valid only for a perfect interface, i.e., an interface without interfacial layer and with no roughness.<sup>106</sup> A boundary for which this condition holds is called a Fresnel interface. The Fresnel interface is a plane interface for which the refractive index changes abruptly going from one medium to another.<sup>103</sup> At a real interface such as the air/water interface, however, the refractive index does not change abruptly from air to water; the interface is not smooth and as a result one has a minimal but non-zero reflectance at the Brewster angle. This Brewster angle condition enables one to study monolayers adsorbed at the air/water interface because the refractive index of the surfactant monolayer is different than that of either air or water, the conditions that satisfy the Brewster's angle are now changed with the reflectance being strongly affected.

#### 2.4 Brewster Angle Microscopy Instrumentation

The BAM setup is composed of a goniometer onto which an emission and a detection arms are fixed (Fig. 2.4). The goniometer is used here to vary the angular positioning of the arms. The arms of the goniometer support all the components of the BAM setup. The laser source is placed on the emission arm, the objective and tube lens, polarizer, and the charge-coupled device (CCD) camera are placed on the detection arm. A large black Plexiglass housing with sliding doors is used to protect the setup against air currents and dust and to eliminate any external parasitic light. A black glass plate (BGP Nima black glass plate for MircoBAM) was placed to rest at the bottom of the Langmuir trough before filling with water to absorb the refracted beam from reaching the detector.

For the experiments here, two BAM setups were used therefore both of their components will be stated. **(BAM 1)** He-Ne laser source output power of 5 mW (Research Electro-Optics, Boulder, CO) emits a *p*-polarized (>500:1) light beam at a wavelength of 543 nm. **(BAM 2)** He-Ne laser source output power of 17.0 mW. (Research Electro-Optics, Boulder, CO) emits *p*-polarized (> 500:1) light beam at 632.8 nm. **(BAM 1)** The output beam is first attenuated by a neutral density filter, then passed through a half-wave plate, and a Glan-Laser calcite polarizer (GL10-A, extinction ratio 100000:1; Thorlabs, Newton, NJ) before reaching the aqueous surface at the Brewster angle ( $\theta_B \approx 53.1^\circ$ ). **(BAM 2)** The light power is attenuated by a HWP (Ekspla, Lithuania) with an anti-reflective coating at 532 nm. Further filtration of the output light is done by a Glan prism (Ekspla, diameter 14 mm). **(BAM 1 and 2)** The reflected light beam is then collected by a 10× infinity-corrected microscope objective (CFI 60 TU Plan EPI, NA 0.35; Nikon, Melville, NY) that is coupled to a lens tube that has a focal length of 200 mm (MXA22018 CFI; Nikon). The tube lens is needed to here to focus the collimated light onto the CCD. **(BAM 1)** The reflected light was then directed to a back-illuminated EM-CCD camera (DV887-BV, 512 × 512 pixels with 24 μm × 24 μm pixel size; Andor Technology, Belfast, Ireland). Images were acquired with the Andor Solis software (v. 4.15.30000.0, Andor Technology). **(BAM 2)** The light was directed to a back-illuminated anti-reflective CCD camera (DV 412-BV, Andor Technology, Ireland; wavelength range: 350–1000 nm) The CCD camera has 512 × 512 active pixels, each with a pixel size of 24 μm × 24 μm (W × H), thus giving an image viewing area of 12.3 mm × 12.3 mm.

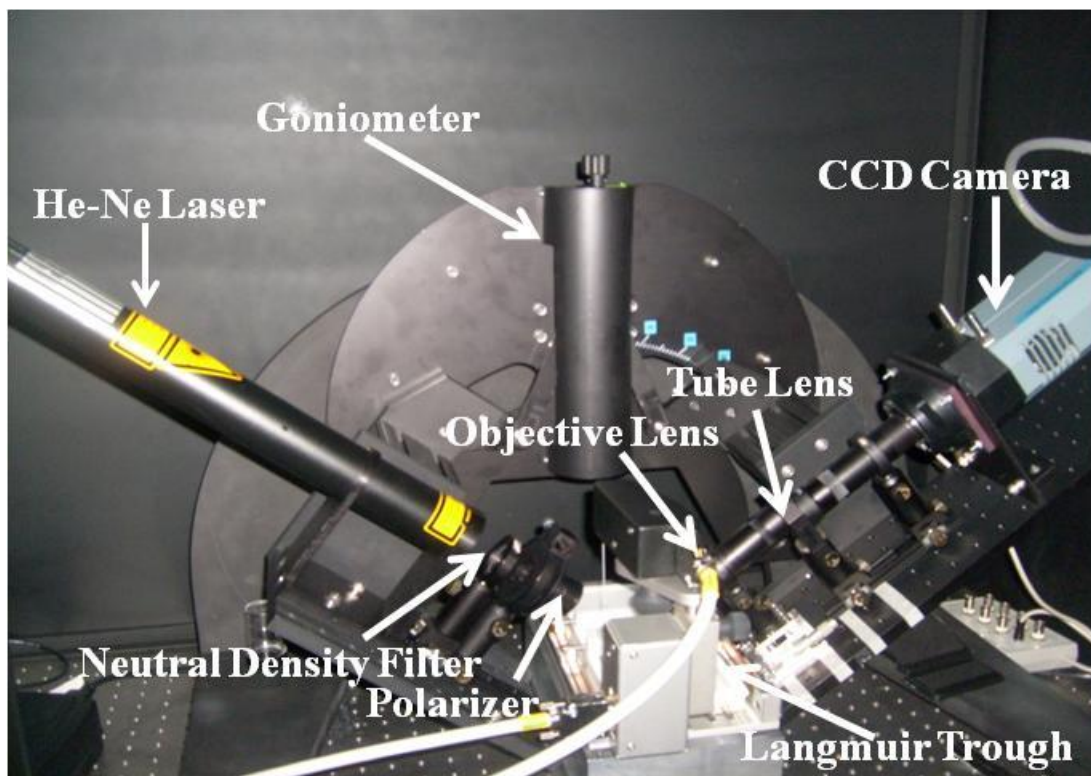


Figure 2.4 Image of the Brewster angle microscope setup and KSV Langmuir trough.

## 2.5 Vibrational Sum Frequency Generation (VSFG) Spectroscopy Theory

VSFG data was collected at the Pacific Northwest National Laboratory (PNNL). The theory and instrumentation is discussed below. VSFG spectroscopy is a nonlinear spectroscopic technique based on the second-order nonlinear process of sum frequency generation (SFG). Briefly, SFG is realized in a medium or at the interface between two media (e.g., the air/water interface), by overlapping spatially and temporally two intense pulsed light beams, one with a fixed visible frequency ( $\omega_{\text{vis}}$ ), the other with a tunable infrared frequency ( $\omega_{\text{IR}}$ ). In order for a SFG signal to be generated in the medium, it must lack inversion symmetry. Intrinsically, the interface between two media also displays

broken symmetry, thus making VSFG spectroscopy a highly surface-specific technique. A vibrational spectrum of molecules adsorbed at the interface can be obtained by scanning the frequency of the IR beam over a set of their vibrational modes. The intensity of the VSFG signal is proportional to the squared modulus of the effective second-order nonlinear susceptibility  $\chi_{\text{eff}}^{(2)}$ , an intrinsic physical parameter of the medium or the interface, as well as to the intensities of the IR ( $I_{\text{IR}}$ ) and VIS ( $I_{\text{VIS}}$ ) input beams:<sup>107, 108</sup>

$$I_{\text{VSFG}}(\omega_{\text{IR}}) \propto \left| \chi_{\text{eff}}^{(2)}(\omega_{\text{IR}}) \right|^2 I_{\text{IR}} I_{\text{VIS}} \quad (2.22)$$

Typically,  $\chi_{\text{eff}}^{(2)}$  results from the contributions of a non-resonant term ( $\chi_{\text{NR}}^{(2)}$ ) and the sum of resonant terms of  $q$  vibrational modes ( $\chi_{\text{R},q}^{(2)}$ )

$$\chi_{\text{eff}}^{(2)}(\omega_{\text{IR}}) = \chi_{\text{NR}}^{(2)} + \sum_q \chi_{\text{R},q}^{(2)}(\omega_{\text{IR}}) \quad (2.23)$$

The non-resonant contribution here is assumed to originate from electronic transitions and is frequency-independent in the IR frequency region. The non-resonant and resonant contributions are generated simultaneously such that their responses are usually convoluted. The resonant response, however, becomes dominant when the frequency of the incident IR beam is in resonance with a vibrational mode of the probed molecules.

The magnitude of  $\chi_{R,q}^{(2)}$  is directly proportional to the number density of the molecules  $N$  and to the molecular hyperpolarizability  $\beta_q^{(2)}$ :

$$\chi_{R,q}^{(2)}(\omega_{IR}) = N \langle \beta_q^{(2)}(\omega_{IR}) \rangle \quad (2.24)$$

where the angular brackets indicate an averaging over the orientations of the molecules. According to Eq. (2.24), the SFG signal is enhanced either by (i) a greater alignment ( $\langle \beta_q^{(2)} \rangle$ ) of molecular transition dipole moments along the surface normal and/or by (ii) a larger number ( $N$ ) of ordered (or oriented) molecules.

The hyperpolarizability  $\beta_q^{(2)}$  is the product of the Raman transition polarizability moment ( $\alpha$ ) and the IR transition dipole moment ( $\mu$ ):

$$\beta_q^{(2)} = \langle g|\alpha|v \rangle \langle v|\mu|g \rangle \quad (2.25)$$

where  $g$  and  $v$  refer to the ground and excited vibrational states, respectively. From Eq. (2.25), it is clear that the SFG signal is dependent upon vibrational modes that are both IR- and Raman-active.

## 2.6 Vibrational Sum Frequency Generation (VSFG) Instrumentation

Details of the high-resolution broadband sum-frequency generation vibrational spectroscopy (HR-BB-SFG-VS) have been described elsewhere.<sup>109, 110</sup> Briefly, the HR-

BB-SFG-VS is based on a set of two Ti:Sapphire oscillators/amplifiers (1 kHz at the fundamental  $\sim 800$  nm), one with 40 fs pulse width, providing the broadband spectral coverage, and the other with 100 ps pulse width, ensuring sub-wavenumber spectral resolution. The two laser systems are electronically synchronized (Synchrolock-AP, Coherent, Palo Alto, CA) to an estimated jitter less than  $\sim 200$  fs. The 40 fs 800 nm beam is used to pump an OPERA-Solo optical parametric amplifier (OPA) to generate the IR light with a power of  $\sim 30$   $\mu\text{J}/\text{pulse}$  in the C-H stretching region ( $2750\text{--}3100\text{cm}^{-1}$ ). The 100 ps 800nm beam provides the source of VIS radiation in the high-resolution frequency-resolved experiments, with a power  $<60$   $\mu\text{J}/\text{pulse}$ . The SFG signals in the reflected direction are collected with a monochromator (Andor Technology, Belfast, NIR, Shamrock 750 mm, 1200 lines/mm grating) and CCD (Andor Technology, Newton 971P, back-illuminated). Different beam polarization configurations (*ssp* and *ppp*) were used and are denoted in order of increasing wavelength (SFG, VIS, and IR).

### 3. Chapter : Experimental Methods

#### 3.1 Methods

##### 3.1.1 Compression isotherm measurements

Surface pressure-molecular area ( $\Pi$ - $A$ ) compression isotherms were measured on a computer-controlled Langmuir film balance system (KSV Minitrough; KSV Instruments, Finland). The Teflon-coated Langmuir trough (KN1001,  $A_{\text{total}} = 150 \text{ cm}^2$ ) has two hydrophilic Delrin-coated barriers for symmetrical monolayer compression. The trough was placed on a vibration-isolated optical table at the center of the Brewster angle microscope (described below). The combined setup was enclosed in a black Plexiglas box to limit ambient air currents, dust particles, and parasitic light. A defined volume of pure or mixed lipidic solution was spread onto the water subphase using a 50  $\mu\text{L}$  microsyringe (model 705, Hamilton, Reno, NV) with the trough barriers initially in the fully expanded position. The spreading solvent was then allowed to evaporate for at least 10 min, after which the monolayer was symmetrically compressed at a speed of 6  $\text{\AA}^2/\text{molecule}/\text{min}$ . This compression rate was slow enough to limit unwanted domain growth artifacts coming from diffusion-limited aggregation.<sup>111</sup> Surface pressure was monitored during compression using a Wilhelmy plate made of filter paper

(Ashless Whatman 41, Sigma-Aldrich) hung to a high precision microbalance (KSV Instruments). The surface pressure is defined as follows:<sup>112</sup>

$$\Pi = \gamma_0 - \gamma_s, \quad (1)$$

where  $\gamma_0$  and  $\gamma$  are the surface tension values of the bare and monolayer-covered air/water interfaces, respectively. Monolayer data were collected using KSV proprietary software (v. 2.0.1, KSV Instruments) and analyzed using OriginPro (v. 9.0, OriginLab, Northampton, MA). All isotherms were recorded at room temperature ( $21 \pm 1$  °C) and were repeated at least three times to ensure reproducibility. The standard deviations of the measured mean molecular area and surface pressures were  $\pm 0.5$  Å<sup>2</sup> and  $\pm 1$  mN/m, respectively. To address monolayer stability, each compression isotherm was completed within approximately 30 min, as the onset of oxidation of pure Chol monolayers has been found to occur around 45 min after spreading.<sup>113</sup> This was typically reflected by the expansion of the isotherm caused by the presence of oxidized Chol derivatives like 7-KChol and 7-hydroxyChol which occupy larger mean molecular areas than Chol. Similarly, oxidation of Chol mixed in DMPC monolayers was shown to be detectable only after 40 min of air exposure.<sup>114</sup>

### 3.1.2 Isotherm analysis

The change in the monolayer elasticity due to the ordering effect of sterols on PCs acyl chains as well as the identification of phase transitions were analyzed using the

isothermal compressibility modulus ( $C_s^{-1}$ ) calculated from the compression isotherm data following:<sup>112</sup>

$$C_s^{-1} = -A_{\Pi}(d\Pi/dA)_T, \quad (2)$$

where  $A_{\Pi}$  is the mean molecular area at a given surface pressure  $\Pi$ . Large compressibility modulus values correspond to a lower interfacial elasticity and more ordered acyl chains.<sup>86</sup>

Intermolecular interactions between PC and sterols in the mixed monolayers were analyzed with the help of the excess free energy of mixing ( $\Delta G_{exc}$ ) as a function of sterol composition, which corresponds to the compression work difference between real and ideal mixtures. It was calculated from the experimental compression isotherm data following:<sup>112, 115</sup>

$$\Delta G_{exc} = N_A \int_0^{\Pi} \Delta A_{exc} d\Pi \quad (3)$$

where the excess mean molecular area ( $\Delta A_{exc}$ ) for the mixed monolayer at a given pressure  $\Pi$  corresponds to the difference between the experimental mean molecular area ( $A_{12}$ ) measured from the compression isotherm and the ideal mean molecular area ( $A_{12}^{id}$ ) calculated from the additivity rule:<sup>112, 116</sup>

$$\Delta A_{exc} = A_{12} - A_{12}^{id} = A_{12} - [(A_1)_{\Pi}X_1 + (A_2)_{\Pi}X_2], \quad (4)$$

where  $A_1$  and  $A_2$  are the mean molecular areas of the pure components 1 and 2, respectively,  $X_1$  and  $X_2 (= 1 - X_1)$  their corresponding mole fractions, and  $N_A$  is Avogadro's constant. Negative or positive  $\Delta G_{exc}$  deviations are an indication of nonideal behavior, with negative and positive values implying cohesive interactions between dissimilar (PC and sterol) and similar (PC-PC or sterol-sterol) components, respectively.

To verify the condensing effect of the sterols the partial molecular area of the PCs were calculated with the use of the following equation:

$$A_{PC}^* = \frac{(A_{12} - A_{sterol} \times X_{sterol})}{1 - X_{sterol}} \quad (5)$$

where  $A_{sterol}$  and  $X_{sterol}$  are the sterol molecular area and molar ratio and  $A_{PC}^*$  is the molecular area of the phosphatidylcholine.

3.1.3 High-Resolution, Broad-Bandwidth Vibrational Sum Frequency Generation (HR-BB-VSFG) measurements were performed at the Pacific Northwest National Laboratory under the guidance of Hong-fei Wang and Li Fu.

Chol, 7-KChol and 5,6 $\beta$ -EChol were spread on water in Teflon Petri dishes (6 cm diameter) to obtain a surface pressure of 40 mN/m. Following spreading, 10 min was allowed for solvent evaporation, after which VSFG spectra were collected. The acquisition time for each spectrum was 5–10 min. The spectra were collected with two polarization configurations (*sps* and *pps*). The data was analyzed using OriginPro (v. 9.0,

OriginLab, Northampton, MA). The spectra were recorded at room temperature ( $24 \pm 1$  °C) and were repeated at least two times to ensure reproducibility.

### 3.1.4 Propagation of Error

As previously mentioned, the standard deviation of the isotherms for the measured mean molecular areas are  $\pm 0.5 \text{ \AA}^2$ . As the isotherms were used in the calculation of the excess surface area values ( $\Delta A_{exc}$ ), the partial molecular area of the PCs values ( $A_{PC}^*$ ) and the Gibbs free energy values ( $\Delta G_{exc}$ ), it was important to determine the propagation of error with each calculation method.

To calculate the propagation of error, the partial derivative of a function with respect to each variable that had an uncertainty was used. From the base definition, one can set  $x$  to be a function of at least two other variables, where  $a$  and  $b$  must have an uncertainty.

$$x = f(a, b, \dots) \quad (6)$$

The variance ( $\sigma_x^2$ ) of  $x$ , with respect to the variance in  $a$  and  $b$  can be approximated using partial derivatives as follows,

$$\sigma_x^2 = \sigma_a^2 \left( \frac{\delta x}{\delta a} \right)^2 + \sigma_b^2 \left( \frac{\delta x}{\delta b} \right)^2 + \dots \quad (7)$$

To determine the variance of the excess area analysis (Eq. 4) the equation used is as follows because it is an addition/subtraction equation and therefore the partial derivative is 1.

$$\sigma_x^2 = \sigma_a^2 + \sigma_b^2. \quad (8)$$

With substitution of the standard deviation, the variance is as follows,

$$\sigma_{\Delta A_{exc}}^2 = \sigma_{A_{12}}^2 + \sigma_{A_1}^2 + \sigma_{A_2}^2 = (0.50 \text{ \AA}^2)^2 + (0.50 \text{ \AA}^2)^2 + (0.50 \text{ \AA}^2)^2 = 0.75 (\text{ \AA}^2)^2. \quad (9)$$

Therefore the error with respect to the  $\Delta A_{exc}$  values are

$$\sqrt{\sigma_{\Delta A_{exc}}^2} = \sqrt{0.75 (\text{ \AA}^2)^2} \approx 0.87 \text{ \AA}^2. \quad (10)$$

The variance with respect to the  $A_{PC}^*$  using (Eq. 5) is as follows,

$$\sigma_{\Delta A_{PC}^*}^2 = \sigma_{A_{12}}^2 + \sigma_{A_{sterol}}^2 = (0.50 \text{ \AA}^2)^2 + (0.50 \text{ \AA}^2)^2 = 0.50 (\text{ \AA}^2)^2 \quad (11)$$

Therefore, the error associated with the  $A_{PC}^*$  values is shown in (Eq. 10)

$$\sqrt{\sigma_{\Delta A_{PC}^*}^2} = \sqrt{0.50 (\text{ \AA}^2)^2} \approx \pm 0.71 \text{ \AA}^2. \quad (12)$$

The uncertainty with respect to the  $A_{PC}^*$  using (Eq.5) is shown in (Eq. 13) where  $X_{sterol} = 0.5$ .

$$A_{PC}^* = \frac{(0.71 \text{ \AA}^2 \times 0.5)}{1 - 0.5} = \pm 0.71 \text{ \AA}^2. \quad (13)$$

The uncertainty with respect to the  $\Delta G_{exc}$  values using (Eq. 3) is shown in (Eq. 14) where

$\Pi = 10 \text{ mN/m}$ .

$$\Delta G_{exc} = N_A \int_0^{\Pi} 0.87 \text{ \AA}^2 d\Pi = \pm 50 \text{ J/mol} \quad (14)$$

#### 4. Chapter :Condensing and Ordering Effects of Cholesterol, 7-Ketocholesterol and 5 $\beta$ ,6 $\beta$ -Epoxycholesterol on DPPC

To the authors' knowledge, there has been to date only few comparative studies of the effects of Chol, 7-KChol, and 5,6 $\beta$ -EChol in binary mixtures with phospholipids.<sup>21, 117</sup> For example, Kamal and Raghunathan used X-ray diffraction to examine DPPC multilayers containing ring-substituted oxysterols, including 7-KChol and 5,6 $\beta$ -EChol. They found that the phase behavior of the DPPC-oxysterol membranes was very similar to that with Chol. However, slight differences in the degree of acyl chain ordering reflected by an increase in the thickness of the DPPC bilayer and in the amount of sterol required to suppress the lipid main phase transition were observed. They speculated that these differences could be due to the orientation of the oxysterols in the bilayers. Besides this work, there have been very few monolayer studies on the interfacial behavior of 7-KChol and none so far with 5,6 $\beta$ -EChol mixed with PCs or any other commonly occurring phospholipid.<sup>22, 26, 113</sup> Hence, the question of how these oxysterols influence the phase behavior of PC monolayers relative to Chol, has yet to be addressed.

In this Chapter, we investigate the effects of Chol, 7-KChol, and 5,6 $\beta$ -EChol on the biophysical properties of DPPC monolayers in a broad range of compositions and surface pressures physiologically relevant to biomembranes using compression isotherm measurements and BAM at the air/water interface. The combination of these two

techniques provides real-time information about the interfacial behavior and domain morphology of the mixed monolayers. Here we find that the sterols differ with regards to their condensing and ordering ability in a DPPC monolayer with Chol being more effective than the two oxysterols. We also show that mixed monolayers containing Chol and 7-KChol exhibit greater stability compared to 5,6 $\beta$ -EChol. Finally, we observe distinct collapse aggregates for the pure sterols suggesting differences in their packing. These changes in the interfacial behavior of DPPC caused by the presence of oxysterols can have significant implications for the lateral organization of cellular membranes, especially lipid raft formation.

#### 4.1 Materials

1,2-Dipalmitoyl-*sn*-glycero-3-phosphocholine (DPPC, >99%), 7-ketocholesterol (7-KChol, >99%), and 5 $\beta$ ,6 $\beta$ -epoxycholesterol (5,6 $\beta$ -EChol, >99%) were purchased from Avanti Polar Lipids (Alabaster, AL), whereas cholesterol (Chol, >99%) was from Sigma-Aldrich (St. Louis, MO). Lipid and sterol stock solutions (1 mM) were prepared in chloroform (HPLC grade,  $\geq$ 99.0%, Fisher Scientific, Pittsburgh, PA). Mixed solutions of desirable compositions were prepared from their respective stock solutions. Ultrapure Milli-Q water (18.2–18.3 M $\Omega$ ·cm, pH 5.6) was used as aqueous subphase and was obtained from a Barnstead Nanopure system (model D4741, Barnstead/ThermoLyne Corporation, Dubuque, IA) equipped with additional organic removing cartridges (D5026 Type I ORGANIC free Cartridge Kit; Pretreat Feed).

## 4.2 Results

### 4.2.1 Pressure-area compression isotherms of sterols in mixed monolayers with DPPC

To compare the interfacial properties of oxysterols with Chol, the compression isotherms of the pure sterol monolayers were first recorded (Fig. 4.1). Isotherm lift-offs were found at  $\sim 37$ ,  $\sim 39.5$ , and  $\sim 39 \text{ \AA}^2/\text{molecule}$  for Chol, 7-KChol, and 5,6 $\beta$ -EChol, respectively. The slightly higher values for the oxysterols point to increased steric hindrance and electrostatic repulsion between bulkier neighboring molecules. Also, both oxysterol isotherms displayed a change of slope, indicative of a more disordered monolayer in comparison to Chol. This slope change was documented previously in the case of 7-KChol monolayers;<sup>22, 26</sup> however, to the best of the authors' knowledge, no isothermal data has been reported before for 5,6 $\beta$ -EChol. Another interesting feature in the isotherms are the differences in the maximum collapse surface pressure with values of 45.0, 46.7, and 49.5  $\text{\AA}^2/\text{molecule}$  for Chol, 7-KChol, and 5,6 $\beta$ -EChol, respectively. This result suggests that the additional oxygen atom, whether it be a ketone or epoxide on the B ring, increases the stability of the oxysterol monolayers at high surface pressures. By closer inspection of Fig. 4.1, one notices that the collapse phase of oxysterol monolayers undergo a similar process: first, the surface pressure reaches a maximum, then it slightly decreases before stabilizing in the form of a long plateau region. However, by comparison, the post-collapse pressure decrease is mostly prominent in Chol monolayer followed by the 5,6 $\beta$ -EChol monolayer, but barely noticeable for 7-KChol. Previous work on the collapse phase of Chol monolayers has attributed this surface pressure drop to the initial formation of an unstable 3D phase (aggregates) within the 2D monolayer,

that rapidly transforms into another more stable 3D collapse phase and reaches equilibrium with the monolayer at a slightly lower surface pressure.<sup>118</sup> Because of the similarities in the collapse onset with Chol and 5,6 $\beta$ -EChol isotherms, a similar aggregation mechanism may also be involved.

The influence of sterol type and composition on the phase behavior of DPPC was subsequently investigated with the compression isotherms of DPPC monolayers mixed with Chol, 7-KChol, and 5,6 $\beta$ -EChol (Fig. 4.2). Without sterol, the compression isotherm of pure DPPC monolayer showed its typical phase transitions, in particular a liquid expanded-liquid condensed (LE-LC) coexistence region at surface pressures between ~3.5 to 6 mN/m, in agreement with previously published isotherms.<sup>119, 120</sup> It is important to note that the collapse pressure of DPPC is usually found at or above 70 mN/m. With the Langmuir trough used here, such high surface pressures could not be reached because of film leakage induced by subphase surface meniscus inversion.<sup>121</sup> However, isotherm data should be reliable up to about 40 mN/m, a surface pressure limit that includes surface pressures encounter in expanded lung surfactant films and biological membranes (~30–35 mN/m). For this reason, the thermodynamic analysis developed below will be restricted to this low to moderate surface pressure range.

Isothermal data was subsequently collected for the mixed DPPC/sterol monolayers with increasing sterol molar ratio ( $X_{\text{sterol}}$ ) in Fig. 4.2. The addition and increase of the sterol molar ratio ( $X_{\text{sterol}}$ ) led to several new features including the shifting of the isotherms to smaller mean molecular areas and the LE-LC coexistence region becomes less prominent. Further analysis of the data from the mixed DPPC/sterol

monolayers with  $X_{\text{sterol}} \leq 0.1$  still maintain a coexistence region but with reduced width and at lower mean molecular areas than DPPC. Both observations are in line with the occurrence of a condensing effect. Moreover, this transition occurs at different surface pressures for each sterol. For example, in the case of  $X_{\text{Chol}} = 0.1$ , the LE-LC coexistence region appears at a slightly lower surface pressure in comparison to pure DPPC, whereas with the oxysterols, the opposite trend is observed. As seen for the DPPC/sterol monolayers at  $X_{\text{sterol}} = 0.3$ , the LE-LC coexistence region is less obvious for Chol but is still observable with 7-KChol and 5,6 $\beta$ -EChol. Finally, at higher sterol concentrations ( $X_{\text{sterol}} \geq 0.5$ ), the plateau region associated with the pure DPPC isotherm is not observed.

The condensing effect of Chol and oxysterols in the mixed monolayers was further analyzed by looking at the variation of mean molecular area as a function of sterol composition at fixed surface pressures ( $\Pi = 3, 10, 20, 30$  and  $40$  mN/m) (Fig. 4.3). This surface pressure range was chosen to understand the impact of the physical state of the mixed monolayer on the condensing effect as it is physiologically relevant to biological membranes.<sup>2</sup> Based on the magnitude of the (negative) deviation from the additivity rule, it is evident that the condensing effect is more prominent in the LE region ( $\sim 3$  mN/m) for all mixed DPPC/sterol monolayers. Additionally, the condensing effect also shows some dependency on the sterol type. For instance, for a mixed DPPC/sterol monolayer with  $X_{\text{sterol}} = 0.5$ , the following hierarchy is observed: Chol > 7-KChol > 5,6 $\beta$ -EChol with Chol having the strongest condensing ability and 5,6 $\beta$ -EChol the weakest. At higher surface pressures ( $>10$  mN/m), the condensing effect is significantly reduced because DPPC is in a condensed phase. Overall, in the low and high surface pressure regimes,

mixed monolayers with a sterol composition in the range  $0.3 \leq X_{\text{sterol}} \leq 0.7$  showed the greatest condensation.

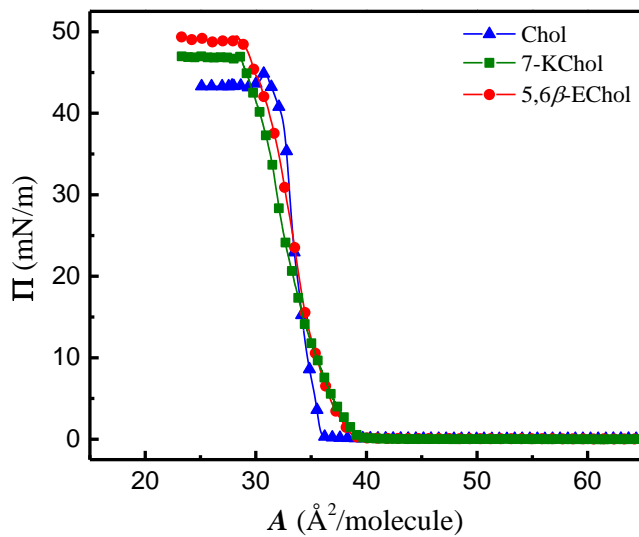


Figure 4.1 Compression isotherms of pure Chol, 7-KChol, and 5,6 $\beta$ -EChol monolayers.

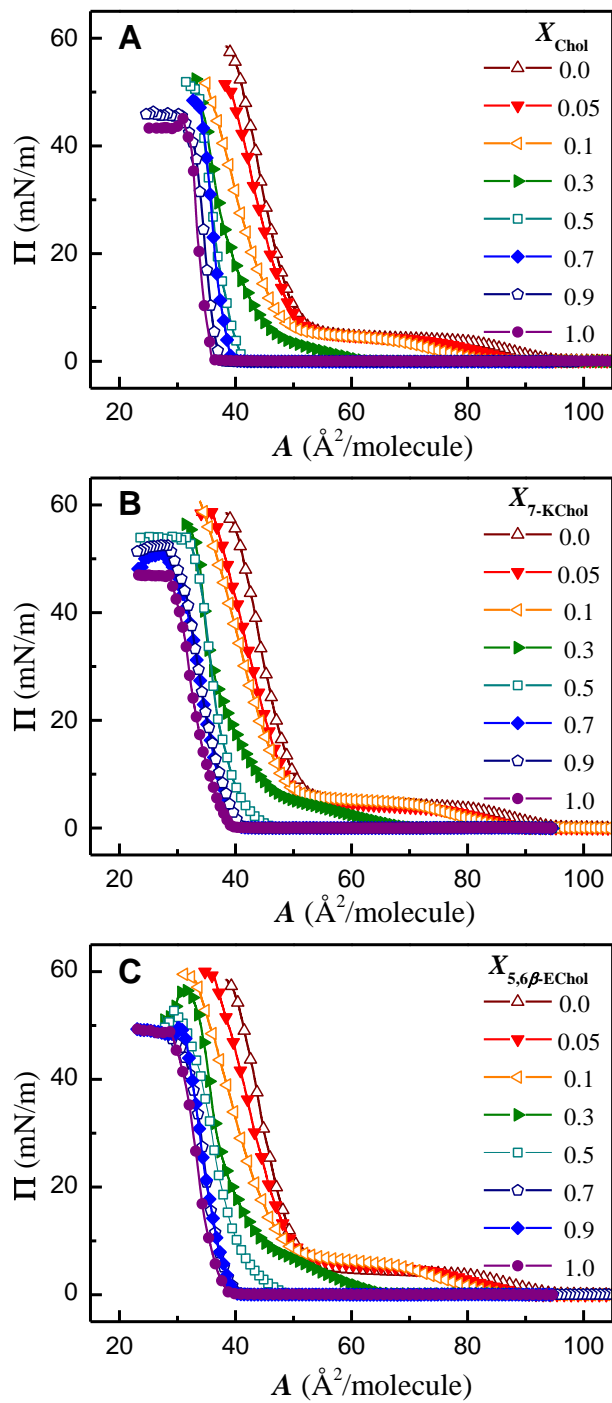


Figure 4.2 Compression isotherms of (A) Chol, (B) 7-KChol, and (C) 5,6 $\beta$ -EChol mixed with DPPC monolayers

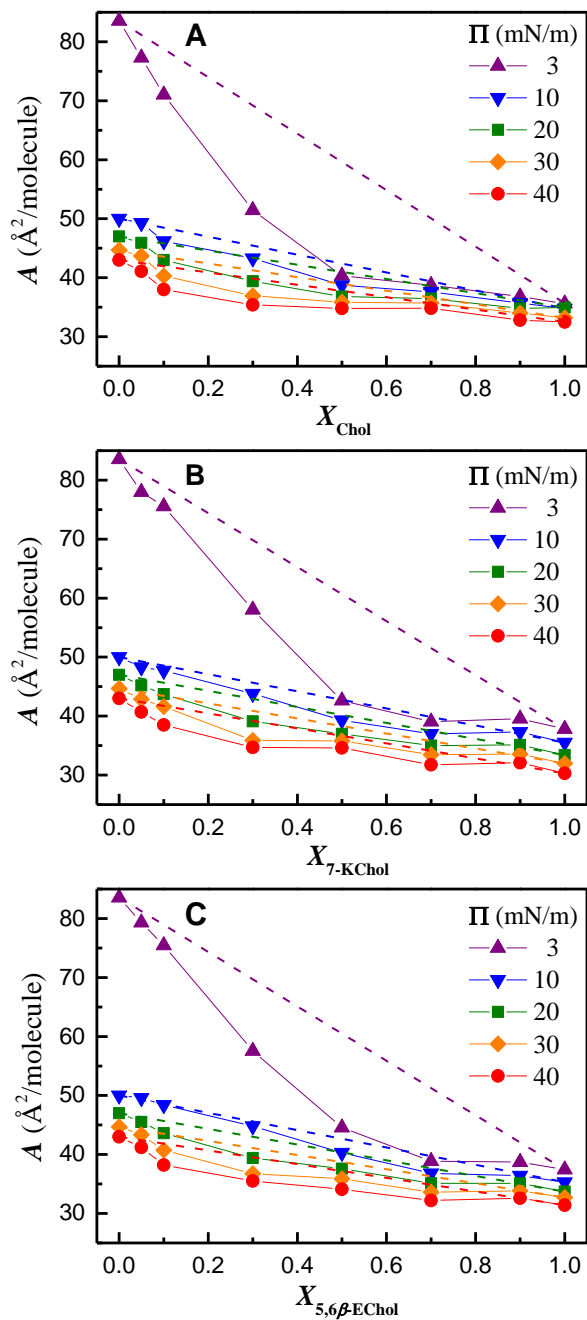


Figure 4.3 Variations of mean molecular area with sterol composition for (A) Chol, (B) 7-KChol, and (C) 5,6 $\beta$ -EChol in binary mixed DPPC monolayers.

#### 4.2.2 Interfacial compressibility modulus

To gain further insight into the physical state of the mixed monolayers, the isothermal compressibility modulus ( $C_s^{-1}$ ) calculated from the compression isotherms was analyzed as a function of surface pressure and sterol composition (Fig. 4.4A–C). The variations of the monolayer compressibility modulus with surface pressure for pure sterol monolayers reveals that Chol achieved the highest compressibility modulus ( $\sim 620$  mN/m) followed by 5,6 $\beta$ -EChol ( $\sim 248$  mN/m) and 7-KChol ( $\sim 223$  mN/m).

The compressibility data shows that pure DPPC and mixed DPPC/sterol monolayers with  $X_{\text{sterol}} \leq 0.1$  have similar interfacial rigidity as the LE-LC phase transition is still observed between 3.5 and 10 mN/m. In the DPPC/Chol monolayer with  $X_{\text{Chol}} \leq 0.1$ , the LE-LC coexistence region (indicated by an arrow in Fig. 4.4A) overlaps with that of pure DPPC. In the case of 7-KChol and 5,6 $\beta$ -EChol, this transition shifts slightly towards higher surface pressures ( $\sim 6$ – $7$  mN/m). In mixed DPPC monolayers at  $X_{\text{sterol}} = 0.3$  the LE-LC coexistence region is still observed for 7-KChol and 5,6 $\beta$ -EChol at  $\sim 4$ – $5$  mN/m, but is not discernible for Chol. The variation of the monolayer compressibility modulus with sterol composition was monitored at surface pressures ranging from 3 to 40 mN/m (Fig. 4.4D–F). With the addition of small amounts of sterols (i.e.  $0 \leq X_{\text{sterol}} \leq 0.1$ )  $C_s^{-1}$  decreases, especially in the surface pressure range from 20 to 40 mN/m. In the range of  $X_{\text{Chol}} = 0.1$ – $0.3$ , the compressibility modulus of the mixed DPPC/Chol monolayers remains practically unchanged, however moving from  $X_{\text{Chol}} = 0.3$  to 0.7, it increases almost linearly at all surface pressures. In contrast, in the same molar

ratio range, only a small increase is observed in the mixed monolayers of 7-KChol and 5,6 $\beta$ -EChol.

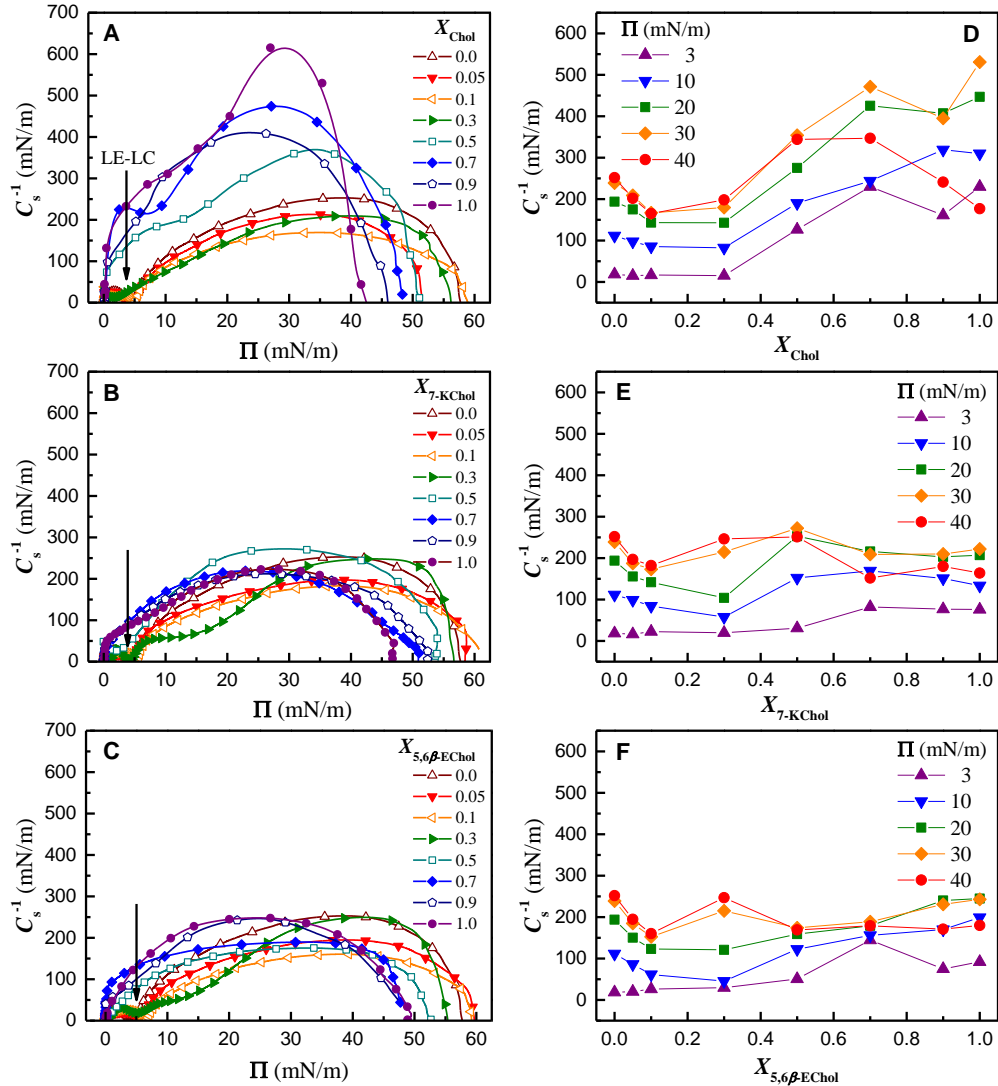


Figure 4.4 Variations of monolayer compressibility modulus with (A–C) surface pressure and (D–F) sterol composition for (A, D) Chol, (B, E) 7-KChol, and (C, F) 5,6 $\beta$ -EChol in binary mixed DPPC monolayers. The compressibility data were calculated from the compression isotherms in Fig. 4.2. The position of the LE-LC phase transition in the compressibility plots is indicated by an arrow.

### 4.2.3 Excess free energy of mixing

The non-ideality of the mixed DPPC/sterol monolayers was assessed and the interactions between individual components were quantitatively analyzed by calculating the excess free energy of mixing ( $\Delta G_{\text{exc}}$ ) from the compression isotherms as a function of sterol composition (Fig. 4.5). All investigated mixtures demonstrate non-ideality ( $\Delta G_{\text{exc}} < 0$ ) over the entire surface pressure range, indicating attractive DPPC-sterol interactions. Further analysis reveals that at lower surface pressures (3 and 10 mN/m) the most stable (i.e., with most negative  $\Delta G_{\text{exc}}$ ) mixed DPPC/sterol monolayers exist at  $X_{\text{sterol}} = 0.5$ . However, at higher surface pressure values (20, 30 and 40 mN/m), the minimum  $\Delta G_{\text{exc}}$  shifts towards a monolayer composition richer in DPPC ( $X_{\text{sterol}} = 0.3$ ). At this sterol composition and at a surface pressure of 30 mN/m, the following hierarchy is observed for the stability of DPPC/sterol monolayer: 7-KChol > 5,6 $\beta$ -EChol  $\approx$  Chol; in contrast, at  $\Pi = 40$  mN/m, the hierarchy becomes: 7-KChol  $\approx$  Chol > 5,6 $\beta$ -EChol. Overall, DPPC monolayers with 7-KChol are more thermodynamically stable at high surface pressures than those with Chol and 5,6 $\beta$ -EChol. Comparing the minimum values of  $\Delta G_{\text{exc}}$  at  $\Pi = 30$  and 40 mN/m for the mixed DPPC/sterols (Fig. 4.5D), explicitly shows that the strength of interactions in the mixed DPPC/5,6 $\beta$ -EChol monolayer is the smallest.

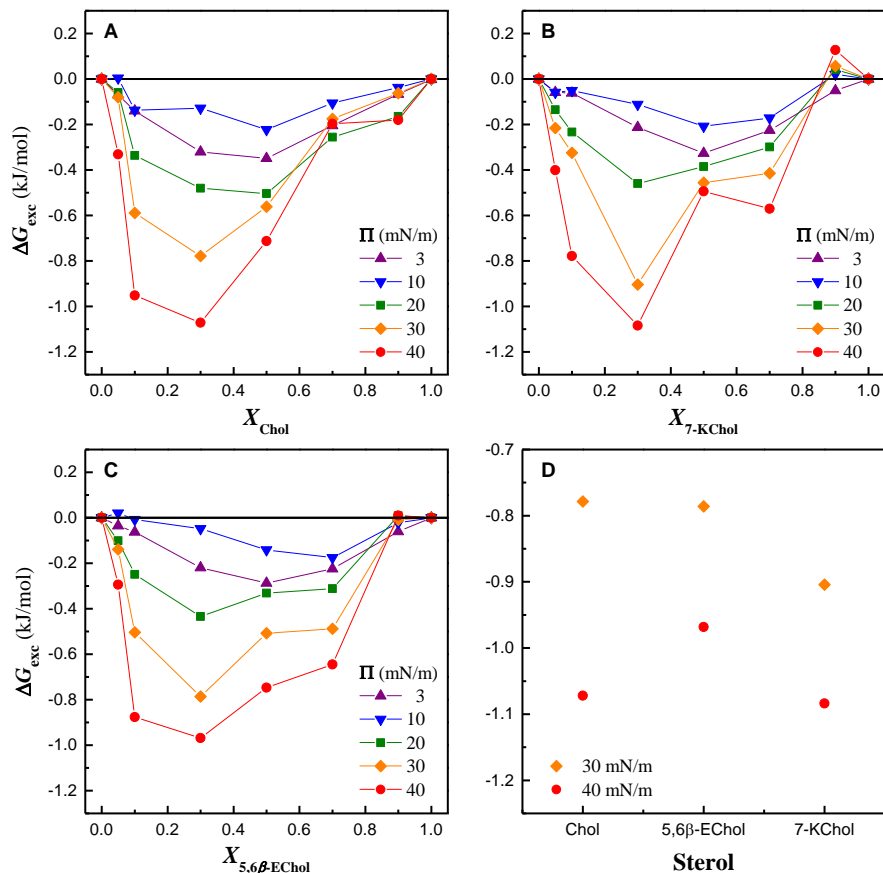


Figure 4.5 Variations of excess free energy of mixing with sterol composition for (A) Chol, (B) 7-KChol, and (C) 5,6 $\beta$ -EChol in binary mixtures with DPPC. (D) Excess free energy of mixing values for Chol, 5,6 $\beta$ -EChol and 7-KChol at 30 and 40 mN/m.

#### 4.2.4 BAM images

The domain morphology of pure and mixed monolayers was investigated by BAM. Fig. 4.6A shows BAM images of the pure DPPC monolayer. At large mean molecular areas ( $>100 \text{ \AA}^2/\text{molecule}$ ) and low surface pressures ( $\sim 1 \text{ mN/m}$ ) the image is homogeneous with very low reflectance (image not shown) which is indicative of the gas-liquid expanded (G-LE) phase. With continued compression, the same homogeneous

BAM image is observed in the LE phase. Once the LE-LC coexistence region is reached at  $\sim 3.5$  mN/m, small bright irregular LC domains are observed, immersed in the darker LE phase. At higher surface pressures ( $\Pi \geq 4$  mN/m), larger multilobed LC domains can be easily resolved. These images are consistent with previously published data on DPPC.<sup>111</sup> The LC domains eventually grow in size along the LE-LC phase until they coalesce into one homogeneous condensed phase.

In the case of the Chol monolayer BAM images revealed that, at large mean molecular areas ( $A \geq 70$  Å<sup>2</sup>/molecule), circular and ovoid condensed domains coexisted with the gas phase (Fig. 4.6B). Upon further compression of the monolayer, most of these domains merged into a completely homogeneous condensed phase ( $\Pi \sim 30$  mN/m). Approaching the collapse phase, small circular-like 3D aggregates are observed. Further compression led to an increase in the domain size and number. However, following the drop in the surface pressure after collapse, the small aggregates appear to transition into a rod-like shape.

In comparison to Chol, the 7-KChol monolayer shows almost no isolated condensed domains at large mean molecular areas, but rather a largely condensed phase with few circular dark (lipid-poor) regions of different sizes scattered throughout, indicative of a less compact monolayer (Fig. 4.6C). Further compression of the monolayer also resulted in a homogeneous condensed phase, although at a slightly larger mean molecular area ( $39$  Å<sup>2</sup>/molecule) than Chol. At the collapse phase, similar to Chol, small circular-like 3D aggregates are observed followed by an increase in their size and number at higher surface pressures. However, unlike Chol, no change in the aggregate

shape occurs with further compression. Instead the 3D aggregates continued to increase in size and also underwent further aggregation with one another into larger structures. Much like the pure 7-KChol monolayer, very few condensed domains are seen at large mean molecular areas in the 5,6 $\beta$ -EChol monolayer; instead a quasi-condensed phase is observed with darker worm-like channels running across it (Fig. 4.6D). At lower mean molecular areas ( $A \approx 60\text{--}70 \text{ \AA}^2/\text{molecule}$ ) these lipid-poor regions transformed into filiform and circular domains. Like Chol and 7-KChol, the collapse phase of 5,6 $\beta$ -EChol, also shows the appearance of circular-like 3D aggregates, although in much greater number. Further compression finally causes shape transitioning into rod-like structures slightly slender than those of Chol.

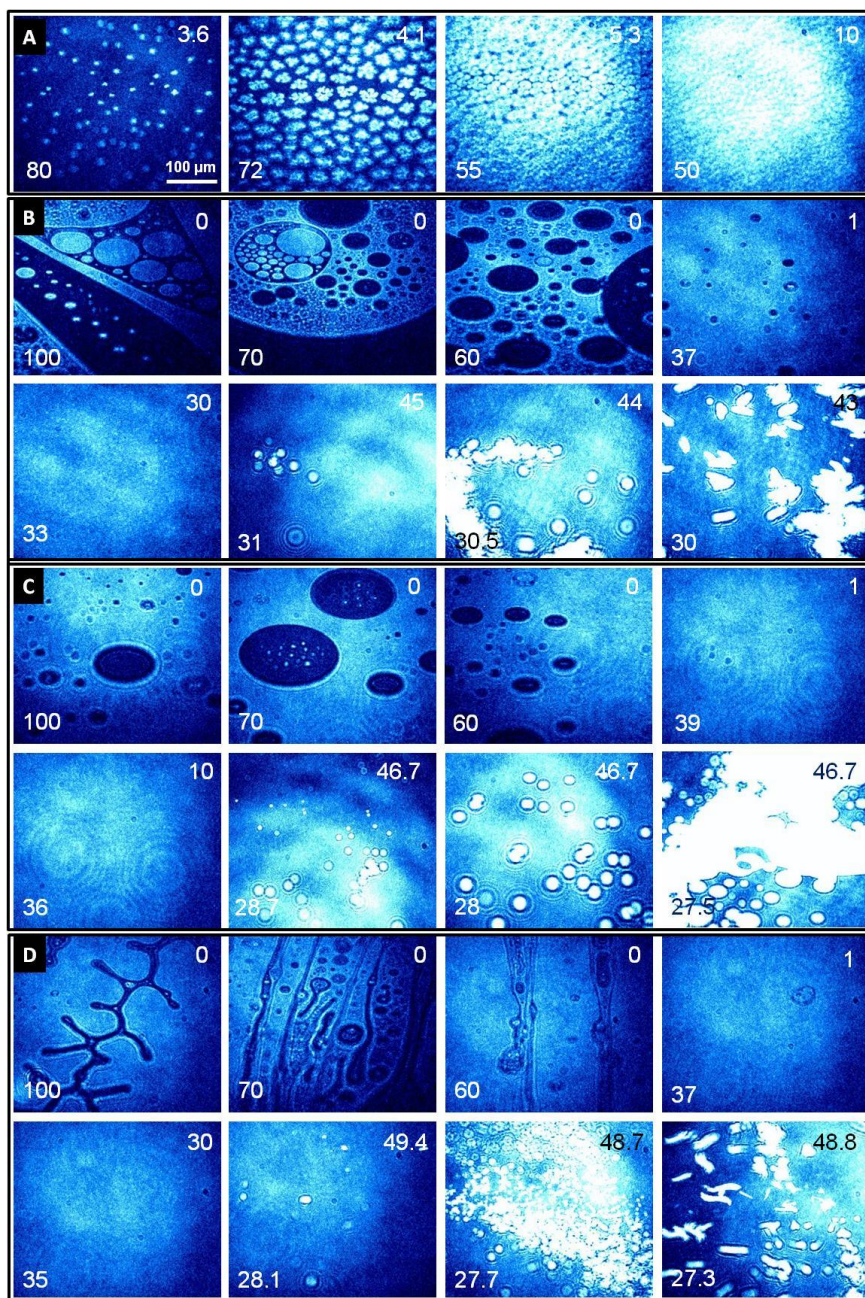


Figure 4.6 BAM images of pure (A) DPPC, (B) Chol, (C) 7-KChol, and (D) 5,6 $\beta$ -EChol monolayers at different stages of compression. Numbers in the lower left and upper right corners indicate the mean molecular area and the surface pressure, respectively.

The BAM images shown in Fig. 4.7A corresponds to DPPC/sterol at  $X_{\text{sterol}} = 0.05$ . With the addition of this small amount of sterol, a dramatic change to the domain morphology is observed in the LE-LC phase ( $A = 60\text{--}70 \text{ \AA}^2/\text{molecule}$ ) in the hierarchy Chol > 7-KChol > 5,6 $\beta$ -EChol. The irregularly shaped LC domains of the pure DPPC monolayer are replaced by smaller ones in the mixed DPPC/oxysterol monolayers. However, the shape of these domains was not discernible due to the available BAM resolution. As the LC domains are larger in the DPPC/5,6 $\beta$ -EChol, this indicates here that among the three sterols, 5,6 $\beta$ -EChol is the least effective in disrupting (i.e., fluidizing) the condensed phase of DPPC. Previous studies using epifluorescence microscopy, atomic force microscopy (AFM), and near-field scanning optical microscopy (NSOM) have shown these LC domains of DPPC/Chol at similar ratios to be spiral-shaped.<sup>9, 122, 123</sup> Further compression results in a homogeneous condensed phase similar to but slightly more compact than that observed for pure DPPC. The BAM images shown in Fig. 4.7B corresponds to the DPPC/sterol at  $X_{\text{sterol}} = 0.3$ . In the mixed Chol monolayer, heterogeneity at low surface pressures ( $< 1 \text{ mN/m}$ ) is observed at large mean molecular areas ( $A \geq 70 \text{ \AA}^2/\text{molecule}$ ) but not in 7-KChol and 5,6 $\beta$ -EChol. Further analysis of the BAM images for the mixed monolayer at  $X_{\text{Chol}} = 0.3$  reveals a mixture of circular and droplet-shaped condensed domains with higher reflectivity immersed in a less condensed phase. Similar domains have also been reported by epifluorescence microscopy in mixed DPPC/Chol with similar molar ratios.<sup>9, 124</sup> Another study also documented a similar effect using AFM on mixed DPPC/Chol monolayer with  $X_{\text{Chol}} = 0.25$ ; three separate phases

coexisting with each other were identified.<sup>123</sup> As the isotherm lifts off, the heterogeneity progressively disappears and a fully condensed phase is then observed.

BAM images of DPPC/Chol with  $X_{\text{Chol}} = 0.1$  show somewhat homogeneous phase throughout the full compression (Appendix A, Fig. A1); however, note that the reflectance did increase with smaller molecular areas indicating increased lipid density. Previous studies were able to delineate filiform or stripe domains in monolayers with the same Chol composition.<sup>123</sup> Unfortunately, the domains formed in the LE-LC region were too small to be visualized with the BAM used in this study. BAM images of DPPC/7-KChol with  $X_{7\text{-KChol}} = 0.1$  (Appendix A, Fig. A2) in the LE-LC phase are further reduced, although they remain visible for  $X_{5,6\beta\text{-EChol}} = 0.1$  (Appendix B, Fig. B1). In the mixed monolayer with  $X_{\text{Chol}} = 0.5$ , at low surface pressures ( $< 1$  mN/m) the monolayer begins to take on more Chol-like features indicating a more condensed monolayer and increased lipid packing. With increasing Chol concentration, the domains appear more like those of the pure Chol monolayer. In the mixed monolayers with  $X_{7\text{-KChol}} = 0.5$  the BAM images appear homogeneous throughout the whole compression, whereas for  $X_{7\text{-KChol}} = 0.7$  and 0.9, the mixed monolayer took on the appearance of 7-KChol. This similar trend was also observed in the mixed DPPC/5,6 $\beta$ -EChol monolayer.

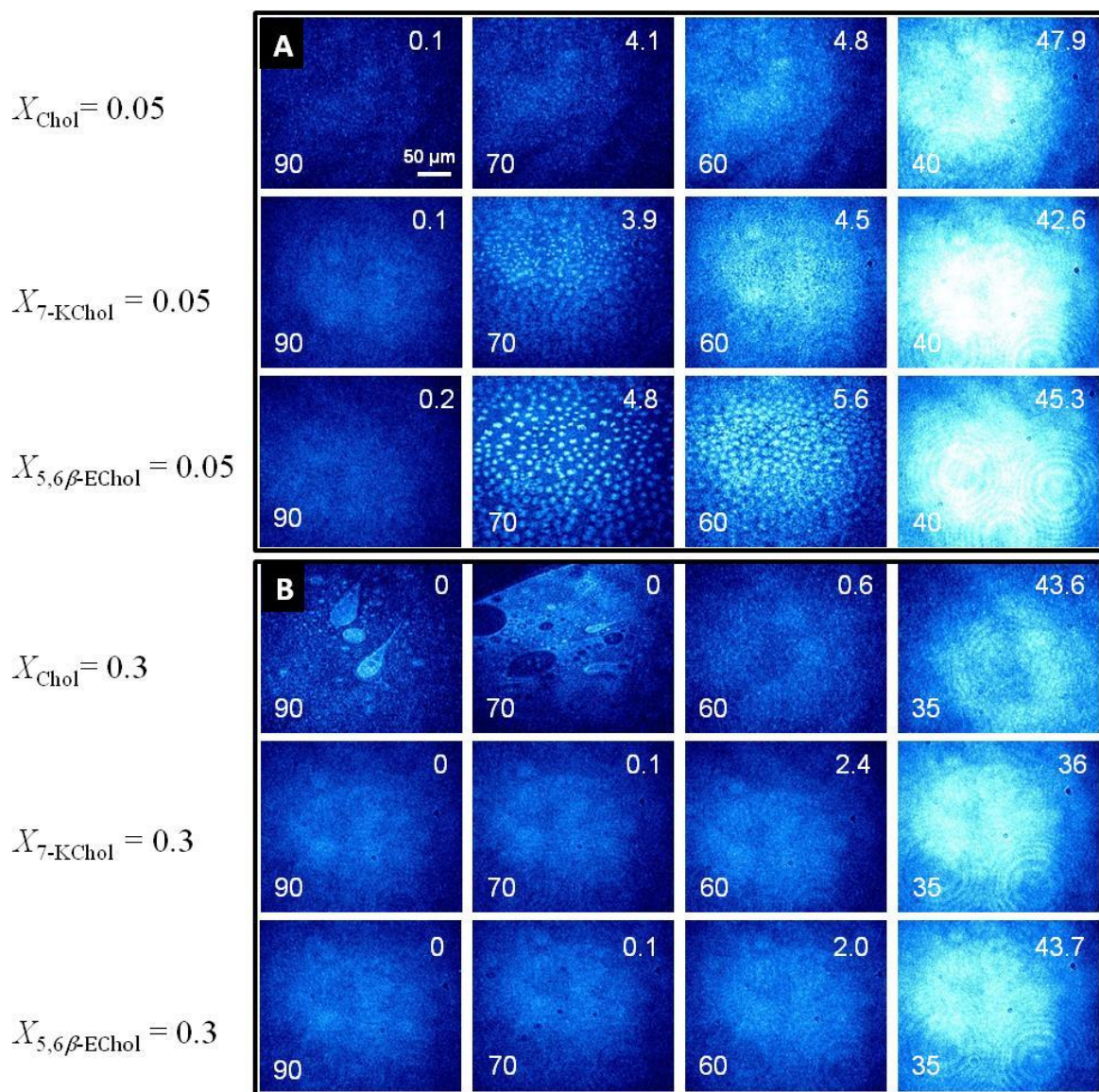


Figure 4.7 BAM images of DPPC/sterol monolayers with (A)  $X_{\text{sterol}} = 0.05$  and (B)  $X_{\text{sterol}} = 0.3$  at different stages of compression. Numbers in the lower left and upper right corners indicate the mean molecular area and the surface pressure, respectively.

### 4.3 Discussion

The present study investigated the effects of Chol and two oxysterols (7-KChol and 5,6 $\beta$ -EChol) in mixed monolayers with DPPC to assess their relative impact on the condensing effect, thermodynamic stability, lateral elasticity, and domain morphology with varying sterol composition by analyzing isothermal data and BAM images. Both oxysterol modifications are found on the B steroid ring but differ in their chemical structure and carbon position of oxygen moiety relative to Chol. The presence of sterols in the mixed monolayers of DPPC had a profound effect on the compression isotherm. Previous studies with mixed DPPC/Chol have documented the shifting of the isotherms to lower mean molecular areas.<sup>9, 125</sup> This shift is referred to as “condensing effect” and has been observed with many different analytical and spectroscopic techniques in mixed phospholipids or sphingomyelin monolayers containing sterols.<sup>1, 10, 126</sup> Various mechanisms have been proposed to explain this condensing effect, the two most widely accepted being the stable complex formation and, more recently, the “umbrella effect”.<sup>127, 128</sup> In the stable complex formation, the condensing effect results from the strong attractive interactions between phospholipid and sterol in the binary mixture, whereas with the umbrella effect the phospholipid headgroups are believed to protect the hydrophobic part of the sterol from the aqueous subphase, thereby favoring closer proximity. As was shown above in the compression isotherms, all three sterols used in this study exhibit a definite condensing ability.

This condensing effect seen in the compression isotherms is better displayed with the change in mean molecular area with sterol composition. From the data it is clear that

at the lowest surface pressure analyzed (3 mN/m) all three sterols demonstrate a pronounced condensing effect for all mixtures. Yet, at high surface pressures, DPPC molecules are more closely packed, therefore, the relative differences between the sterols with respect to the condensing effect become less significant.

On closer inspection, at  $X_{\text{sterol}} = 0.5$ , the condensing effect is most prominent in the Chol mixed monolayer. As the surface pressure increased, the condensing effect was significantly reduced as DPPC enters the condensed phase. The relative condensing ability with each sterol at 3 mN/m is mainly attributed to differences in the molecular structure. In a mixed DPPC/sterol monolayer, the van der Waals interactions are the primary attractive intermolecular interactions between the acyl tails and the steroid nucleus. The hydrophobicity of Chol is greater than that of 7-KChol and 5,6 $\beta$ -EChol, thus resulting in stronger attractive interactions with the acyl tails of DPPC and a more effective condensing effect in the mixed monolayer at lower surface pressures. As mentioned in the Introduction, 7-KChol differs from Chol by having an additional oxygen atom on C7, while 5,6 $\beta$ -EChol has an epoxy group between C5 and C6 and no longer retains the double bond nor its planarity. These structural modifications to Chol result in 7-KChol being the most hydrophilic of the three sterols considered in this study. Because of its greater hydrophilicity, 7-KChol should have demonstrated the lowest condensing ability when mixed with DPPC, however, this was not the case. Instead, DPPC/5,6 $\beta$ -EChol mixed monolayers displayed the least condensing effect. One possible reason for the different thermodynamic behavior between the oxysterols comes from their different interactions with the hydrophobic acyl tails of DPPC. As 7-KChol is more

hydrophilic, the ketone group has been shown to be thermodynamically unstable in the hydrophobic environment of the acyl tails of DPPC.<sup>129</sup> This instability results in 7-KChol being tilted towards the air/water interface. With respect to 5,6 $\beta$ -EChol, not only does it lack planarity on the steroid A-B ring but the configuration also brings the epoxy moiety in closer proximity to the hydrophobic acyl tails, thereby increasing steric effects.<sup>21</sup> The differences here are clearly related to the positioning of the oxygen moiety relative to the acyl tails of DPPC.

The impact of the sterols on the DPPC chain ordering is also reflected in the physical state of the monolayer as revealed by the interfacial compressibility modulus.<sup>130, 131</sup> According to Davies and Rideal,  $C_s^{-1}$  values in the range of 100 to 250 mN/m are indicative of a monolayer in the LC phase, while larger values reveal that the monolayer is in a liquid-ordered ( $l_o$ ) or solid state with closely packed acyl chains.<sup>132</sup> In the data presented here,  $C_s^{-1} \geq 250$  mN/m are mostly observed for mixed DPPC/Chol monolayers with  $X_{\text{Chol}} \geq 0.5$ . With 7-KChol mixed films, such large compressibility values are only obtained for  $X_{7\text{-KChol}} = 0.5$  ( $C_s^{-1} = 272$  mN/m), while with 5,6 $\beta$ -EChol, no such values were found at any sterol composition. The larger  $C_s^{-1}$  observed in the mixed monolayer with  $X_{\text{Chol}} \geq 0.5$  is the result of the cholesterol's ability to order the tails of DPPC and to form the  $l_o$  phase. From the results presented here, both oxysterols appear to be poor raft promoters in comparison to Chol because of their lower interfacial rigidity. In a computational study, Aittoniemi et al. were able to demonstrate difference in the tilt angle of Chol and modified sterols in a DPPC bilayer.<sup>133</sup> In their model, Chol was shown to have the smallest tilt and to reside almost perpendicular to the bilayer plane, hence

enabling it to have better ordering ability. To the authors' knowledge, no comparable simulations on the tilt orientation of 7-KChol or 5,6 $\beta$ -EChol in bilayers have so far been reported. However, Smondyrev and Berkowitz have found 6-ketocholestanol, an analogous of 7-KChol, to be tilted in a DPPC bilayer with its ketone group oriented towards the aqueous phase, preferring to be hydrated rather than to be buried in the hydrophobic core of the acyl tails.<sup>129</sup> Because of the structural similarities between 6-ketocholestanol and 7-KChol, it was then suggested that 7-KChol must also be tilted.

In addition to assessing the nonideal behavior of the mixed monolayers, the excess free energy of mixing was also used here to obtain information regarding the DPPC-sterol interactions. Chol and 7-KChol show quantitatively almost the same stability at low sterol composition ( $X_{\text{sterol}} < 0.5$ ) and higher surface pressures ( $\Pi \geq 30$  mN/m), followed by 5,6 $\beta$ -EChol. This result indicates that the additional oxygen substitutions on 7-KChol did not have a significant impact on the attractive interactions between the sterol ring and the phospholipid acyl tails at high surface pressures. However, the reduced planarity of 5,6 $\beta$ -EChol makes these interactions slightly less favorable compared to 7-KChol. At  $X_{\text{sterol}} \geq 0.5$ , the mixed monolayers became progressively less stable with the increasing sterol concentration. It appears that while all three sterols demonstrate favorable interactions with DPPC, the oxysterols are inferior to Chol in their ordering abilities. In relating these results to biomembranes, it is quite possible that these oxysterols can compete with Chol in their interactions with DPPC and similar phospholipids. For instance, in the context of lipid rafts formation, it remains to be seen if these differences in condensing/ordering effect between Chol and oxysterols

would also affect Chol/sphingolipids interactions in the same manner.

BAM images also confirm that the molecular structure of sterols has an impact on the domain morphology of pure and mixed monolayers, particularly in the collapse region. In the pure sterol monolayers studied here, differences in the domain structures were identified at large mean molecular areas and in the collapse region of the isotherms. At large mean molecular areas, Chol domains display greater complexity and are also more numerous. In the collapse phase, the 3D aggregates display differences with regards to their sizes and shapes suggesting variations in the molecular packing. The BAM images at the onset of collapse in Chol and 5,6 $\beta$ -EChol monolayers show what appeared to be circular-like aggregates, which, upon continued compression in the plateau region, transformed into rectangular and needle-like shapes, respectively. By comparison, no such aggregate shapes were observed throughout the plateau region of the collapse phase of 7-KChol.

Previous studies have determined that Chol can have two types of 3D collapse aggregates in the bulk monolayer: monohydrate and anhydrous, with the monohydrate being the most stable form in water.<sup>134</sup> GIXD experiments have also shown that the 3D aggregates of collapsed Chol monolayers are trilayers composed of a bilayer and a disordered Chol monolayer separated by one water layer.<sup>135, 136</sup> This water layer is suggested to maintain a continuous hydrogen bonding channel between the hydroxyl groups of Chol molecules from the monolayer and bilayer. These interactions are believed to stabilize the crystal structure of the aggregates.<sup>136</sup> X-ray diffraction was also used to determine the hydrated crystal structure of 7-KChol.<sup>137</sup> Notable differences in the

crystal structures of 7-KChol and Chol were found and traced back to the participation of the ketone group in the hydrogen bonding network in addition to two hydroxyl groups from other 7-KChol molecules. This additional binding may disrupt the hydrogen bonding channel that is associated with the Chol monohydrate. This supports the BAM images of the sterol collapse phases, which show that the ketone group of 7-KChol has a greater impact on the shape of the 3D collapse aggregates than Chol (as well as 5,6 $\beta$ -EChol).

Another interesting feature that is observed here is the relative size of the 7-KChol 3D collapse structures in comparison to those of Chol and 5,6 $\beta$ -EChol. The 3D collapse aggregates in the 7-KChol monolayer were on average three to six times larger indicating more molecules in one aggregation site. This increase in the aggregation size of 7-KChol is manifested with a significant increase in the reflectivity observed from the BAM images suggesting the formation of multilayer structures that are thicker than those of the other two sterols. As previously mentioned, 7-KChol has been identified in atherosclerotic plaque, therefore its ability to form larger aggregates relative to the other sterols suggests a possible mechanism for its crystallization in plasma membranes.

The BAM images of the pure DPPC monolayer reveals that the LE phase surrounds the LC domains. According to McConnell's analysis, the overall shape of LC domains are influenced by the balance between line tension and dipole density difference between the two phases.<sup>138</sup> Because this dipole difference is usually large in the coexistence region, the line tension dominates. In the mixed DPPC/sterol monolayers containing  $X_{\text{sterol}} = 0.05$ , the condensed domains that are characteristic of the LE-LC

coexistence region of DPPC are dramatically affected, revealing that line tension changes are occurring. In the case of Chol, the sizes of the domains are reduced. As shown by Keller et al., the presence of Chol in DPPC monolayers decreased the size of the domains indicating that Chol prefers to reside at the interfacial boundary between the condensed and fluid phases hence reducing the line tension.<sup>139</sup> The fact that the domains in the LE-LC coexistence region of the DPPC/oxysterol monolayers are larger than those of DPPC/Chol indicates that Chol has a greater capacity to lower the line tension of the DPPC domains. This line tension reduction of the DPPC domains in the presence of Chol is another indicator that it intercalates more easily at the boundaries of the DPPC condensed phase. In DPPC/sterol monolayers with  $X_{\text{sterol}} = 0.3$  the condensed domains usually found in the pure DPPC monolayer are no longer present. At this molar ratio, Chol shows the most interesting domain structure as indicated by the heterogeneity seen in the images in the low surface pressure regime. In contrast, BAM images of DPPC/oxysterol monolayers were quite homogeneous. The heterogeneity seen at  $X_{\text{Chol}} = 0.3$  was previously reported and was thought to be the result of three separate phases in coexistence with each other, with Chol-rich and Chol-poor domains.<sup>123</sup> In the DPPC/Chol mixed monolayer at  $X_{\text{Chol}} \geq 0.5$  the domain structure is more Chol-like at lower surface pressures, whereas for 5,6 $\beta$ -EChol and 7-KChol with  $X_{\text{sterol}} \geq 0.3$  the domains are quite homogeneous. These results indicate that phase separation in the mixed DPPC/Chol monolayers was more prevalent than those with oxysterols indicating that modifications to the molecular structure of Chol by the addition of an oxygen atom can potentially impact lipid raft formation.

Given increasing evidence of the presence of oxysterols in biomembranes thorough studies are therefore needed to unravel their mechanism of action. Our study reveals that Chol displays the largest ordering capability in DPPC monolayers in comparison to the oxysterols. As lipid rafts are known for their rigidity, one can speculate that the increasing levels of oxysterols will affect their packing order as studies here reveal. Further work would be required to examine how the competition between Chol and oxysterols affects Chol/sphingolipids interactions in the context of lipid rafts formation in membranes. Also to what extent these interactions would be affected at physiologically relevant temperatures still needs to be investigated. Because highly specialized processes are believed to occur in these microdomains, subtle changes in phase behavior may have far reaching implications for proper membrane function. The results of the BAM images of the pure sterol monolayers in the collapse region are also highly significant as they show differences in crystallization. This can have implications in the pathology of diseases associated with oxysterol deposits.

5. Chapter : Dependence on the Condensing and Ordering Effects on Fluid and Condensed Saturated Phosphatidylcholines in mixed films with Cholesterol, 7-Ketocholesterol and  $5\beta,6\beta$ -Epoxycholesterol

While numerous studies have investigated sterol/phospholipid interactions, many questions still remain. In trying to address some of these issues, several models have been proposed to describe their interactions in mixed monolayers that include the super lattice model, the condensed-complex model, and the umbrella model.<sup>127, 140, 141</sup> With respect to the condensed-complex model, McConnell et al. predicted the existence of stable complexes of defined stoichiometry between Chol and phospholipids. While many studies are in agreement with the condensed-complex model, differences still remain with respect to stoichiometry as it has been indicated that it depends on the kind of phospholipids/sterol and the physical state of their monolayers.<sup>116</sup> Apart from model studies into sterol-phospholipid interactions, McMullen et al., with the use of differential scanning calorimetry (DSC), investigated a saturated homologous series of PCs with Chol and determined the effective length of Chol corresponded to a 17-carbon (C) all-trans acyl chain. They then went on to illustrate that the hydrophobic mismatch

(i.e., the difference in the hydrophobic length of the interacting molecules) had a great impact on the interaction between Chol and PCs. It is important to note, that these Chol/PC interactions are highly dependent on the molecular structure of Chol. Studies have shown that when the molecular structure of Chol is modified, there are implications that can affect lipid-lipid and lipid-protein interactions.<sup>10, 142 21, 143</sup>

In this work, the effect of PC acyl chain length (C12, C14, C18, and C20) on the interfacial behavior and domain morphology of mixed PC/sterol (Chol, 7-KChol, and 5,6 $\beta$ -EChol) monolayers with different sterol composition are systematically investigated using compression isothermal measurements and Brewster angle microscopy. To the author's knowledge, no systematic study has been done to understand the effects of all three sterols in mixed monolayers with the PCs used in this study. Questions therefore still remain as to how the interfacial behavior of commonly occurring phospholipids are affected by the additional oxygen moiety in oxysterols and therefore needs to be addressed.

To help the reader, the result and discussion sections will be separated into two sections, the first section will focus on DLPC and DMPC and the other on DSPC and DAPC.

## 5.1 Materials

1,2-Dilauroyl-*sn*-glycero-phosphocholine (DLPC, >99%), 1,2-dimyristoyl-*sn*-glycero-3-phosphocholine (DMPC, 99%), 1,2-disteroyl-*sn*-glycero-3-phosphocholine (DSPC, >99%), 1,2-diarachidoyl-*sn*-glycero-3-phosphocholine (DAPC, 99%), 7-ketocholesterol

(7-KChol, >99%), and 5 $\beta$ ,6 $\beta$ -epoxycholesterol (5,6 $\beta$ -EChol, >99%) were purchased from Avanti Polar Lipids (Alabaster, AL), whereas cholesterol (Chol, >99%) was from Sigma-Aldrich (St. Louis, MO). Lipid and sterol stock solutions (1 mM) were prepared in chloroform (HPLC grade,  $\geq$ 99.0%, Fisher Scientific, Pittsburgh, PA). Mixed solutions of desirable compositions were prepared from their respective stock solutions. Ultrapure Milli-Q water (18.2–18.3 M $\Omega$ -cm, pH 5.6) was used as aqueous subphase and was obtained from a Barnstead Nanopure system (model D4741, Barnstead/ThermoFisher Corporation, Dubuque, IA) equipped with additional organic removing cartridges (D5026 Type I ORGANIC free Cartridge Kit; Pretreat Feed).

## 5.2 Results and Discussion. Part I

### 5.2.1 Surface Pressure-Area Isotherms of Pure DLPC, DMPC, and Sterols Monolayers

Compression isotherms of the pure Chol, 7-KChol and 5,6 $\beta$ -EChol monolayers are shown in Fig. 5.1. The lift-off values of the pure sterols follow the trend 7-KChol > 5,6 $\beta$ -EChol > Chol. The larger lift-off values of the oxysterol monolayers are the result of increased electrostatic repulsion and steric hindrance between oxysterol molecules. This is induced by the hydrophilicity and added bulkiness of the additional oxygen atom. Discernible differences in the isotherm slopes of the sterols are also observed and follow the trend Chol > 5,6 $\beta$ -EChol > 7-KChol. The additional oxygen moiety therefore increased disorder within the oxysterol monolayer. The slope reduction of the 7-KChol isotherm has been documented previously and has been attributed to the polar ketone

group preferring to be hydrated by the aqueous phase.<sup>22, 32</sup> These studies also suggested tilting of the 7-KChol monolayer from the surface normal. While it appears that these changes are subtle, they do indicate different packing geometries in the monolayer of the sterols.

Regarding the isotherms of the pure DLPC and DMPC monolayers, the lift-off values of both PCs are  $\sim 94 \text{ \AA}^2/\text{molecule}$ , however, the collapse surface pressure of DMPC is  $\sim 4 \text{ mN/m}$  higher than that of DLPC. The difference in collapse pressure can be explained by the difference in main phase transition temperatures ( $T_m$ ) of these two PCs. The temperature recorded during these measurements ( $22 \pm 1 \text{ }^\circ\text{C}$ ) lies well above the transition temperature of DLPC ( $T_m \sim -2 \text{ }^\circ\text{C}$ ), but closer to that of DMPC ( $T_m \sim 23 \text{ }^\circ\text{C}$ ).<sup>144</sup> The increased  $T_m$  with DMPC is the result of increased van der Waals interactions due to the longer acyl tails. Even with this increased van der Waals interactions in the DMPC monolayer, both PC form a liquid-expanded monolayer without any visible transition throughout or even prior to the collapse phase. Lipid monolayers that are in a liquid-expanded (LE) phase are characterized by flexible disordered hydrocarbon tails with many gauche defects that are undergoing rapid axially symmetric reorientation.<sup>145</sup>

The influence of sterol type and concentration on the interfacial behavior of DLPC and DMPC monolayers were analyzed with each of the PCs mixed with Chol, 7-KChol and 5,6 $\beta$ -EChol shown in Fig. 5.1. Looking at the isotherms, it seems that all three sterols exert a condensing effect on both PCs monolayers. Further analysis with regards to the mixed DLPC/sterol monolayers with increasing sterol molar composition ( $0.1 \leq X_{\text{sterols}} \leq 0.7$ ) reveals progressively smaller lift-off values and increasing slopes that appear to

approach that of the pure sterol isotherms. In the mixed DMPC/sterol monolayers with increasing composition ( $0.1 \leq X_{\text{sterol}} \leq 0.9$ ), similar effects to those observed for the mixed DLPC/sterol monolayers are apparent, however, smaller concentrations of sterol are required to condense and order the monolayers. For instance, a glance of the DLPC/Chol and DMPC/Chol isotherms at  $X_{\text{sterol}} = 0.5$  reveals the difference in condensing and ordering abilities (Fig. 5.1A,D).

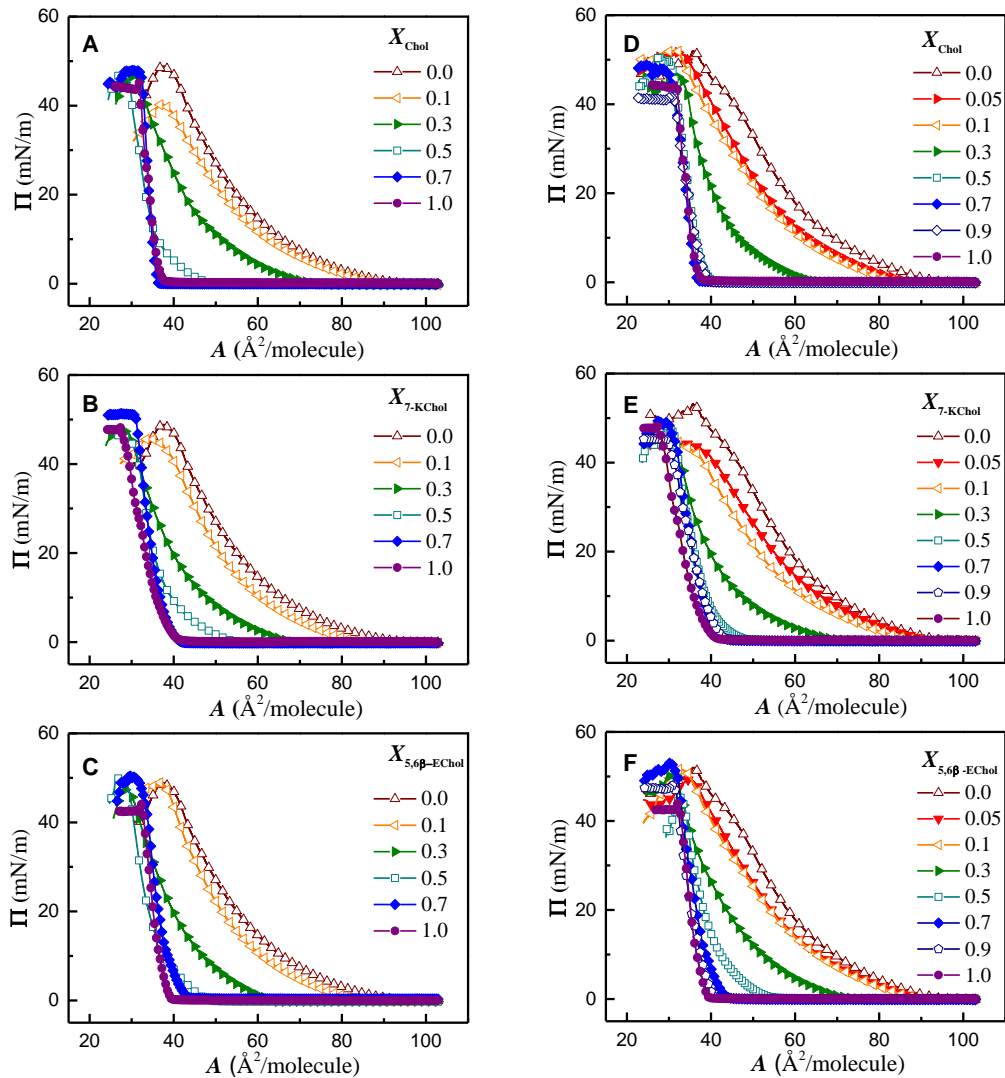


Figure 5.1 Compression isotherms of (A) Chol, (B) 7-KChol, (C), 5,6 $\beta$ -EChol mixed with DLPC monolayers. Compression isotherms of (D) Chol, (E) 7-KChol, (F), 5,6 $\beta$ -EChol mixed with DMPC monolayers.

### 5.2.2 Condensing Effect

To have a clearer understanding of the interactions between sterols and PCs, the condensing effect caused by the presence of the sterols in mixed monolayers of DLPC and DMPC was analyzed by plotting the excess molecular area ( $\Delta A_{\text{exc}}$ ) obtained directly

from the isotherms as a function of sterol composition at fixed surface pressures ( $\Pi = 3$  to  $40$  mN/m) shown in (Fig 5.2). This large surface pressure range was selected to provide detailed information on the physical state of the PC monolayer with the condensing effect. For all the mixtures of DLPC/sterol and DMPC/sterol, negative excess areas values are obtained indicating attractive interactions occurring within all investigated PC/sterol monolayers. As shown in Fig. 5.2, the magnitude of these interactions is dependent on sterol type and surface pressure. Further analysis reveals that, at the smallest surface pressure analyzed ( $3$  mN/m) and equimolar composition for DLPC/ $5,6\beta$ -EChol, the excess molecular area is significantly more negative than those of mixed DLPC/Chol and DLPC/ $7$ -KChol monolayers. From this observation, it can be inferred that  $5,6\beta$ -EChol had the greatest impact on condensing the DLPC monolayer. In contrast, analysis of the DMPC/sterol monolayer at the same surface pressure and equimolar composition shows the most negative excess area value with Chol.

To further verify the condensing effect by the sterols in the mixed DLPC and DMPC monolayers, the partial molecular area of PC ( $A_{PC}^*$ ) is also plotted in Fig. 5.3. For DLPC/sterol at  $3$  mN/m, the increased concentrations of sterols cause a significant reduction in the mean area occupied by DLPC (Fig. 5.3A). Previously, the excess molecular area results for DLPC with  $X_{sterol} = 0.5$ , indicated that  $5,6\beta$ -EChol demonstrates the greatest condensing ability. However, at  $X_{sterol} = 0.5$ , the  $A_{PC}^*$  values are equivalent for both Chol and  $5,6\beta$ -EChol therefore suggesting that both sterols condense the DLPC monolayer equally. The discrepancy between the excess and partial molecular areas clearly indicates that Chol occupies a larger area when mixed with DLPC. One

probable explanation may reside in the fact that Chol displays a larger tilt angle from the surface normal. In a previous study, McMullen et al. used high-sensitivity differential scanning calorimetry to investigate the effects of Chol on the thermotropic phase behavior of a homologous series of linear saturated PCs.<sup>146</sup> From their results, they determined that the hydrophobic thickness of Chol was equivalent to the length of diheptadecanoylphosphatidylcholine, a 17 acyl chain PC with a mean hydrophobic length of 17.5 Å. They also then went on to show that as the PC length deviated from "ideal" PC chain length, Chol changed the thermotropic phase behavior of the PC monolayer in a chain length-dependent manner. It was inferred that these changes were attributed to the hydrophobic mismatch between the PC and Chol. Between DLPC and Chol, it is clear that the hydrophobic mismatch between the two is large. One can expect that at low surface pressures, the hydrophobic part of Chol will prefer to tilt and interact with DLPC instead of residing almost parallel to the surface normal where they will be a larger hydrophobic gap between the two components.<sup>147, 148</sup>

Analysis of the mixed DLPC/7-KChol at the same surface pressure and equimolar sterol concentration illustrates that the excess molecular area is approximately the same as that of DLPC/Chol (Fig. 5.2B); however, the partial molecular area is slightly larger (Fig. 5.3A). Without a doubt, 7-KChol is clearly the least capable of the sterols at condensing DLPC at low surface pressures. As mentioned previously, the ketone group in 7-KChol is hydrophilic and prefers to be hydrated or to reside closer to the aqueous phase.<sup>129</sup> The small condensing ability suggests a tilting of the 7-KChol molecule from the surface normal as well as reduced attractive interactions with DLPC. Partial

molecular area analysis for DMPC/sterol at 3 mN/m and equimolar composition shows that the area occupied by DMPC is smallest when mixed with Chol and largest with 7-KChol (Fig. 5.3D–F); this trend also follows the excess area values indicating a true condensing effect. It can be concluded from this result that the reduced hydrophobic mismatch from DLPC to DMPC increased the stability of the PC/Chol monolayer at low surface pressures.

At higher surface pressures (20, 30, and 40 mN/m), for both DLPC and DMPC, the condensing effect is still quite evident. For instance, at the highest surface pressure analyzed (40 mN/m), the excess area values in the mixed DLPC/sterol at  $X_{\text{sterol}} = 0.3$  follows the trend  $5,6\beta\text{-EChol} \approx 7\text{-KChol} > \text{Chol}$  (Fig. 5.2A–C) while in the same mixed DLPC/sterol at  $X_{\text{sterol}} = 0.5$ , the excess area trend changes to  $\text{Chol} > 5,6\beta\text{-EChol} > 7\text{-Chol}$  (Fig. 5.2A–C) with a similar result also in the  $A_{\text{PC}}^*$  values Fig. 5.3C. What is more interesting is that the DLPC area is not affected in the monolayer containing 7-KChol as the sterol concentration increased from 0.3 to 0.5 (Fig. 5.3B–C). This observation indicates that 7-KChol maximum condensing ability has been reached. With regards to the excess molecular area for the mixed DMPC/sterol monolayers at 40 mN/m and at  $X_{\text{sterol}} = 0.3$ , the trend follows  $7\text{-KChol} > 5,6\beta\text{-EChol} \approx \text{Chol}$  (Fig. 5.2D–F) whereas at  $X_{\text{sterol}} = 0.5$  the observed trend is  $\text{Chol} > 7\text{-KChol} \approx 5,6\beta\text{-EChol}$  (Fig. 5.2D–F), with Chol again demonstrating the smallest  $A_{\text{PC}}^*$  values at  $X_{\text{sterol}} = 0.5$  (Fig. 5.2D–F).

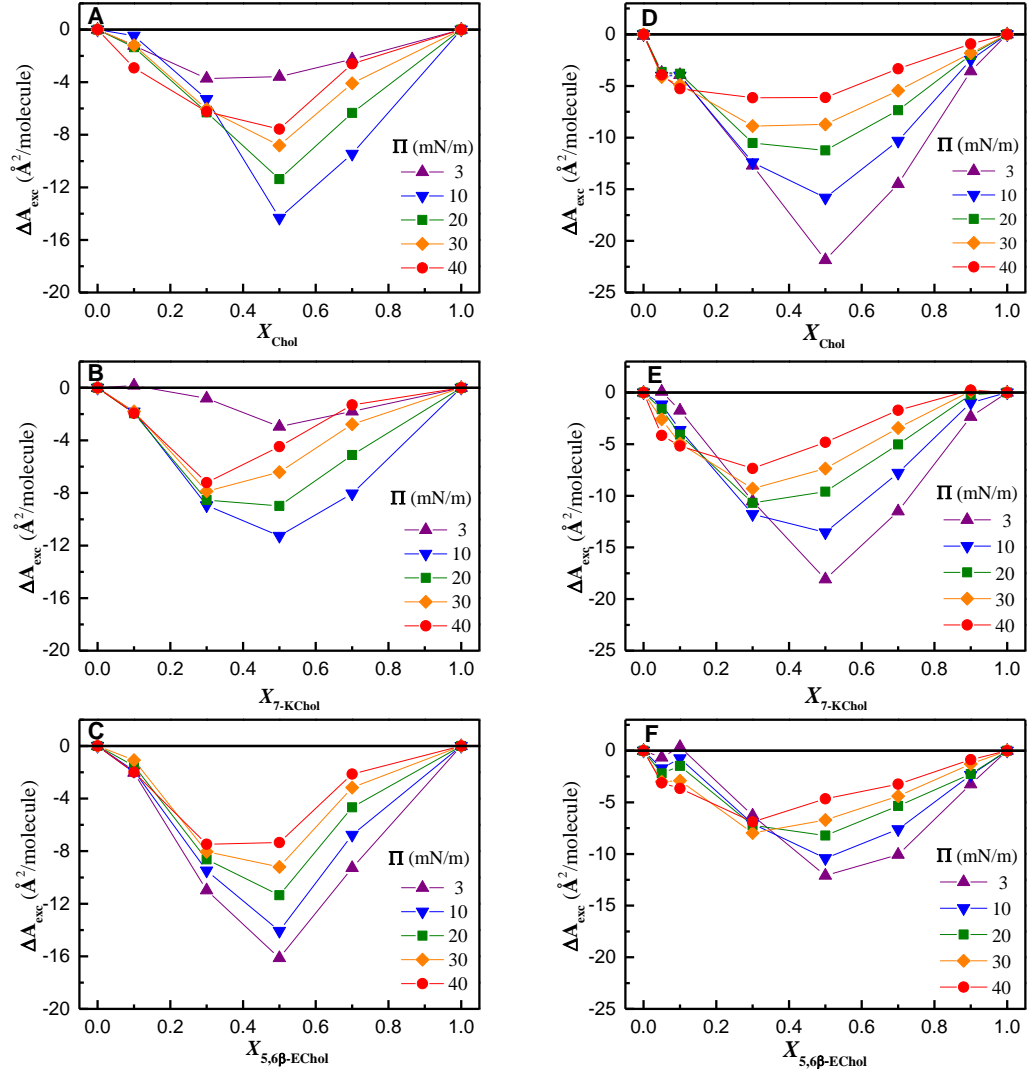


Figure 5.2 Excess molecular area with sterol composition for (A) Chol, (B) 7-KChol, and (C) 5,6 $\beta$ -EChol mixed with DLPC monolayers. Excess molecular area with sterol composition for (D) Chol, (E) 7-KChol, and (F) 5,6 $\beta$ -EChol mixed with DMPC monolayers.

Overall, the condensing effect appears to be significantly influenced by the hydrophobic mismatch between the PCs and sterols. This statement is supported by the observations made in the DLPC and DMPC mixed with Chol at 3 mN/m with  $X_{\text{sterol}} = 0.5$  (Figs. 5.2A,D and 5.3A,D). The strongest sterol condensing effects are found in the

mixed DMPC/sterol monolayers at 3 mN/m (Fig. 5.2D–F). This clearly results from the differences in the acyl chain length between DLPC and DMPC. It came as no surprise, however, that in the mixed DMPC/sterol monolayer, Chol demonstrated the largest condensing ability at low surface pressures because it is the most hydrophobic of the three sterols and therefore will preferential interact with the hydrophobic acyl tails of DMPC. At 40 mN/m, the maximum condensing ability is achieved at  $X_{7\text{-KChol}} = 0.3$  in both DLPC and DMPC (Figs. 5.2B,E), however, it is achieved at  $X_{5,6\beta\text{-EChol}} = 0.5$  when mixed with DLPC and  $X_{5,6\beta\text{-EChol}} = 0.3$  when mixed with DMPC (Figs. 5.2C,F). As for Chol, when mixed with both PCs, it achieves its maximum condensing ability at  $X_{\text{Chol}} = 0.5$  (Figs. 5.2A,D). Again, a probable explanation for these differences may come from the differences in the hydrophobic length of the three sterols, with Chol having the longest hydrophobic length, 5,6 $\beta$ -EChol having an intermediate hydrophobic length because of its reduced planarity, and 7-KChol preferring to reside closer to the aqueous phase.

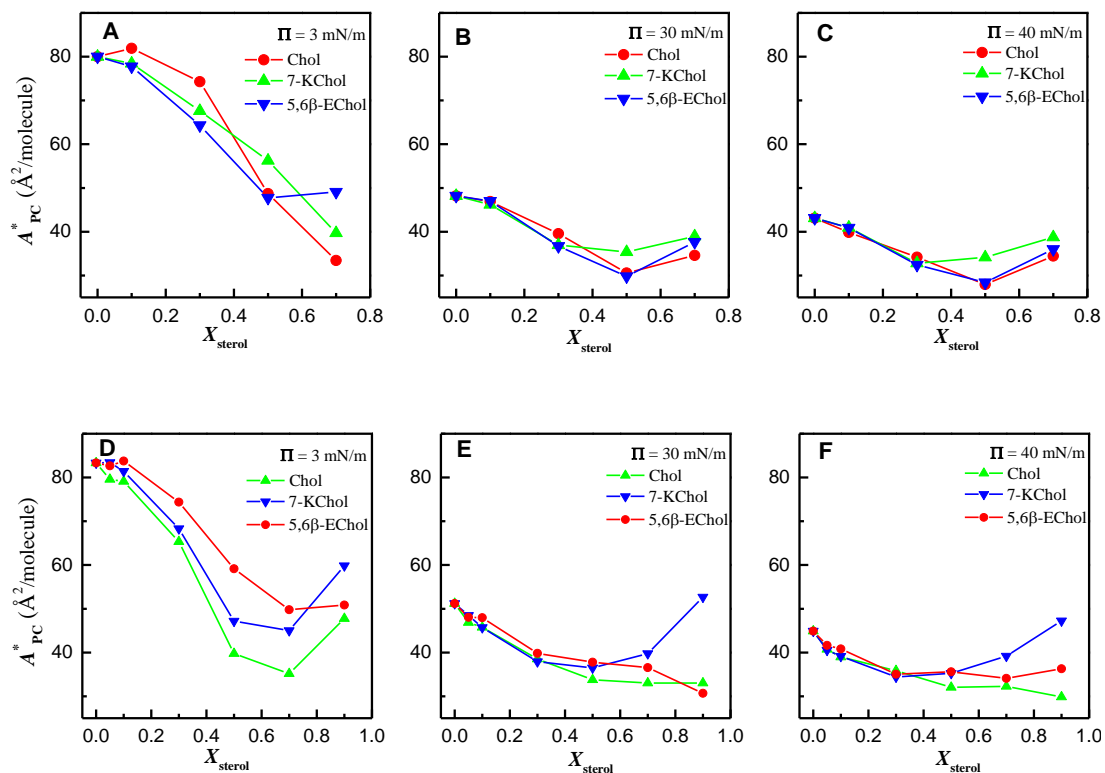


Figure 5.3 Partial molecular area with sterol composition for (A) Chol, (B) 7-KChol, and (C) 5,6 $\beta$ -EChol mixed with DLPC monolayers. Partial molecular area with sterol composition for (D) Chol, (E) 7-KChol, and (F) 5,6 $\beta$ -EChol mixed with DMPC monolayers.

### 5.2.3 Interfacial Area Compressibility Modulus of DLPC, DMPC, Sterols, and their Mixtures

To characterize the physical state of the monolayers, the compressibility modulus is calculated from the isotherm data and plotted as a function of surface pressure (Fig. 5.4). With regards to pure sterol monolayers, the highest compressibility moduli obtained were for Chol (615 mN/m) followed by 5,6 $\beta$ -EChol (248 mN/m) and 7-KChol (223

mN/m). With the PCs monolayers, both DLPC and DMPC, display maximum compressibility values of  $\sim 100$  mN/m, a value consistent with a LE phase.

The compressibility modulus data shows that pure DLPC and mixed DLPC/sterol monolayers with  $X_{\text{sterol}} \leq 0.3$  have similar interfacial rigidity and are therefore not affected by the addition of the sterols (Fig. 5.4A–C). However, at  $X_{\text{sterol}} = 0.5$  the compressibility modulus increased for all mixed DLPC/sterol monolayers which is an indication of an ordering effect. It is evident that at  $X_{\text{sterol}} = 0.7$ , Chol displays the greatest ability to order the PC acyl tails. The variation of the monolayer compressibility modulus with sterol composition was also monitored over the entire pressure range (3–40 mN/m) (Fig. 5.4D–F). With the addition of small amounts of sterols ( $X_{\text{sterol}} \leq 0.3$ ) there is little change in the compressibility modulus, however, moving from  $X_{\text{sterol}} = 0.3$  to 0.7, the compressibility modulus values of both mixed DLPC/7-KChol and DLPC/5,6 $\beta$ -EChol monolayers increase almost linearly at 20, 30, and 40 mN/m (Fig. 5.4E,F). In the mixed DLPC/Chol monolayers, however, the linear increase is more evident moving from  $X_{\text{sterol}} = 0.5$  to 0.7 within the same surface pressure range (Fig. 5.4D). These results here illustrate that all sterols have ordering capabilities in the DLPC monolayer. The observed changes in the ordering effect for the sterols also coincide with the sterol composition ( $X_{\text{sterol}} = 0.3$  and 0.5) for which the condensing effect was the strongest in the mixed monolayers.

The compressibility modulus values for pure DMPC and mixed DMPC/sterol monolayers are similar to those of mixed DLPC/sterol monolayers at  $X_{\text{sterol}} \leq 0.3$  (Fig. 5.5A–C). However, at  $X_{\text{sterol}} = 0.3$  there is an increase in the compressibility modulus

values in the mixed DMPC/Chol at  $\Pi > 15$  mN/m and a small increase in DMPC/5,6 $\beta$ -EChol at  $\Pi > 30$  mN/m (Fig. 5A and C), whereas the mixed DMPC/7-KChol monolayer appears unaffected (Fig. 5.5B). At  $X_{\text{sterol}} = 0.5$  the compressibility modulus increased for all the mixed DMPC/sterol monolayers. However, for  $0.5 \leq X_{\text{sterol}} \leq 0.7$  there are no significant increases in compressibility modulus values in mixed DMPC/oxysterol monolayers. The variation of compressibility with sterol composition shows little to no changes when  $X_{\text{sterol}} \leq 0.1$  for the mixed sterols and linearity is observed in the range  $0.3 \leq X_{\text{sterol}} \leq 0.7$ . In comparison to the results with DLPC, less Chol concentration is required to order the DMPC tails. However, the ordering effects were reduced at high Chol ratio in DMPC in comparison to DLPC. This may be the result of a smaller number of gauche defects in DMPC.

Overall, both oxysterols could not achieve large compressibility modulus values as those seen in the mixed monolayers with Chol. Also, in terms of relative compressibility modulus values between the oxysterols, the order of magnitude is approximately the same. It can therefore be inferred that the values are affected by the additional volume effect incurred because of the extra oxygen atom.

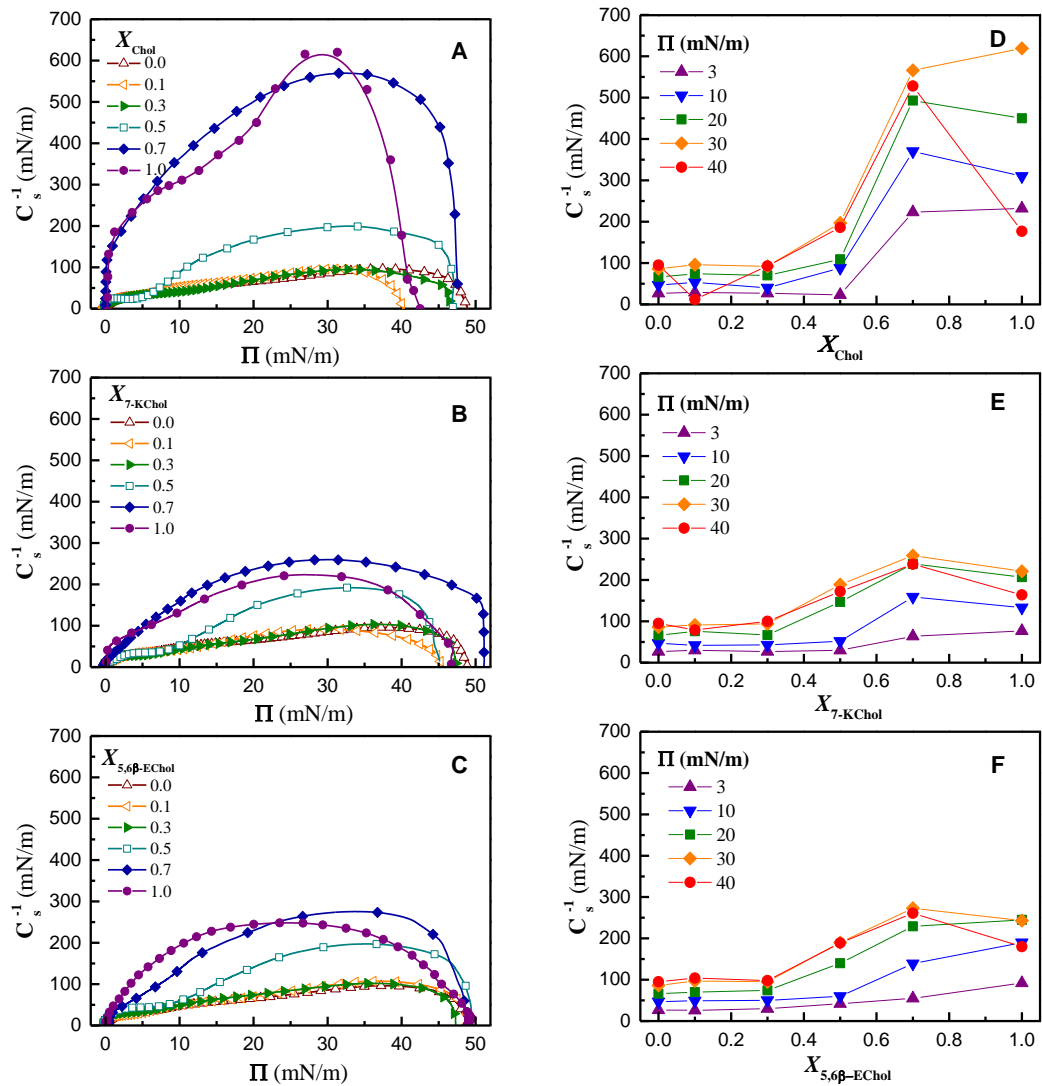


Figure 5.4 Variations of monolayer compressibility modulus with (A–C) surface pressure and (D–F) sterol composition for (A and D) Chol, (B and E) 7-KChol, and (C and F) 5,6 $\beta$ -EChol mixed with DLPC monolayers. The compressibility data was calculated from the compression isotherms shown in Fig. 5.1.

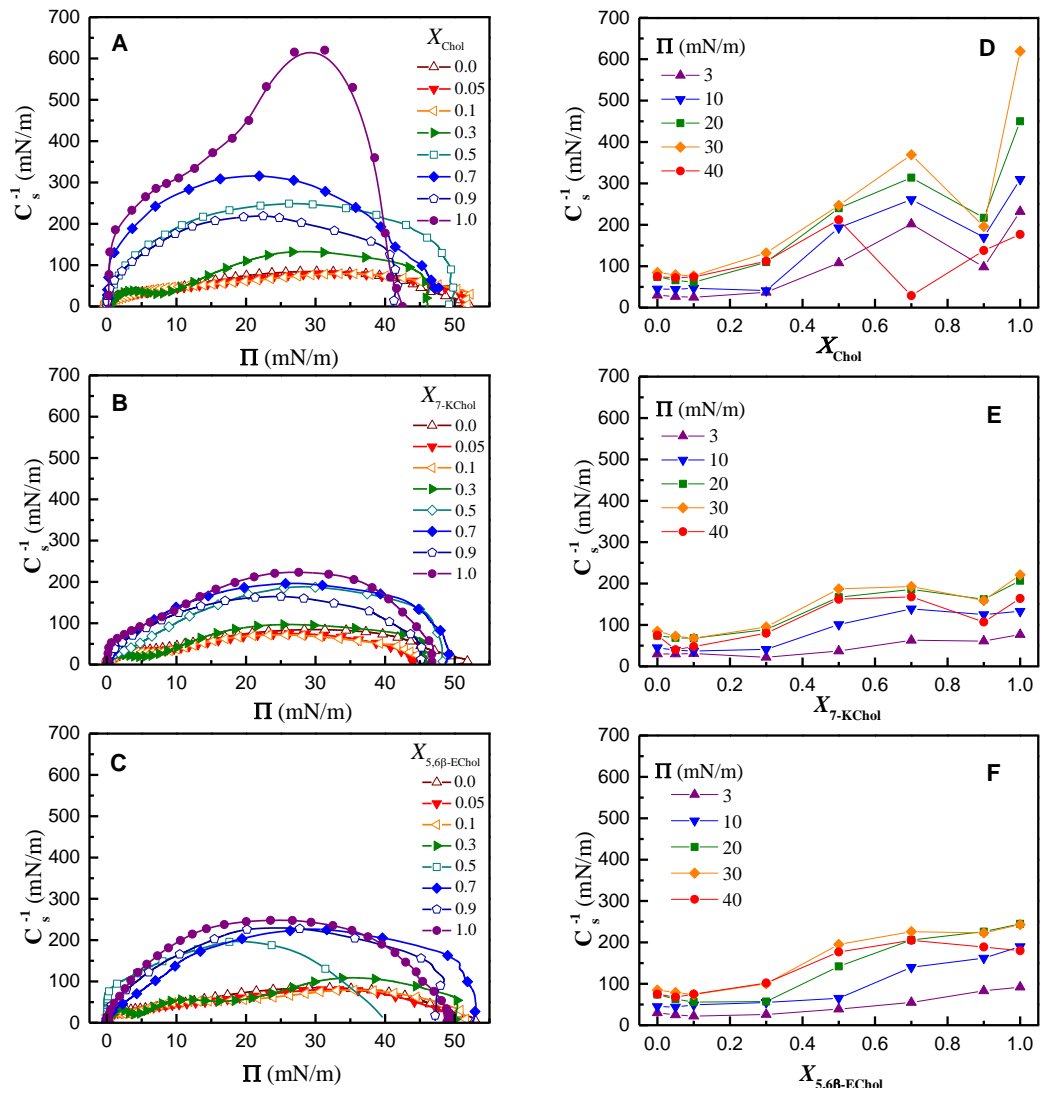


Figure 5.5 Variations of monolayer compressibility modulus with (A–C) surface pressure and (D–F) sterol composition for (A and D) Chol, (B and E) 7-KChol, and (C and F) 5,6 $\beta$ -EChol mixed with DMPC monolayers. The compressibility data was calculated from the compression isotherms shown in Fig. 5.1.

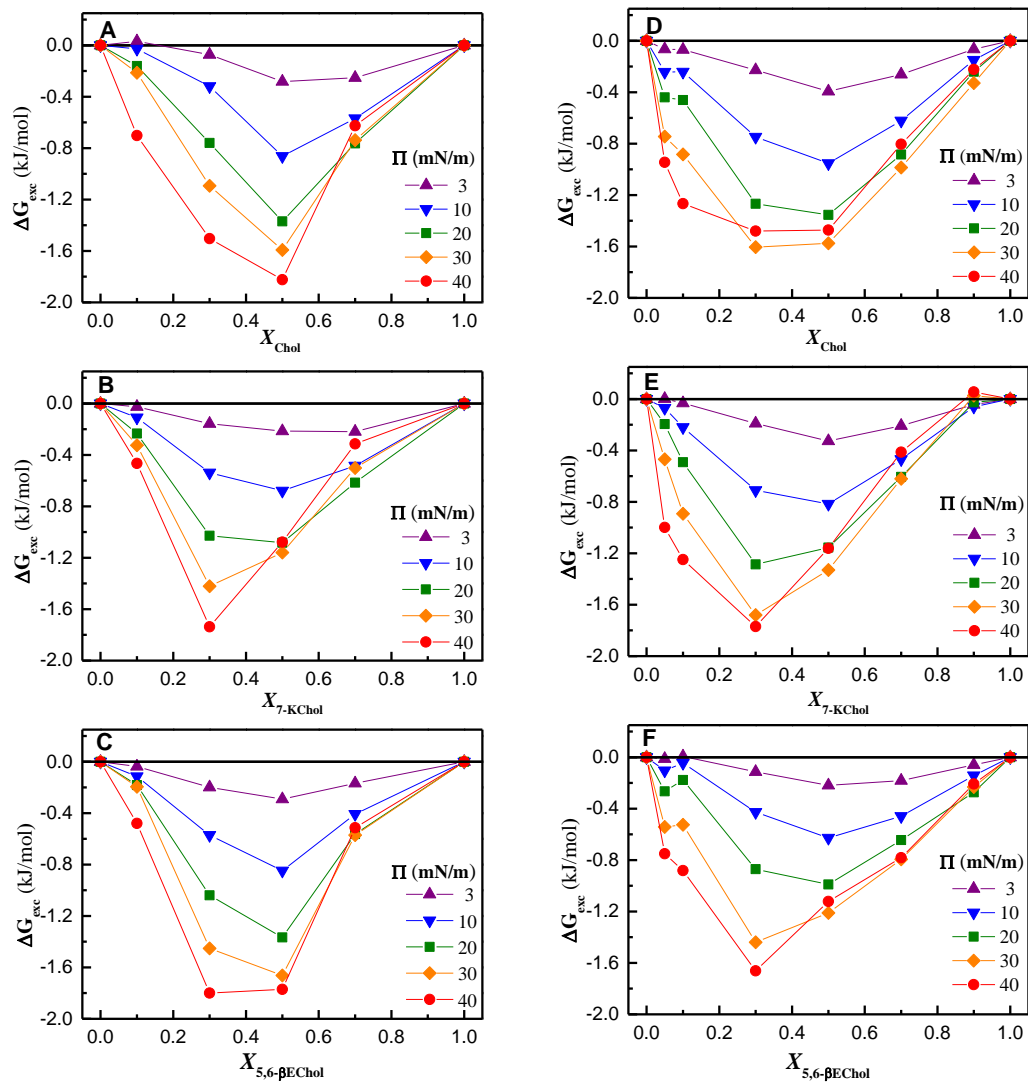


Figure 5.6 Variations of excess free energy of mixing of sterol composition for (A) Chol, (B) 7-KChol, and (C) 5,6 $\beta$ -EChol mixed with DLPC monolayers. Variations of excess free energy of mixing of sterol composition for (D) Chol, (E) 7-KChol, and (F) 5,6 $\beta$ -EChol mixed with DMPC monolayers.

#### 5.2.4 Excess Free Energy of Mixing of DLPC, DMPC, Sterols, and their Mixtures

The excess molecular area of the PCs mixed with the sterols is a rough indicator of interactions between the two components. The excess free energy of mixing ( $\Delta G_{exc}$ ) as function of sterol composition and in the same surface pressure range was used to quantify the deviation from ideality. Analysis of the excess free energy in the mixed DLPC/sterol monolayers over the entire surface pressure range demonstrate non-ideality for all three sterols and DLPC-sterol attractive interactions (Fig. 5.6A–C). The occurrence of a minimum implies that the influence of the molecular interactions on monolayer stability was the most significant at that composition. Analysis of the mixed DLPC/sterol monolayers at 3 and 10 mN/m reveals that the most attractive and stable interactions exist at  $X_{sterol} = 0.5$ . This result is consistent for the three sterols at these low surface pressures. As the surface pressure increase, differences are observed pertaining to their compositional stability. For instance, at higher surface pressures ( $\Pi \geq 20$  mN/m), the most attractive and stable interactions for the DLPC/Chol monolayer exists at  $X_{Chol} = 0.5$  (Fig. 5.6A). Clearly, for this particular monolayer, it can be postulated that the preferred DLPC:Chol stoichiometry is 1:1. Turning to the mixed DLPC/7-KChol monolayers at 30 and 40 mN/m, the stability shifts to  $X_{7-KChol} = 0.3$  (Fig. 5.6B); here it can be postulated that the preferred DLPC:7-KChol stoichiometry is 2:1. In the case of the mixed DLPC/5,6 $\beta$ -EChol monolayer at 30 mN/m, the stability is at  $X_{5,6\beta-EChol} = 0.5$ , but as the surface increased to 40 mN/m, both  $X_{5,6\beta-EChol} = 0.3$  and 0.5 display equal stabilities hence indicating that both 2:1 and 1:1 stoichiometries are equally preferred (Fig. 5.6C). At the surface pressure of 30 and 40 mN/m with  $X_{sterol} = 0.3$ , the following

trend is observed for the stability of the DLPC/sterol monolayers:  $5,6\beta\text{-EChol} > 7\text{-KChol} > \text{Chol}$ ; in contrast, at  $X_{\text{sterol}} = 0.5$  at 30 mN/m, the trend becomes  $5,6\beta\text{-EChol} > \text{Chol} > 7\text{-KChol}$ , and at 40 mN/m it changes to  $\text{Chol} > 5,6\beta\text{-EChol} > 7\text{-KChol}$ .

Analysis of the excess free energy of mixing in the mixed DMPC/sterol monolayers at lower surface pressures (3 and 10 mN/m) are thermodynamically most stable for all three sterols at  $X_{\text{sterol}} = 0.5$  (Fig. 5.6D–F). At higher surface pressures (30 and 40 mN/m) both 7-KChol and 5,6 $\beta$ -EChol are thermodynamically more stable at  $X_{\text{sterol}} = 0.3$ , whereas Chol illustrates dual thermodynamic stabilities at  $X_{\text{sterol}} = 0.3$  and 0.5.

It is believed that strong attractive interactions in binary mixed monolayers may be the result of the formation of stable condensed complexes.<sup>127</sup> If this is indeed the case, from the results shown here, it appears that the differences in the compositional stabilities are linked to surface complex stabilities formed within the monolayer. The  $\Delta G_{\text{exc}}$  values suggest that the preferred PC:sterol stoichiometry at high surface pressures are 1:1 in DLPC/Chol, 2:1 in DLPC/7-KChol, and both 2:1 and 1:1 in DLPC/5,6 $\beta$ -EChol. With DMPC the preferred stoichiometry in the same surface pressure range are both 2:1 and 1:1 in DMPC/Chol, and 2:1 in DMPC/7-KChol and DMPC/5,6 $\beta$ -EChol. In a molecular dynamics simulations study, Pandit et al. demonstrated that DLPC in a bilayer mixed with 40 % Chol had a tendency to complex in a 1:1 stoichiometry. In the same study, they also simulated DPPC in a mixed bilayer with Chol at the same concentration and observed the two molecules preferred to interact in a 2:1 PC:Chol ratio.<sup>149</sup> They then went on to postulate that the differences in the observed complexation of Chol with the two PCs were the result of different packing geometries due to the differing PC acyl

chain lengths. This can be explained as the shorter acyl chain of DLPC forms a thinner bilayer in comparison to DPPC and as such Chol molecules will be more tilted in DLPC because of the larger hydrophobic mismatch. Additionally, they were also able to determine that the PCs interact with Chol via an interconnected hydrogen bonding network and these interactions were less likely to occur in the mixed DLPC/Chol because of this increased Chol tilt. Because the most favorable association of DLPC/Chol found here is 1:1, it can be inferred that Chol is most likely tilted in the monolayer because of the hydrophobic mismatch and therefore cannot achieve the 2:1 stoichiometry. The 2:1 stoichiometry, however, is maintained in the mixed DLPC/7-KChol monolayer therefore suggesting a lesser hydrophobic mismatch than in DLPC/Chol. To prove this point even further, Smondyrev and Berkowitz in another stimulation study looked at the interactions between DPPC and 6-ketocholestanol, an analogue of 7-KChol, and determined that because of the ketone group, 6-ketocholestanol moves away from the bilayer center towards the polar region of the phospholipid headgroups.<sup>129</sup> Also, another interesting observation is that in the mixed DLPC/5,6 $\beta$ -EChol both 1:1 and 2:1 stoichiometries appear to be equally favored. From the DMPC/sterol results, 7-KChol still maintains the 2:1 stoichiometry, while 5,6 $\beta$ -EChol only retains the 2:1 stoichiometry and Chol displays dual stoichiometries. The results here show that the 2:1 PC/sterol stoichiometry is dependent on the effective hydrophobic length of the PC.

### 5.2.5 BAM Images of DLPC, DMPC, Sterols, and their Mixtures

Figure 5.7 shows BAM images of pure DLPC and DLPC/Chol monolayers with  $X_{\text{Chol}} = 0.3\text{--}0.7$  and Chol at different stages of compression. The pure DLPC monolayer appears homogeneous throughout the compression only increasing in reflectivity as the surface pressure increased; this observation is quite characteristic of the LE phase. The characteristic domain morphology of Chol is also observed at low surface pressures ( $\sim 0$  mN/m) with a gas and condensed phase. As increasing amounts of Chol is added to the DLPC monolayer, the BAM images begin to appear similar to those of pure Chol. The Chol ratio where this transition occurred, however is at  $X_{\text{sterol}} = 0.7$ . Further analysis of the BAM at  $X_{\text{Chol}} = 0.3$  and  $0.5$ , illustrate heterogeneity, particularly at  $X_{\text{Chol}} = 0.5$ . The BAM images of DLPC/7-KChol (Fig. 5.8) and DLPC/5,6 $\beta$ -EChol (see Appendix A) monolayers with increasing concentration of sterols also take on the appearance of their respective pure sterol monolayer. However, in comparison to Chol, visual similarities with their pure sterol monolayers are observed at  $X_{\text{sterol}} = 0.5$ .

The BAM images of the mixed DMPC/sterol (Fig. 5.9–5.10) demonstrates some similarities with those seen in DLPC, however, heterogeneity in the mixed DMPC/Chol monolayers is only observed with  $X_{\text{sterol}} = 0.3$  (Fig. 5.9) and at  $X_{\text{sterol}} = 0.5$ , it takes on the appearance of the pure Chol monolayer. Small concentrations of Chol in PC monolayers are known to mix uniformly.<sup>9, 150</sup> However, as the concentration of Chol increases, phase separation occurs to form Chol-rich and Chol-poor microdomains. Previous studies have also indicated that phase separation varies as a function of acyl chain length, monolayer composition and surface pressure.<sup>127, 150</sup>

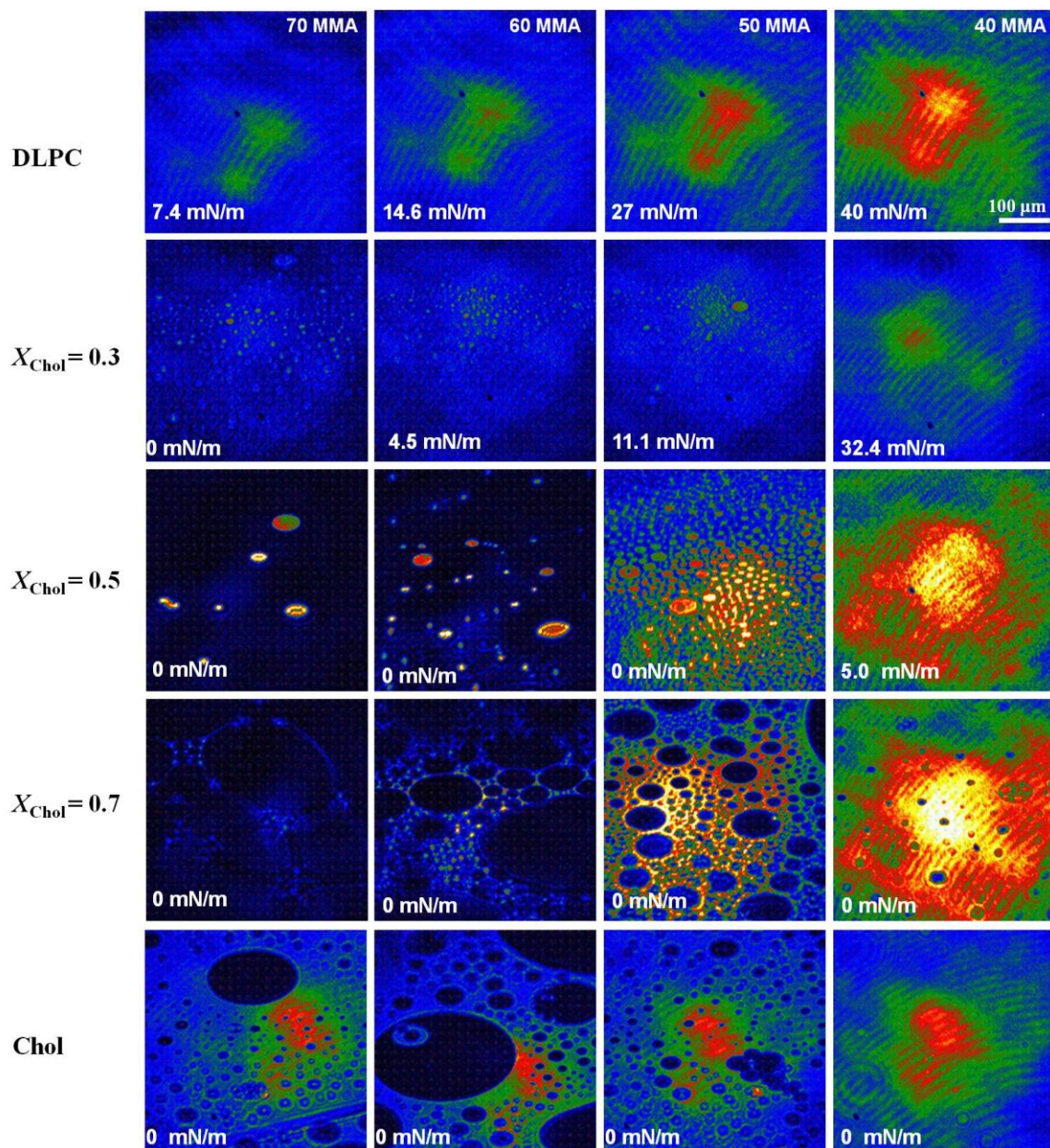


Figure 5.7 BAM images of DLPC and DLPC/Chol monolayers with  $X_{\text{Chol}} = 0.3\text{--}0.7$  and Chol at different stages of compression. Numbers in the lower left and upper right corners indicate the mean molecular area and the surface pressure, respectively.

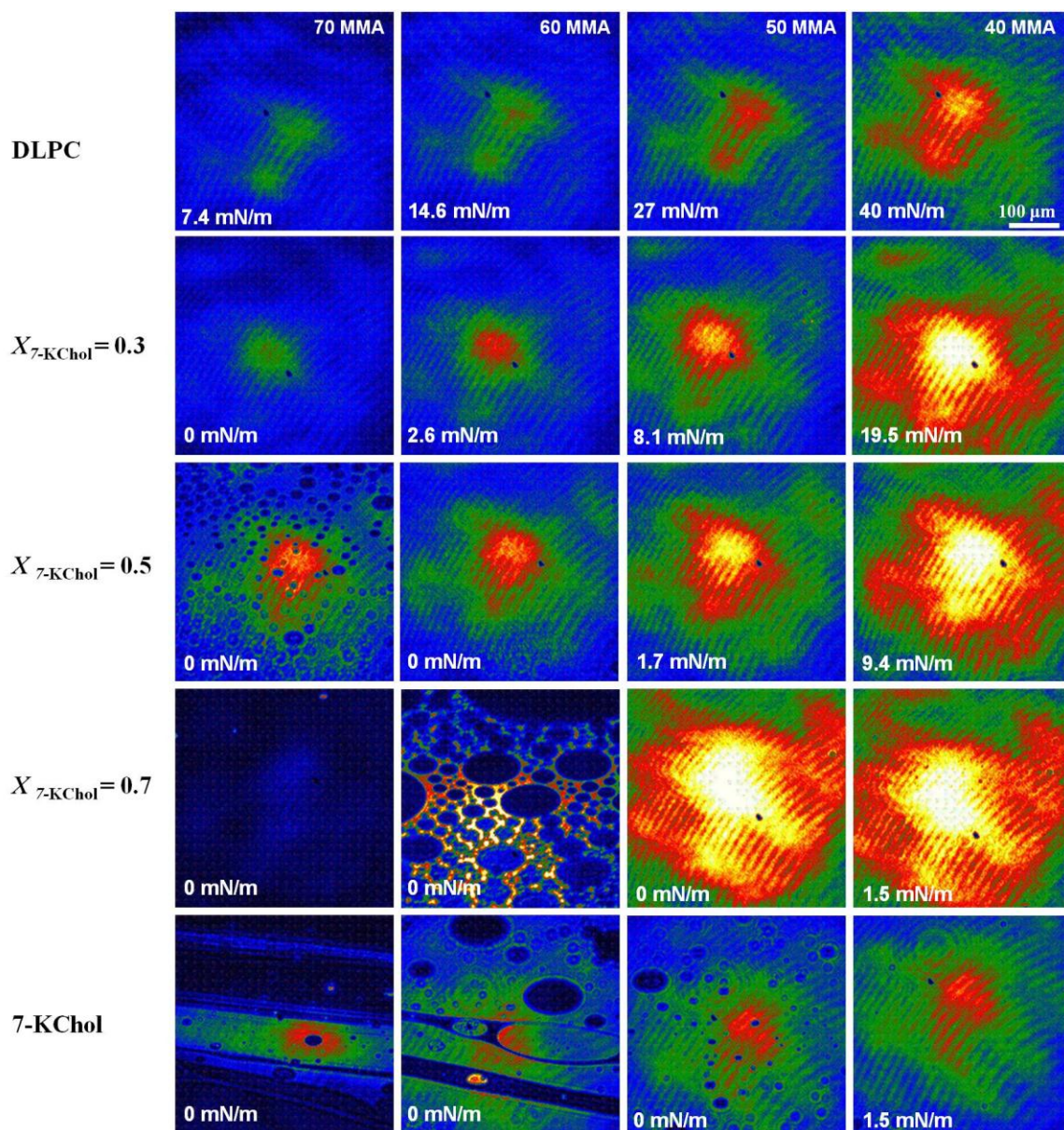


Figure 5.8 BAM images of DLPC and DLPC/7-KChol monolayers with  $X_{7\text{-KChol}} = 0.3\text{--}0.7$  and 7-KChol at different stages of compression. Numbers in the lower left and upper right corners indicate the mean molecular area and the surface pressure, respectively.

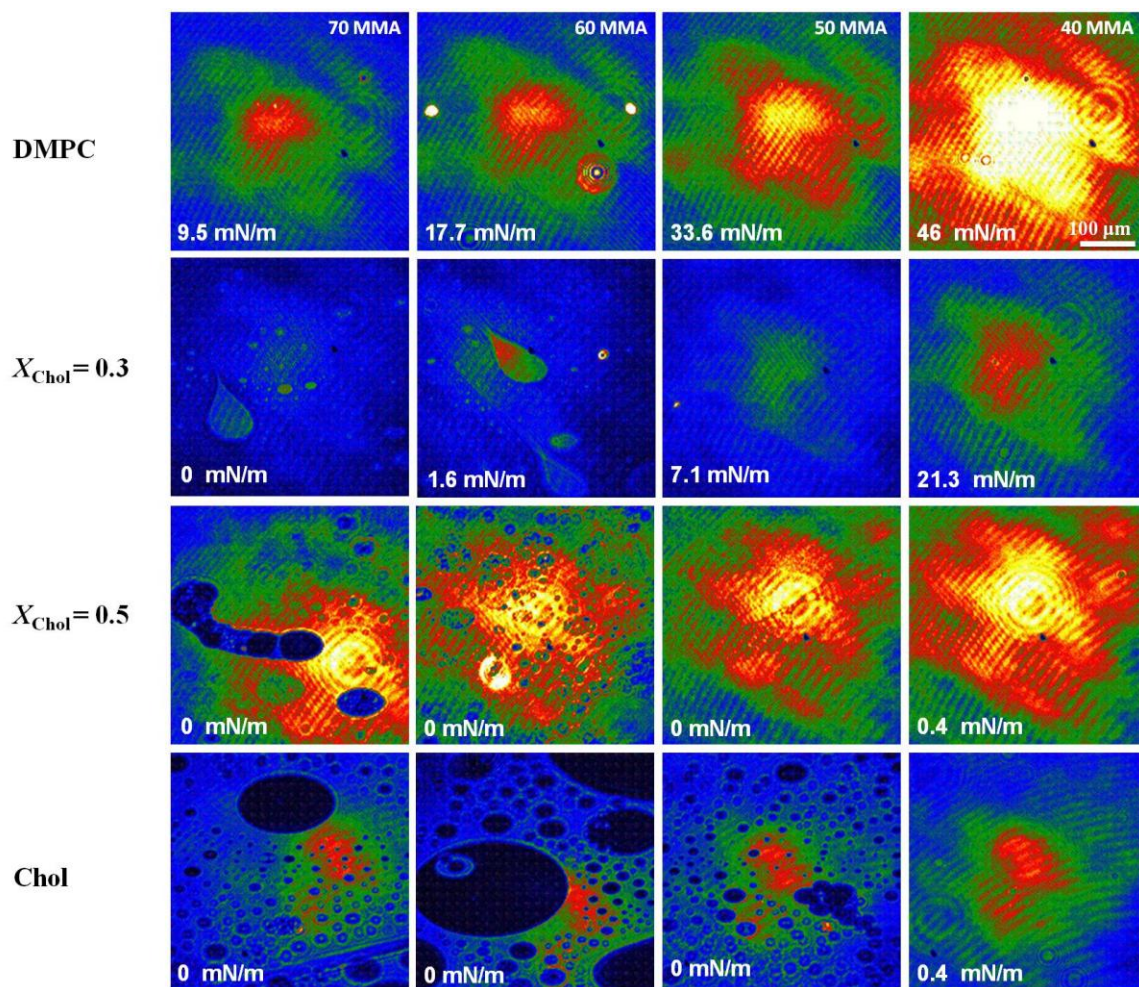


Figure 5.9 BAM images of DMPC and DMPC/Chol monolayers with  $X_{\text{Chol}} = 0.3\text{--}0.5$  and Chol at different stages of compression. Numbers in the lower left and upper right corners indicate the mean molecular area and the surface pressure, respectively.

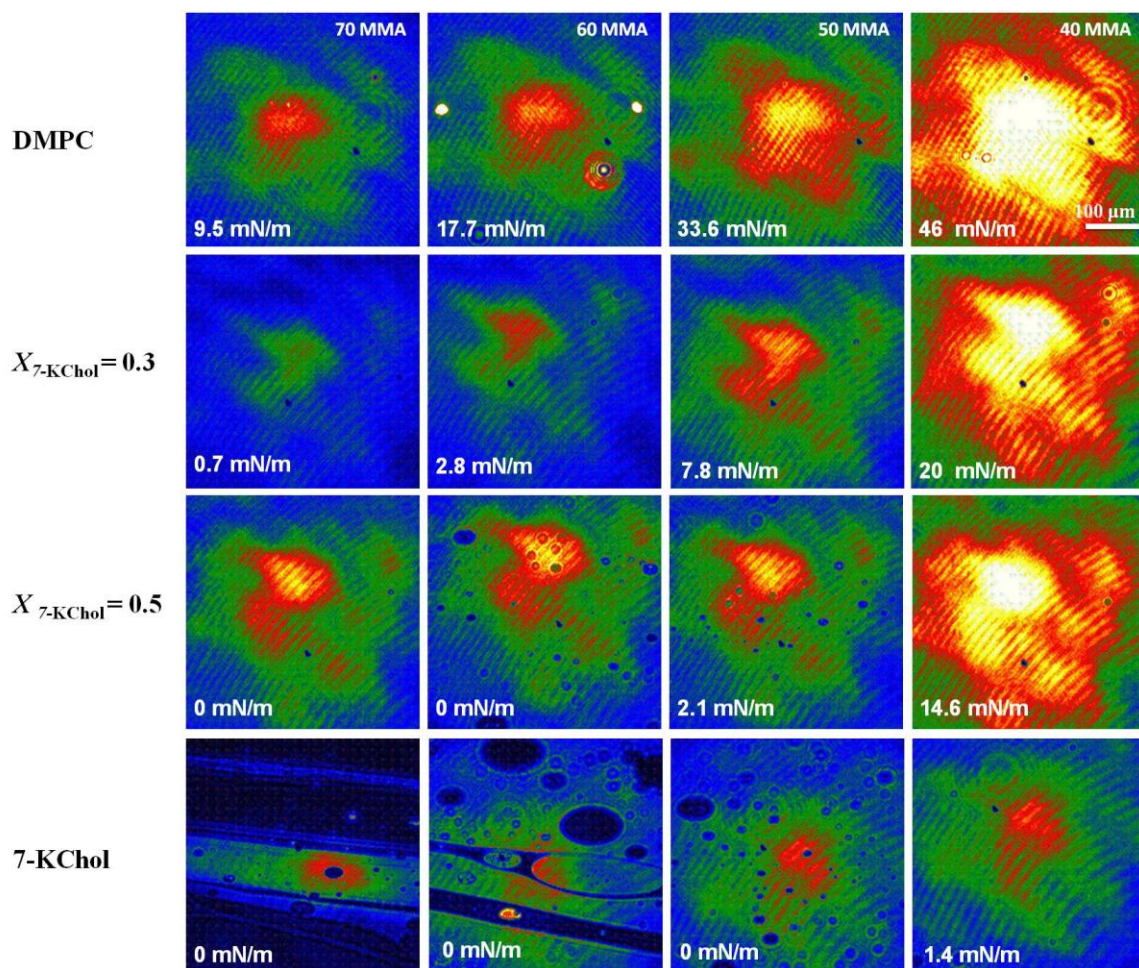


Figure 5.10 BAM images of DMPC and DMPC/7-KChol monolayers with  $X_{7\text{-KChol}} = 0.3\text{--}0.5$  and Chol at different stages of compression. Numbers in the lower left and upper right corners indicate the mean molecular area and the surface pressure, respectively.

## 5.3 Results and Discussion. Part II

### 5.3.1 Surface Pressure-Area Isotherms of Pure DSPC, DAPC, and their Mixtures with Sterols

Compression isotherms of the pure DSPC and DAPC monolayers, and their mixtures with the sterols are shown in Fig. 5.11. The lift-off ( $54 \text{ \AA}^2$ ) and collapse surface pressure ( $60 \text{ mN/m}$ ) values for both pure PCs monolayers are approximately the same. At room temperature, both PCs are below their main phase transitions with  $T_m \sim 55$  and  $\sim 66$  °C and for DSPC and DAPC, respectively.<sup>151</sup> Concerning the physical state of the monolayers, this means that both PCs monolayers are in the solid phase with highly ordered acyl tails. Upon the addition of sterols to DSPC, the isotherms shifted to smaller areas (Fig. 5.11A–C). In the case of DAPC, however, the isothermal curves are drastically affected by the presence of oxysterols as can be seen by the appearance of a plateau at  $X_{\text{sterol}} = 0.3$ , typically indicative of a first order phase transition (Fig. 5.11D–F).

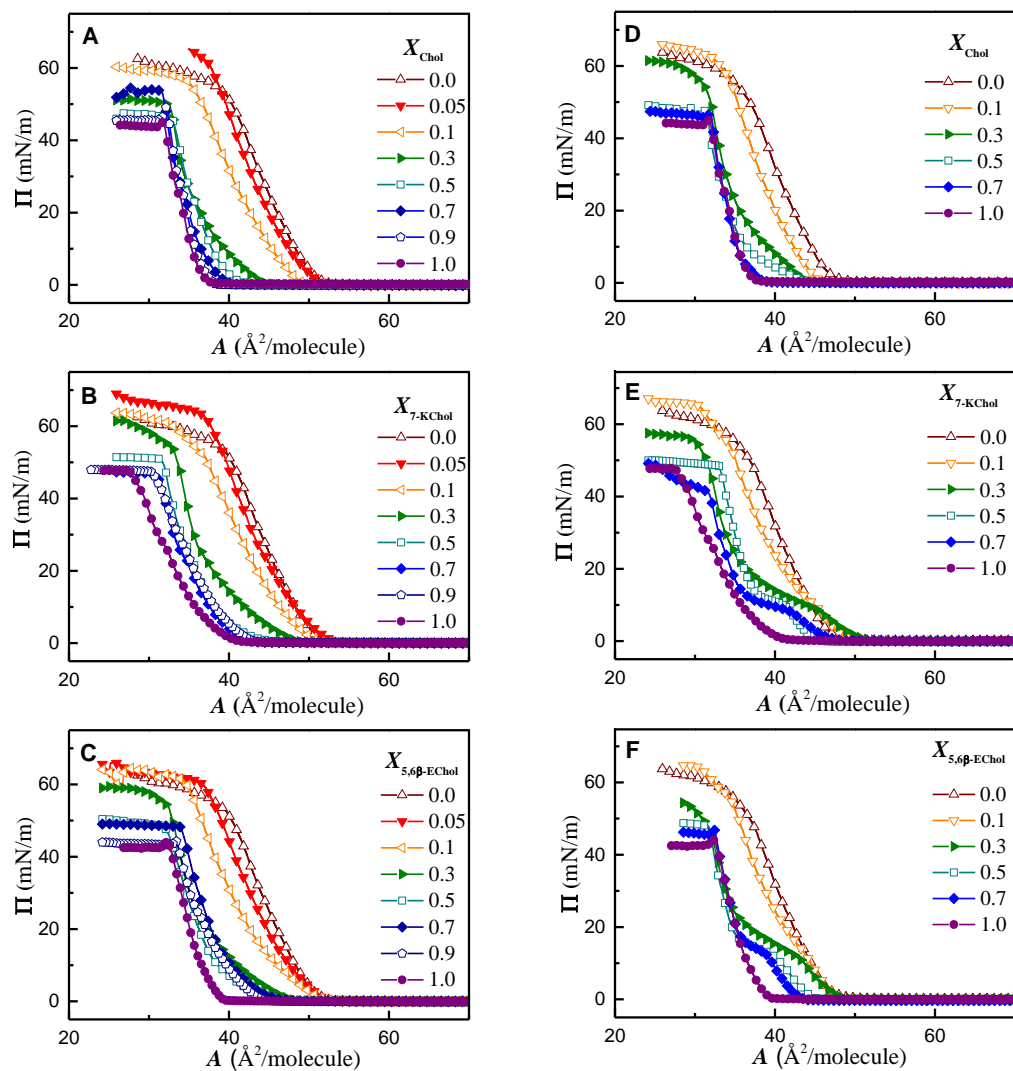


Figure 5.11 Compression isotherms of (A) Chol, (B) 7-KChol, (C), 5,6 $\beta$ -EChol mixed with DSPC monolayers. Compression isotherms of (D) Chol, (E) 7-KChol, (F), 5,6 $\beta$ -EChol mixed with DAPC monolayers.

### 5.3.2 Condensing Effect

In mixed DSPC/sterol monolayers, small positive excess area per molecules values are observed at 3 and 10 mN/m ( $X_{\text{sterol}} \leq 0.1$ ) indicating repulsive interactions between the components (Fig. 5.12A–C). As the sterol concentration increased to  $X_{\text{sterol}} = 0.7$ , positive excess area values are only observed. Moving on to the mixed DAPC/sterol monolayers, at 3 and 10 mN/m, positive excess area values are found for almost all oxysterol ratios, however, the mixed DAPC/7-KChol monolayer displays the most positive values (Fig. 5.12D–F). It is noted that these positive values are significantly larger than those in the mixed DSPC/oxysterol monolayers. This observation is very important and indicates that the oxysterols have reduced solubility in DAPC in comparison to Chol. Positive excess area values may, at times, indicate that the components in a binary mixed monolayer might be immiscible or partially miscible.

Analysis of the partial molecular areas for DSPC/sterols shown in Fig. 5.13A–C are also consistent with the analysis of the excess molecular area that shows expansion of the DSPC area at  $X_{\text{sterol}} \geq 0.5$  in the low surface pressure region. However, the partial molecular area shown in Fig. 5.13D–F reveals a successive increase in the DAPC area in the mixed oxysterol monolayers for  $X_{\text{sterol}} \leq 0.3$  at low surface pressures, clearly showing reduced solubility of the oxysterols in DAPC. At high surface pressures ( $\Pi \geq 20$  mN/m), the excess area values are negative over the range  $0.1 \leq X_{\text{sterol}} \leq 0.7$  and are positive beyond it, except for Chol. Also in the mixed DSPC/sterol monolayers with  $X_{\text{sterol}} = 0.3$  at high surface pressures, the condensing ability follows the trend Chol > 5,6 $\beta$ -EChol > 7-KChol. Similar to DSPC, at higher surface pressures the excess area values of mixed

DAPC/sterol monolayers are negative practically at all sterol ratios and also demonstrated the same condensing ability trend (Fig. 5.13).

It is clear that the oxysterols display increased repulsive interactions as the PC chain length is increased, particularly at low surface pressures as observed in the DAPC monolayer. The increased repulsive interactions are the result of reduced miscibility of the oxysterols in DAPC. It appears that as the chain length increased from DSPC to DAPC, the stronger DAPC-DAPC interactions are preferred over DAPC-oxysterol interactions. Differences in the interactions between the respective oxysterols are observed because the DAPC/7-KChol interactions are less favorable. This may be due to the greater hydrophilicity of 7-KChol compare to 5,6 $\beta$ -EChol.

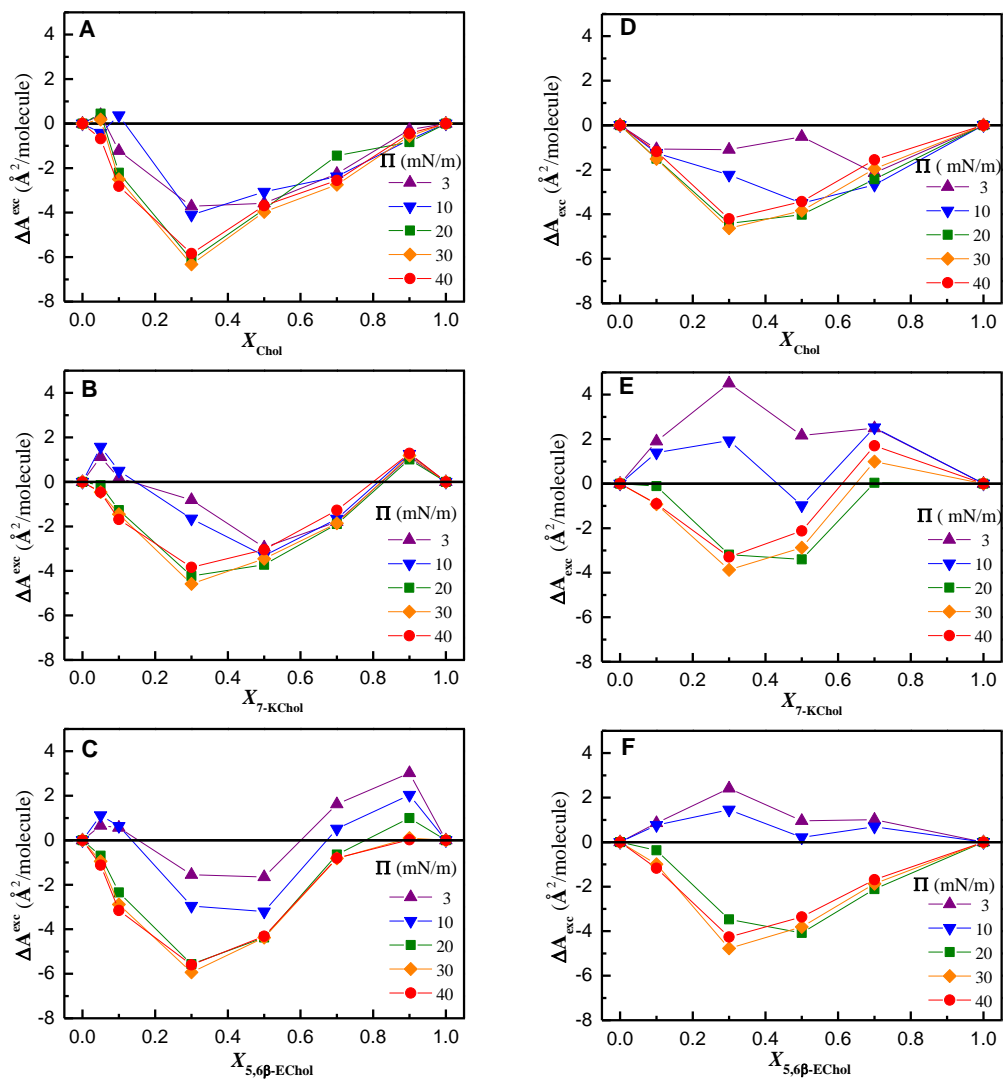


Figure 5.12 Excess molecular area with sterol composition for (A) Chol, (B) 7-KChol, and (C) 5,6 $\beta$ -EChol mixed with DSPC monolayers. Excess molecular area with sterol composition for (D) Chol, (E) 7-KChol, and (F) 5,6 $\beta$ -EChol mixed with DAPC monolayers.

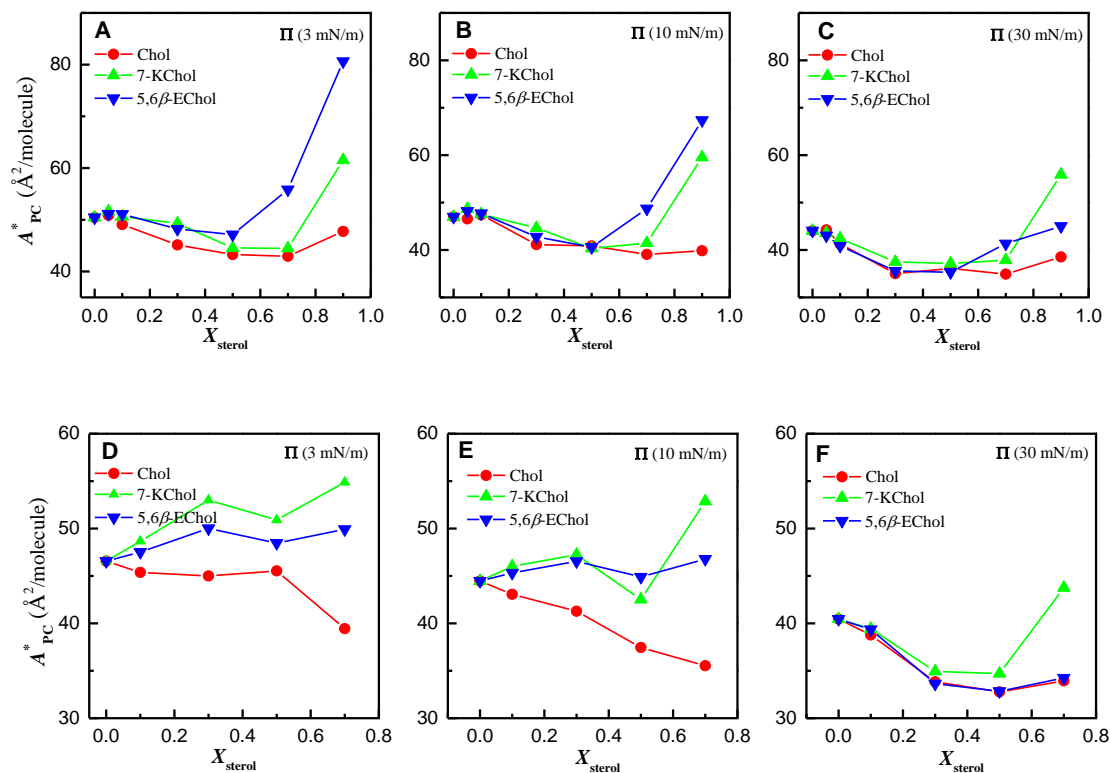


Figure 5.13 Partial molecular area with sterol composition for (A) Chol, (B) 7-KChol, and (C) 5,6 $\beta$ -EChol mixed with DSPC monolayers. Partial molecular area with sterol composition for (D) Chol, (E) 7-KChol, and (F) 5,6 $\beta$ -EChol mixed with DAPC monolayers.

### 5.3.3 Interfacial Area Compressibility Modulus of DSPC, DAPC, Sterols, and their Mixtures

In the mixed DSPC/oxysterol monolayers, it is apparent that there is no significant change in the compressibility values, particularly in the mixed DSPC/7-KChol monolayers (Fig. 5.13A–C). However, in the mixed DSPC/Chol monolayers at  $X_{sterol} = 0.3$ , a reduction in the compressibility modulus values is observed at low surface pressures followed by an inflection point at  $\Pi = 6$ – $15$  mN/m (Fig. 5.13A). Inflection

points in the curves are an indication of a change in order (or change in phase) of the PC acyl chains that is mediated by the surface pressure and the sterol concentration. As the concentration of Chol increased from  $X_{\text{Chol}}$  0.5-0.9, the compressibility modulus values continued to increase, and the inflection shifted to  $\Pi = 20\text{--}27$  mN/m. In terms of the compressibility modulus as a function of surface pressure, the results indicate a decrease in the compressibility modulus values at  $X_{\text{sterol}} \leq 0.3$  in a manner dependent on sterol type and surface pressure. From the compressibility modulus values at  $X_{\text{sterol}} = 0.3$ , Chol disorders the DSPC monolayer in comparison to the oxysterols.<sup>1</sup> This is not a surprise as Chol is known to induce disorder in solid phase lipids by interfering with the long-range order of the pure solid phase lipid.<sup>1, 146</sup> The mechanism behind Chol interfering with the solid phase revolves around the fact that it intercalates within the acyl tails and the PC headgroup regions where it reduces attractive interactions between the pure solid lipid component. In the range  $0.3 \leq X_{\text{sterol}} \leq 0.9$ , no significant changes in the compressibility modulus values is observed the mixed DSPC/oxysterol monolayers, indicating the oxysterols reduced ability to intercalate into the solid DSPC monolayer.

In the mixed monolayer with DAPC/sterol, at  $X_{\text{sterol}} = 0.1$ , no significant change in the compressibility modulus values was observed for the mixed DAPC/Chol monolayer compared to pure DAPC (Fig. 5.15A); however, in mixtures with oxysterols the compressibility modulus decreased relative to that of pure (Fig. 5.15B,C). Additionally, in the mixed DAPC/5,6 $\beta$ -EChol monolayer for  $X_{5,6\beta\text{-EChol}} = 0.1$ , an inflection point at 15 mN/m is observed. This result suggests that after 5,6 $\beta$ -EChol disordered the DAPC monolayer, as the surface pressure increased it demonstrates the ability to order the

monolayer. Analysis at  $X_{\text{sterol}} = 0.3$ , reveals a zero compressibility modulus value for the mixed DAPC at 15 mN/m and 5,6 $\beta$ -EChol at 18 mN/m (Fig. 5.15B,C). Zero compressibility modulus values are an indication that a first order main phase transition has taken place. This result indicates major disruption of DAPC in the presence of the oxysterols. At  $X_{\text{sterol}} = 0.5$ , in both mixed DAPC/7-KChol and DAPC/5,6 $\beta$ -EChol monolayers, the zero compressibility modulus is still observed but at the surface pressures of 10 and 15 mN/m, respectively (Fig. 5.10B,C). At  $X_{\text{sterol}} = 0.7$ , no inflection point in the mixed DAPC/Chol is observed, while, a minimum compressibility modulus value still persists with the mixed oxysterols monolayers.

The compressibility modulus values as a function of sterol concentration at  $X_{\text{sterol}} \leq 0.3$  shows a reduction in value relative to pure DAPC, in particular at surface pressures at 3 and 10 mN/m demonstrating that all three sterols disorder the gel phase of DAPC (Fig. 5.15D–F) In the range  $0.3 \leq X_{\text{sterol}} \leq 0.7$  there is a linear increase in the compressibility modulus values that exceed that of the pure oxysterol when  $X_{\text{sterol}} = 0.7$  at high surface pressures. It was also noted that at 30 and 40 mN/m the disordering effect observed at low surface pressures is reduced, particularly in the PC monolayers mixed with Chol. The results clearly show here that oxysterols have a greater capability to disorder DAPC.

Looking back on the mixed DSPC/sterol compressibility modulus results, Chol demonstrated the greatest ability in disrupting the solid phase of DSPC. This result is in stark contrast to what was observed in the DAPC/sterol monolayers. One possible explanation for this difference the additional oxygen moiety on the sterol rings of the

oxysterols have a larger projected mean molecular area and can thus disrupt the solid phase of DAPC and act as more effective spacer molecule than Chol.<sup>145</sup> A quick look at the excess molecular area also shows that Chol is more miscible in DAPC than the oxysterols (Fig. 5.15D–F). Another probable mechanism, in conjunction with the excess area of the oxysterols, is the reduced miscibility of the oxysterols behind the major disruption of the solid phase DAPC. In the monolayer, this reduced miscibility can lead to minor phase separation between the two components. Because of this minor phase separation, the DAPC lipids that are in close proximity to the oxysterols are disrupted by a greater extent hence the fluidization of DAPC. Of the sterols, 7-KChol demonstrates the greatest ability in disrupting DAPC. Again as previously mentioned, 7-KChol is tilted closer to the interface than the other sterols. Also, this tilting results in the ketone group being a closer proximity to the headgroup of DAPC. As a result, 7-KChol can descend into the headgroup region more efficiently disrupting the long-range order between the pure DAPC. At high sterol concentrations, the compressibility modulus values of the mixed monolayers were higher than for their pure counterparts (Fig. 5.15D–F). This may be because the sterols are not symmetrically distributed throughout the monolayer and hence have a greater ability to order DAPC.

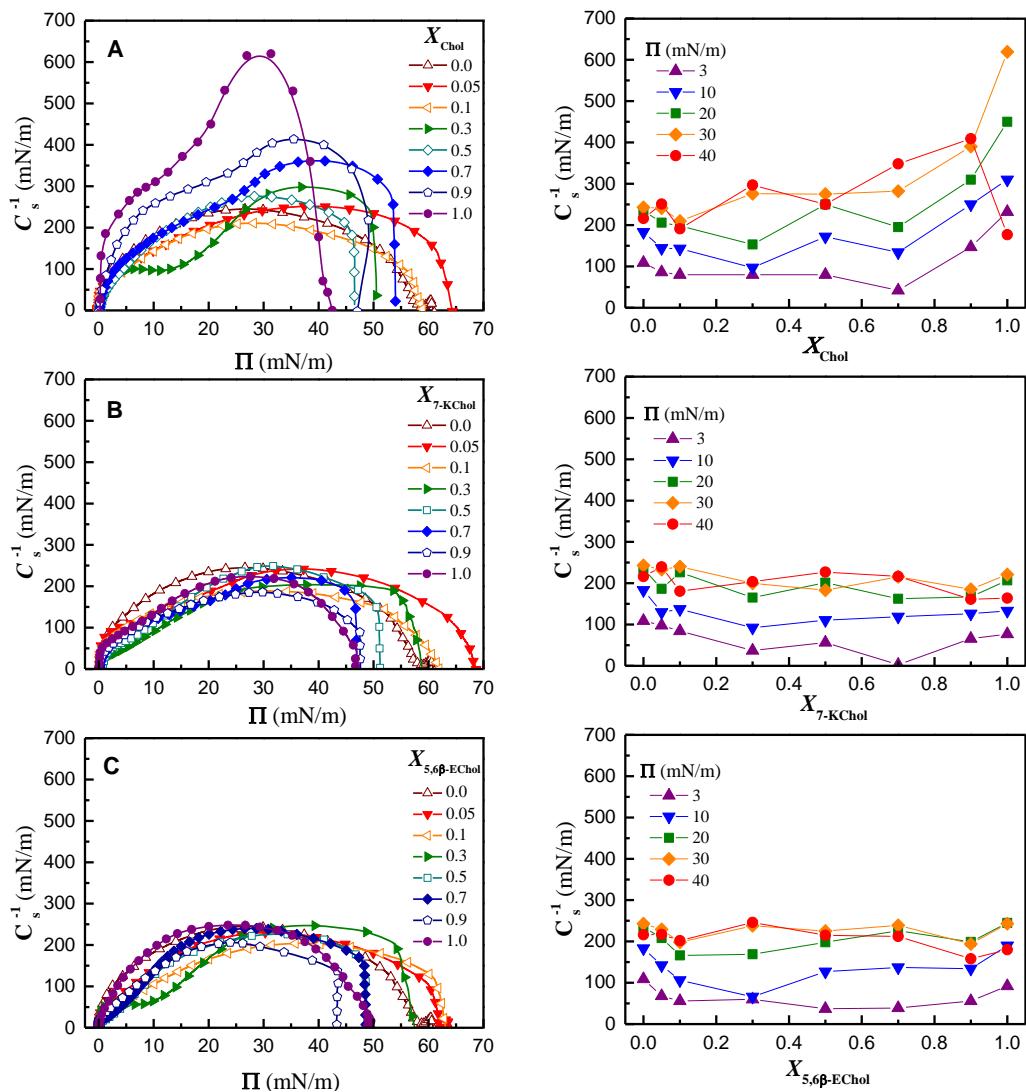


Figure 5.14 Variations of monolayer compressibility modulus with (A–C) surface pressure and (D–F) sterol composition for (A and D) Chol, (B and E) 7-KChol, and (C and F) 5,6β-EChol mixed with DSPC monolayers. The compressibility data was calculated from the compression isotherms shown in Fig. 5.11.

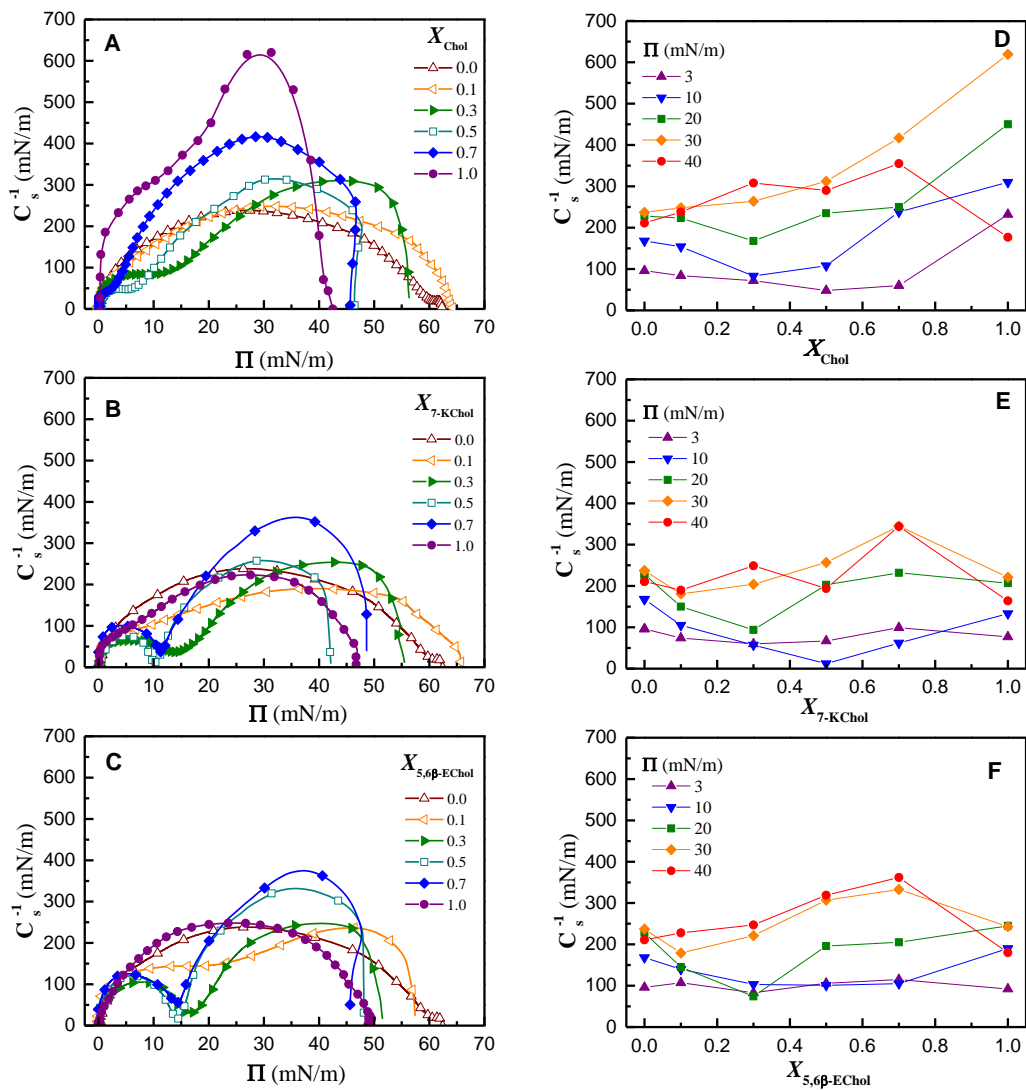


Figure 5.15 Variations of monolayer compressibility modulus with (A–C) surface pressure and (D–F) sterol composition for (A and D) Chol, (B and E) 7-KChol, and (C and F) 5,6 $\beta$ -EChol mixed with DAPC monolayers. The compressibility data was calculated from the compression isotherms shown in Fig. 5.11.

### 5.3.3 Excess Free Energy of Mixing of DSPC, DAPC, Sterols, and their Mixtures

Analysis of the excess free energy in the mixed DSPC/sterol monolayers at 40 mN/m and at  $X_{\text{sterol}} = 0.3$  reveals the most and least negative  $\Delta G_{\text{exc}}$  values for the mixed DSPC/Chol and DSPC/7-KChol monolayers, respectively (Fig. 5.16A,B). Positive excess free energy values are obtained in the mixed DSPC/7-KChol monolayer at  $X_{\text{sterol}} = 0.9$ . With regards to the DAPC at 40 mN/m the excess free energy follows the trend 7-KChol > 5,6 $\beta$ -EChol > Chol (Fig. 5.16D–F), which is the same as in the mixed DSPC/sterol monolayer. Both PCs demonstrate that their preferred PC:sterol stoichiometry is 2:1.

From our study, we find a clear PC and sterol dependency trend on condensing and ordering abilities. Regarding condensing effects, it was quite apparent that relative fluidity of PC monolayers, hydrophobic mismatch and sterol type influenced the observed magnitude between PC and sterols. Ordering effects, however, were clearly affected by the additional oxygen moiety in oxysterols, as they were ineffective in comparison to Chol in each of the PCs studied. This parameter was clearly affected by the additional volume imposed by the oxygen atom. Also, in fluid DLPC and DMPC monolayers, phase separation was only observed when mixed with Chol. And, the formation of stable complexes of PC:sterol was dependent on hydrophobic mismatch and monolayer composition in which it occurred. Turning to the condensed monolayers of DSPC and DAPC, Chol is commonly referred to as a spacer molecule as it intercalates into solid monolayers disrupting long-range order thereby fluidizing the monolayer. This effect was observed in both DSPC and DAPC monolayers with addition of small amounts of Chol. However, with DSPC, it was revealed that oxysterols could not fluidize the

monolayer as well as Chol. It came as a surprise, however, that with DAPC, oxysterols demonstrated greater fluidizing abilities. In depth analysis of the isothermal revealed that immiscibility effects, and added bulkiness and roughness of these oxysterol played a substantial role in the drastic fluidization observed.

These changes in the interfacial behavior of PCs with sterols can have significant implications for the lateral organization of cellular membranes, especially lipid raft formation and the breathing process. Condensed monolayer films on the surface of marine aerosols to affect to evaporation and gas diffusion. As oxysterols were shown to affect lipid order, there could be repercussion on the reactivity of marine aerosols in the atmosphere.

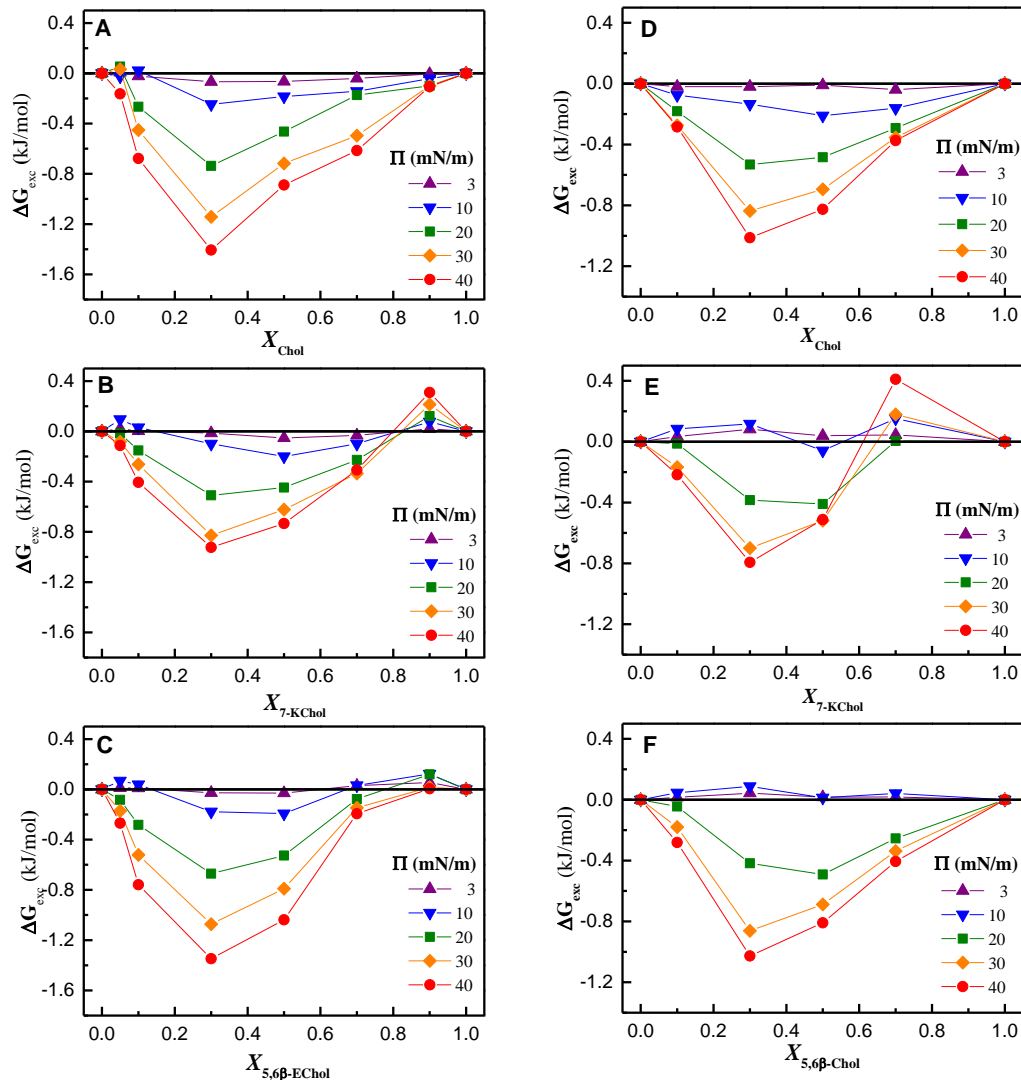


Figure 5.16 Variations of excess free energy of mixing of sterol composition for (A) Chol, (B) 7-KChol, and (C) 5,6 $\beta$ -EChol in binary mixtures with DSPC. Variations of excess free energy of mixing of sterol composition for (D) Chol, (E) 7-KChol, and (F) 5,6 $\beta$ -EChol in binary mixtures with DAPC.

## 5.4 Conclusions

From previous studies, it is known that Chol demonstrates the dual ability of ordering fluid PC monolayers while disordering solid PC monolayers. With our study, we also find a clear PC and sterol dependency trend on condensing and ordering abilities. Regarding condensing effects, it was quite apparent that relative fluidity of PC monolayers, hydrophobic mismatch and sterol type influenced the observed magnitude between PC and sterols. Ordering effects, however, were clearly affected by the additional oxygen moiety in oxysterols, as they were ineffective in comparison to Chol in each of the PCs studied. This parameter was clearly affected by the additional volume imposed by the oxygen atom. Also, in fluid DLPC and DMPC monolayers, phase separation was only observed when mixed with Chol. And, the formation of stable complexes of PC:sterol was dependent on hydrophobic mismatch and monolayer composition in which it occurred. Turning to the condensed monolayers of DSPC and DAPC, Chol is commonly referred to as a spacer molecule as it intercalates into solid monolayers disrupting long-range order thereby fluidizing the monolayer. This effect was observed in both DSPC and DAPC monolayers with addition of small amounts of Chol. However, with DSPC, it was revealed that oxysterols could not fluidize the monolayer as well as Chol. It came as a surprise, however, that with DAPC, oxysterols demonstrated greater fluidizing abilities. In depth analysis of the isothermal revealed that immiscibility effects, and added bulkiness and roughness of these oxysterol played a substantial role in the drastic fluidization observed.

These changes in the interfacial behavior of PCs with sterols can have significant implications for the lateral organization of cellular membranes, especially lipid raft formation and the breathing process. Condensed monolayer films on the surface of marine aerosols to affect to evaporation and gas diffusion. As oxysterols were shown to affect lipid order, there could be repercussion on the reactivity of marine aerosols in the atmosphere.

## 6. Chapter : High-Resolution Broad-Bandwidth VSFG spectroscopy of Pure Cholesterol, 7-Ketocholesterol and 5 $\beta$ ,6 $\beta$ -Epoxycholesterol Monolayers at the Air/Water Interface

VSFG spectroscopy has proven quite ideal for probing the interfacial organization (ordering, orientation) of lipid monolayers at the air/water interface as well as in other model membrane systems.<sup>17, 110, 152, 153 154</sup> The VSFG spectrum of Chol has been previously reported for both liquid and solid interfaces,<sup>155 110, 156</sup> and spectral assignment has been given, even though it remains tentative and incomplete.<sup>155</sup> In addition, VSFG spectroscopy has also provided information about the condensing effect of Chol and palmitic acid when mixed with a DPPC monolayer by determining their impact on the ordering of the phospholipid acyl chain.<sup>17, 152</sup> However, to date, there has been no VSFG study of oxysterol monolayers, with the exception of the work by Ma et al. who attempted to make peak assignments for 6-ketocholesterol.<sup>157</sup>

The main structural parts of Chol that influence sterol-lipid interactions are the planar tetracyclic rings, the 3 $\beta$ -hydroxyl group and the isooctyl chain that is attached at C17 (Fig. 1.3A). As mentioned in the preceding chapters and also in previous studies, modifications to the molecular structure of Chol affects sterol-lipid interactions in bilayers that can influence proper membrane function, for example in the formation of lipid rafts. In an atomistic simulation study by Aittoniemi et. al. the tilt

angle of the molecular plane formed by the steroid nucleus of Chol and three of its analogues was investigated in mixed bilayers of DPPC.<sup>133</sup> From their study, they observed that the smaller the tilt angle of the sterols from the surface normal, the stronger their ordering abilities when mixed in bilayers with DPPC. The numerical tilt angle given for Chol with a concentration of 20% in the mixed bilayer with DPPC was  $\sim 20^\circ$ . This value also correlates with other studies that have calculated the tilt angle of Chol mixed in biological relevant lipids that range between  $10\text{--}30^\circ$ .<sup>149, 158, 159, 160</sup> More recently, Kett et. al. determined the tilt angle of pure Chol in hybrid bilayers using VSFG spectroscopy and obtained a tilt angle value of  $\leq 25^\circ$ .<sup>161</sup> With regards to the oxysterols used in our study, no simulation or VSFG study have been performed to determine the tilt angles of 7-KChol and 5,6 $\beta$ -EChol in monolayers or bilayers. However, Ma et. al. determined the tilt angle of the ketone group on 6-ketocholestanol, an analogue of 7-KChol, to be  $\sim 10^\circ$ . However, more studies are needed to determine the tilt angles of oxysterols to understand their impact on the ordering of lipids in biomembranes.<sup>157</sup>

In this chapter we used HR-BB-VSFG spectroscopy to study the interfacial organization of pure Chol, 7-KChol and 5,6 $\beta$ -EChol monolayers at the air/water interface. The spectral assignment focuses on the C–H vibrational stretching region ( $2750\text{--}3100\text{ cm}^{-1}$ ). We also used these HR-BB-VSFG spectra to determine the sterol tilt angles from the surface normal.

## 6.1 Materials

7-ketocholesterol (7-KChol, >99%), and 5 $\beta$ ,6 $\beta$ -epoxycholesterol (5,6 $\beta$ -EChol, >99%) were purchased from Avanti Polar Lipids (Alabaster, AL), whereas cholesterol (Chol, >99%) was from Sigma-Aldrich (St. Louis, MO). All compounds were used without further purification. 1 mM sterol stock solutions were prepared in chloroform (HPLC grade,  $\geq$ 99.0%, Fisher Scientific, Pittsburgh, PA).

## 6.2 Results and Discussion

### 6.2.1 VSFG Spectra of Pure Sterol Monolayers

The VSFG spectra of pure Chol, 5,6 $\beta$ -EChol and 7-KChol monolayers in the CH stretching region (2750–3100 cm<sup>-1</sup>) are presented in Figs. 6.1, 6.2 and 6.3, respectively, for both *ssp* and *ppp* polarization combinations. A comparison of all three spectra is also shown in Fig 6.4. These polarization modes are more sensitive to the vibrational modes that are perpendicular and parallel, respectively, to the plane of incidence. For example, the asymmetric vibrational modes is known to be parallel to the plane of incidence and therefore can be unambiguously assigned with the *ppp* polarization. The CH stretching region encompasses the C–H vibrational modes (e.g., symmetric and asymmetric stretching, Fermi resonance (FR), and combination bands) from the CH, CH<sub>2</sub> and CH<sub>3</sub> groups. A list of possible assignments for some of the peaks is provided in Table 6.1 according to previously published data.<sup>154, 155, 156, 157</sup>

In terms of obtaining accurate peak assignments for the sterols, it is quite difficult as these are complex molecules and as such there are some uncertainties in the interpretation of their VSG spectra. The reason for this uncertainty is the result of the CH, CH<sub>2</sub> and CH<sub>3</sub> groups being directly connected to different structures on the sterol.

In the spectrum of Chol, two prominent peaks are observed at 2945.1 and 2962.4 cm<sup>-1</sup> (Fig. 6.1). The first peak is a convolution of CH<sub>2</sub><sub>as</sub> and CH<sub>3</sub><sub>FR</sub> vibrational modes, whereas the second peak has been assigned to the CH<sub>3</sub><sub>as</sub> mode of CH<sub>3</sub> groups on the sterol ring. Two other minor peaks at 2850.1 and 2874.1 cm<sup>-1</sup> have been assigned to the CH<sub>2</sub><sub>ss</sub> and CH<sub>3</sub><sub>ss</sub> vibrational modes, respectively;<sup>155, 156</sup> the last mode belongs to the CH<sub>3</sub> groups of the isooctyl chain. Another CH<sub>3</sub><sub>ss</sub> mode, this one related to the sterol ring, gives rise to a weak shoulder at 2861.1 cm<sup>-1</sup>.<sup>110, 155</sup> The weak shoulder at 2885 cm<sup>-1</sup> has been assigned to the CH<sub>2</sub><sub>FR</sub> vibrational mode, whereas the minor peak at 2906 cm<sup>-1</sup> was tentatively assigned to the R<sub>3</sub>C-H.<sup>155</sup> Finally, the feature observed at 2822.1 cm<sup>-1</sup> is probably not a peak but may be the result of an interference coming from two adjacent peaks with opposite phase.

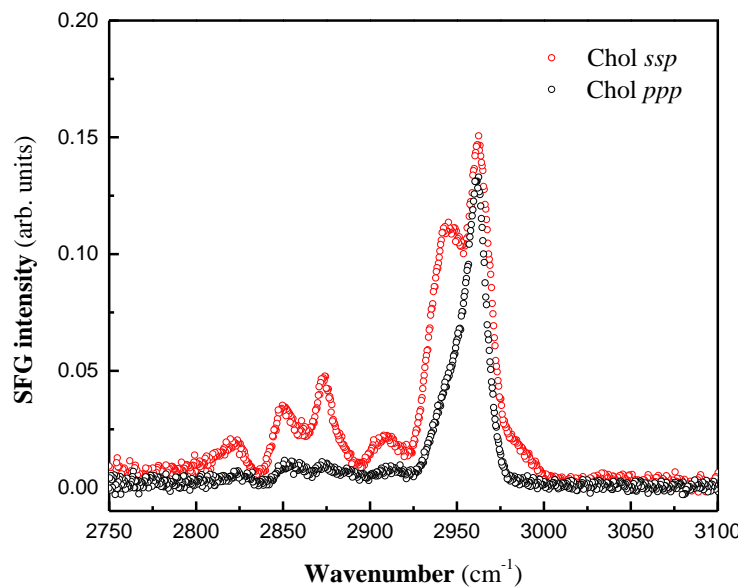


Figure 6.1 VSGF spectra of pure Chol monolayers at the air/water interface.

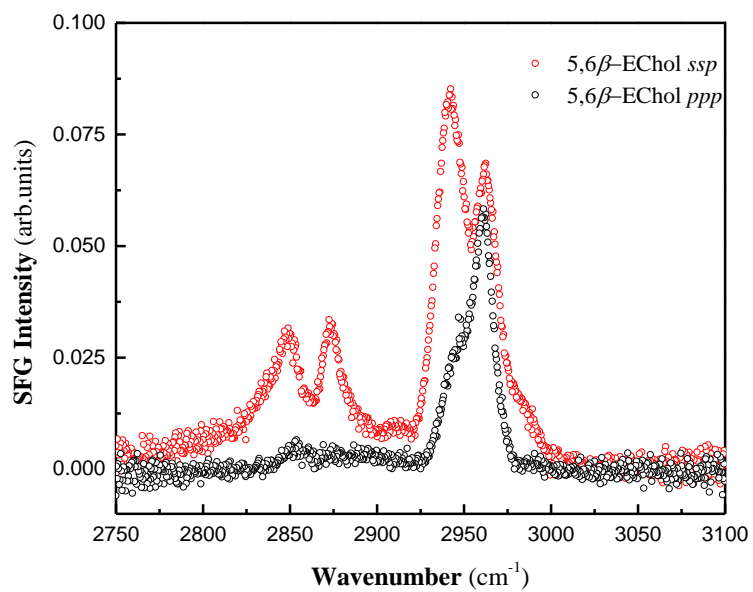


Figure 6.2 VSGF spectra of pure 5,6 $\beta$ -EChol monolayers at the air/water interface.

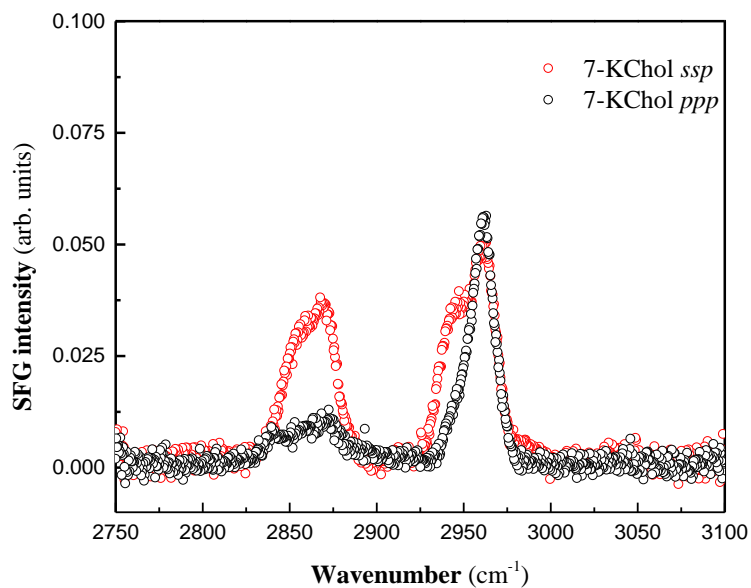


Figure 6.3 VSGF spectra of pure 7-KChol monolayers at the air/water interface.

Table 6.1 Peak frequencies and spectral assignment of VSGF spectra of Chol, 7-KChol, and 5,6 $\beta$ -EChol monolayers at the air/water interface.<sup>154, 156, 157</sup>

Frequency/cm <sup>-1</sup>	Assignment
2822.1	interference
2837.2	no assignment
2850.1	CH <sub>2</sub> <sub>ss</sub>
2861.1	CH <sub>3</sub> <sub>ss</sub> (sterol rings)
2874.4	CH <sub>3</sub> <sub>ss</sub> (on the isooctyl tail)
2885.3	CH <sub>2</sub> FR
2906.3	R <sub>3</sub> C-H
2945.1	CH <sub>3</sub> <sub>ss</sub> FR and CH <sub>2</sub> <sub>as</sub>
2962.4	CH <sub>3</sub> <sub>as</sub> (sterol rings)
2971.3	no assignment
2991.7	no assignment

By looking at the 5,6 $\beta$ -EChol spectrum, many similarities can be found to the Chol spectra; however, it is apparent that the spectral feature at 2822.1 cm<sup>-1</sup> is no longer present. Also, at 2837 cm<sup>-1</sup>, the dip seen in the Chol spectrum has been replaced by a shoulder in the 5,6 $\beta$ -EChol spectrum. While no assignment has been made, the appearance of the peak seems to suggest a difference in the orientation between the two sterols. The two prominent peaks at 2945.1 and 2962.4 cm<sup>-1</sup> were still observed, however, their relative intensity ratio is opposite to that observed for Chol. One assumption that can be made is that the CH<sub>3</sub> FR band may be changing in intensity. The CH<sub>2</sub> ss vibrational mode at 2950.1 cm<sup>-1</sup> is still observed with approximately the same peak intensity of Chol, while the peak intensity at 2874.1 cm<sup>-1</sup> is slightly less than Chol. This may be due to differences in the orientation of the isooctyl chains or to a lesser surface number density of probed sterol molecules resulting from the added molecular area caused by the epoxy group. The intensity of the peak at 2906.3 cm<sup>-1</sup> is also less than Chol.

In the spectrum of 7-KChol, the feature at 2822.1 cm<sup>-1</sup> is also absent (Fig. 6.3). The shoulder that was observed at 2937.2 cm<sup>-1</sup> in 5,6 $\beta$ -EChol is not observed in the 7-KChol spectrum, again suggesting differences in orientation. The two distinct peaks observed in Chol and 5,6 $\beta$ -EChol at 2850.1 and 2874.1 cm<sup>-1</sup> are replaced by a broad peak in the 7-KChol spectrum (Fig. 6.3). However, while the peak at 2861.1 cm<sup>-1</sup> appeared as a shoulder in both Chol and 5,6 $\beta$ -EChol, this peak is prominent in 7-KChol. Also, the peaks at 2906.3, 2945.1 and 2962.4 cm<sup>-1</sup> that are present in Chol are observed in the 7-KChol spectrum but with a lower intensity. Again, it is important to remember that these are indeed tentative assignments and are therefore susceptible to error.

### 6.2.2 Orientation of Sterols

The orientation angle of the sterol ring methyl groups ( $\theta_{\text{CH}_3}$ ) from the surface normal can be determined from the VSFG spectra for all three sterols with the *ssp* polarization mode. The methyl group tilt angle of the sterols is defined as the angle between the surface normal and the vector T joining C3 and C17 (Fig 6.4).<sup>161</sup> This angle can also be used to further determine the tilt of molecular plane formed by the steroid nucleus ( $\theta_T$ ) with respect to the surface normal. Because the methyl groups at C18 and C19 are almost perpendicular to the ring system of Chol, therefore the sterol plane tilt angle is approximately given by  $\theta_{\text{CH}_3} = (90 + \theta_T)^\circ$ .

The calculation method used to determine the orientation of the molecules from the surface normal has been documented elsewhere.<sup>107, 162</sup> A brief summary of the orientation angle calculation revolves around the VSFG second-order nonlinear susceptibility ( $\chi$ ) and the mean  $\text{CH}_3$  orientation angle ( $\theta_{\text{CH}_3}$ ). The orientation angle of the sterol  $\text{CH}_3$  group from the surface normal is calculated by

$$\frac{I_{ss}}{I_{as}} = \frac{\chi_{yyz}^{(2)}(\nu_{ss}\text{CH}_3)}{\chi_{yyz}^{(2)}(\nu_{as}\text{CH}_3)} \propto \left| \frac{(1+r)\cos\theta_{\text{CH}_3} - (1-r)\cos^3\theta_{\text{CH}_3}}{\cos\theta_{\text{CH}_3} - \cos^3\theta_{\text{CH}_3}} \right| \quad (r = 2.3) \quad (1)$$

The peak intensity ratio  $I_{ss}/I_{as}$  between  $\nu(\text{CH}_{3ss})$  at  $2861.1 \text{ cm}^{-1}$  and  $\nu(\text{CH}_{3as})$  at  $2962.4 \text{ cm}^{-1}$  has a direct relationship with  $\theta_{\text{CH}_3}$  (values of  $r = 2.3$ ). Therefore,  $\theta_{\text{CH}_3}$  can be easily obtained by knowing the  $\chi_{yyz}(\text{CH}_{3ss})/\chi_{yyz}(\text{CH}_{3as})$  ratio. This ratio is obtained from the

square root of the  $I_{ss}/I_{as}$  ratio and was used in trying to identify the tilt angle of the sterols. (Table 6.2).<sup>152</sup>

Using the value of  $r = 2.3$  given in Ma et. al. it was not possible to determine quantitatively the tilt angle for the sterols.<sup>152</sup> Experimental (Raman depolarization ratio measurements) and theoretical (bond polarizability analysis) studies have shown that the  $r$  values of  $\text{CH}_3$  groups from simple molecules such as methanol, ethanol and dimethylsulfoxide typically fall in the range 1.7–4.0.<sup>163</sup> In the paper of Ma et al., the  $r$  value corresponds to the terminal methyl group of DPPC. However, this value may not be representative of the methyl groups attached to the steroid nucleus. Further experimental work is therefore needed to determine the  $r$  value for sterols which is beyond the scope of this dissertation. However, while we do not know this value, a qualitative conclusion can still be made. From the intensity ratios shown in Table 6.2, 7-KChol appears to be the most tilted from the surface normal and Chol the least (Figs 6.5 and 6.6).

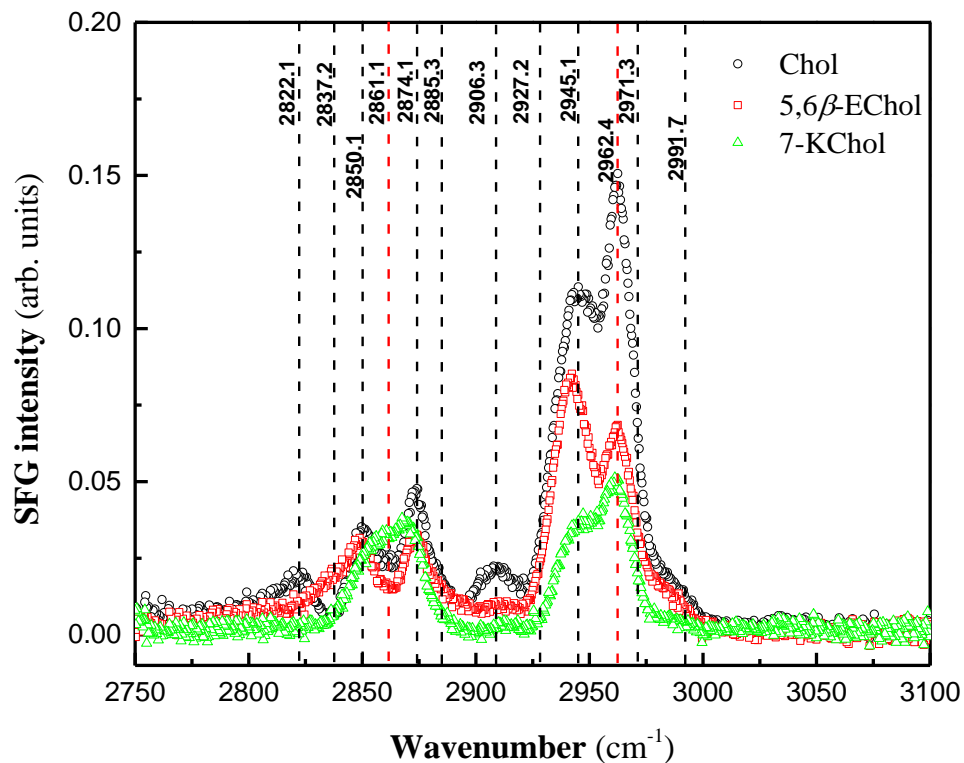


Figure 6.4 Comparison of the *ssp* VSG spectra of pure Chol, 7-KChol, and 5,6 $\beta$ -EChol at the air/water interface.

Table 6.2 Sterol CH<sub>3</sub> groups and sterol molecule tilt angles. Parentheses indicate extrapolated values

Sterol	$ \chi_{ssp,ss}/\chi_{ssp,as} $
Chol	0.409
7-KChol	0.785
5,6 $\beta$ -EChol	0.488

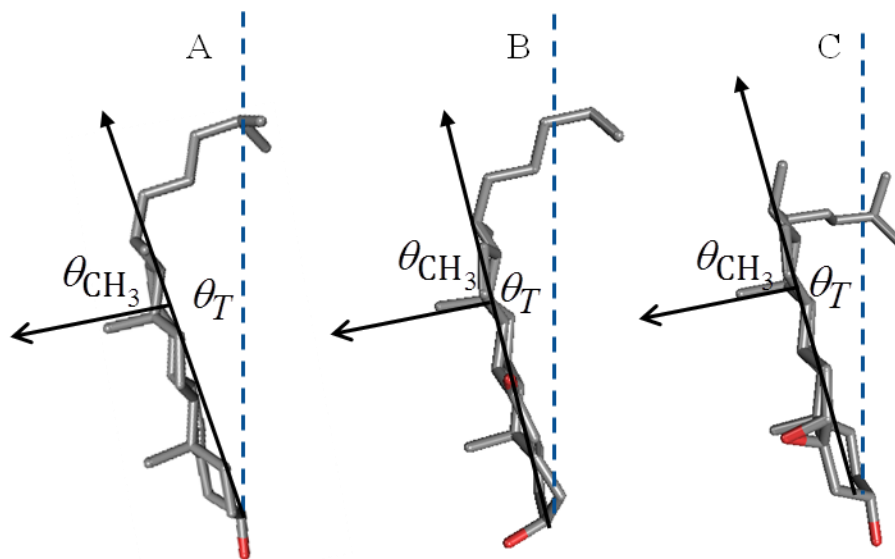


Figure 6.5 The methyl group tilt angle of sterol ( $\theta_{\text{CH}_3}$ ) is defined as the angle between the surface normal and the vector **T** joining C3 to C17 for (A) Chol, (B) 7-KChol, and (C) 5,6 $\beta$ -EChol.

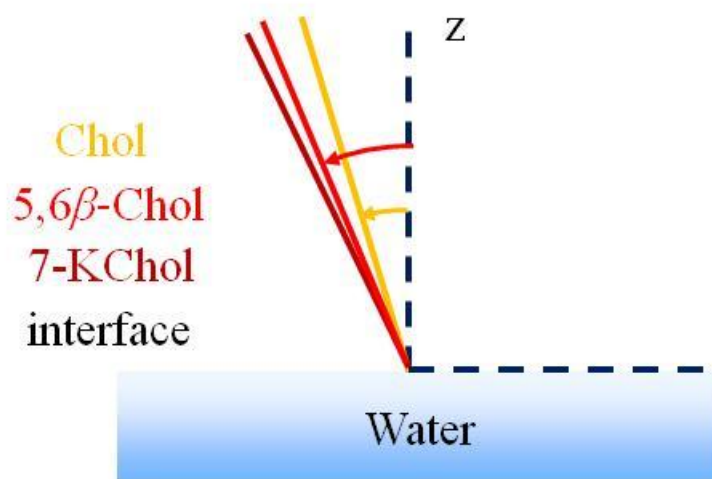


Figure 6.6 The tilt angle of the molecular plane formed by the steroid nucleus relative to the surface normal.

## 7. Chapter : Conclusions and Implications

The work presented in this thesis is motivated by an interest in understanding the influence of oxysterols on the molecular-level interactions between PCs that are relevant to biomembranes, PS, and marine aerosols, and to compare these interactions with those of Chol. Chol has been extensively studied in many model membranes systems, particularly in binary mixed PC monolayers. Reasons for this interest include Chol's fluidizing and permeability capabilities in monolayers and bilayers as well as its ability to phase separate into Chol-rich and Chol-poor microdomains. With regards to these model membrane studies, researchers have focused on varying the acyl chain asymmetry, length, and degree of saturation, as well as the type of headgroup. More recently, there has been an increased interest in understanding molecular-level interactions in model membrane systems in binary mixtures of phospholipids and oxysterols. These studies have placed an emphasis on investigating these interactions with one or two different phospholipids with the variant being oxysterols. To the author's knowledge, no systematic study has been done to vary both phospholipids and sterols over a wide range of monolayer compositions to extract a more comprehensive analysis of these interactions. With this study, we were able to deduce that the oxysterols do differ in their interactions with PCs in comparison to Chol.

The condensing ability was dependent on the sterol type, acyl chain length, composition and physical state of the monolayer. From the compressibility modulus values, oxysterols were inferior to Chol in ordering the acyl tails of all the PCs used in this study. The Gibbs free energy analysis indicated differences in the preferred PC:sterol stoichiometry and thermodynamic stability. For instance, at the 2:1 stoichiometry in DLPC, Chol demonstrated the lowest favorable interaction among all sterols, however as the acyl chain length increased, this stoichiometry became increasingly favorable. For 7-KChol in DLPC, the 2:1 stoichiometry was highly preferred showing greater thermodynamic stability in comparison to Chol however, its thermodynamic stability became least favored in DSPC and DAPC compared to the other sterols. For 5,6 $\beta$ -EChol, the 2:1 stoichiometry was less favorable in the fluid DMPC but as the chain length increased it exhibited intermediate thermodynamic stability between the sterols. In this study, it appears that the thermodynamic stability is dependent on the hydrophobic length and the oxygen moiety. Also, in terms of phase separation, both oxysterols are inferior to Chol.

From a biological standpoint, the most striking observation from this study was that the oxysterols, at times, demonstrated equivalent thermodynamic stability to that of Chol. However, they were incapable of ordering the acyl chains as efficiently as Chol. One can see that in biomembranes these oxysterols can compete with Chol in interacting with other lipids components but cannot perform the roles as efficiently as Chol. This can therefore affect proper membrane function. Also, in the more solid lipid, DAPC, the oxysterols disrupted these monolayers more efficiently than Chol. For biomembranes,

this disruption may have implications for interfering with highly ordered structure, for instance lipid rafts.

With reference to the data presented in Chapter 4, this section was highly important in regards to lung function as DPPC is by far the most prevalent lipid constituent in PS. Both oxysterols demonstrated poorer fluidic regulating capabilities in comparison to Chol and can therefore influence lung function.

Turning to marine aerosols, as previously mentioned, their sizes are directly correlated to their environmental effects. Because the oxysterols mixed with the PCs demonstrated reduces ordering abilities, one can infer that an aerosol with an increased concentration of oxysterols in the surface will be more permeable. This can result in an increased evaporation of the aqueous core, and as a result concentration of the inorganic material.

## REFERENCES

1. Li, X. M.; Momsen, M. M.; Brockman, H. L.; Brown, R. E. Sterol structure and sphingomyelin acyl chain length modulate lateral packing elasticity and detergent solubility in model membranes. *Biophys. J.* **2003**, *85* (6), 3788-3801.
2. Marsh, D. Lateral pressure in membranes. *Biochim. Biophys. Acta-Reviews on Biomembranes* **1996**, *1286* (3), 183-223.
3. Kozarac, Z.; Mobius, D.; Spohn, D. B. Investigation of sea-surface microlayer and phytoplankton culture samples by monolayer techniques and Brewster angle microscopy. *Croatica Chem. Acta* **1998**, *71* (2), 285-301.
4. Weeraman, C.; Chen, M.; Moffatt, D. J.; Lausten, R.; Stolow, A.; Johnston, L. J. A combined vibrational sum frequency generation spectroscopy and atomic force microscopy study of sphingomyelin-cholesterol monolayers. *Langmuir* **2012**, *28* (36), 12999-13007.
5. Horton R. H.; Moran L. A.; Scrimgeour K. G.; Perry M. D.; Rawn J. D. *Principles of Biochemistry*; 4th ed.; Pearson Prentice Hall: New Jersey, 2006.
6. Ohvo-Rekilä, H.; Ramstedt, B.; Leppimäki, P.; Slotte, J. P. Cholesterol interactions with phospholipids in membranes. *Prog. Lipid Res.* **2002**, *41* (1), 66-97.
7. Kaganer, V. M.; Mohwald, H.; Dutta, P. Structure and phase transitions in Langmuir monolayers. *Rev. Mod. Phys.* **1999**, *71* (3), 779-819.
8. Bloch, K. E. Sterol structure and membrane function. *CRC Crit. Rev. Biochem.* **1983**, *14* (1), 47-92.
9. Worthman, L. A. D.; Nag, K.; Davis, P. J.; Keough, K. M. W. Cholesterol in condensed and fluid phosphatidylcholine monolayers studied by epifluorescence microscopy. *Biophys. J.* **1997**, *72* (6), 2569-2580.
10. Yeagle, P. L. Cholesterol and the cell membrane. *Biochim. Biophys. Acta* **1985**, *822* (3-4), 267-287.
11. Bach, D.; Epan, R. F.; Epan, R. M.; Miller, I. R.; Wachtel, E. The oxidized form of cholesterol 3 $\beta$ -hydroxy-5-oxo-5,6-secocholestan-6-al induces structural and thermotropic changes in phospholipid membranes. *Chem. Phys. Lipids* **2009**, *161* (2), 95-102.
12. Mulder, M. Sterols in the central nervous system. *Curr. Opin. Clin. Nutr. Metab. Care* **2009**, *12* (2), 152-158.
13. Donaldson, J. G.; Porat-Shliom, N.; Cohen, L. A. Clathrin-independent endocytosis: A unique platform for cell signaling and PM remodeling. *Cell. Signalling* **2009**, *21* (1), 1-6.

14. Ziblat, R.; Leiserowitz, L.; Addadi, L. Crystalline domain structure and cholesterol crystal nucleation in single hydrated DPPC:cholesterol:POPC bilayers. *J. Am. Chem. Soc.* **2010**, *132* (28), 9920-9927.
15. Preston Mason, R.; Tulenko, T. N.; Jacob, R. F. Direct evidence for cholesterol crystalline domains in biological membranes: role in human pathobiology. *Biochim. Biophys. Acta* **2003**, *1610* (2), 198-207.
16. Yu, S. H.; Possmayer, F. Dipalmitoylphosphatidylcholine and cholesterol in monolayers spread from adsorbed films of pulmonary surfactant. *J. Lipid Res.* **2001**, *42* (9), 1421-1429.
17. Bonn, M.; Roke, S.; Berg, O.; Juurlink, L. B. F.; Stamouli, A.; Muller, M. A molecular view of cholesterol-induced condensation in a lipid monolayer. *J. Phys. Chem. B* **2004**, *108* (50), 19083-19085.
18. Stockton, G. W.; Smith, I. C. P. Deuterium nuclear magnetic resonance study of condensing effect of cholesterol on egg phosphatidylcholine bilayer membranes. 1. Perdeuterated fatty acid probes. *Chem. Phys. Lipids* **1976**, *17* (2-3), 251-263.
19. Kulig, W.; Tynkkynen, J.; Javanainen, M.; Manna, M.; Rog, T.; Vattulainen, I.; Jungwirth, P. How well does cholesteryl hemisuccinate mimic cholesterol in saturated phospholipid bilayers? *J. Mol. Model.* **2014**, *20* (2), 1-9.
20. Notter, R. H. *Lung Surfactants: Basic Science and Clinical Applications*; New York City, 2000; Vol. 149.
21. Massey, J. B.; Pownall, H. J. Structures of biologically active oxysterols determine their differential effects on phospholipid membranes. *Biochemistry* **2006**, *45* (35), 10747-10758.
22. Mintzer, E.; Charles, G.; Gordon, S. Interaction of two oxysterols, 7-ketocholesterol and 25-hydroxycholesterol, with phosphatidylcholine and sphingomyelin in model membranes. *Chem. Phys. Lipids* **2010**, *163* (6), 586-593.
23. Björkhem, I.; Diczfalusy, U. Oxysterols - Friends, foes, or just fellow passengers? *Arterioscler. Thromb. Vasc. Biol.* **2002**, *22* (5), 734-742.
24. Olkkonen, V. M.; Hynynen, R. Interactions of oxysterols with membranes and proteins. *Mol. Aspects Med.* **2009**, *30* (3), 123-133.
25. Rooney, M.; Tamuralis, W.; Lis, L. J.; Yachnin, S.; Kucuk, O.; Kauffman, J. W. The influence of oxygenated sterol compounds on dipalmitoylphosphatidylcholine bilayer structure and packing. *Chem. Phys. Lipids* **1986**, *41* (1), 81-92.
26. Theunissen, J. J. H.; Jackson, R. L.; Kempen, H. J. M.; Demel, R. A. Membrane properties of oxysterols interfacial orientation, influence on membrane permeability and redistribution between membranes. *Biochim. Biophys. Acta* **1986**, *860* (1), 66-74.
27. Wang, J. W.; Megha; London, E. Relationship between sterol/steroid structure and participation in ordered lipid domains (lipid rafts): Implications for lipid raft structure and function. *Biochemistry* **2004**, *43* (4), 1010-1018.
28. Massey, J. B.; Pownall, H. J. The polar nature of 7-ketocholesterol determines its location within membrane domains and the kinetics of membrane micro solubilization by apolipoprotein A-I. *Biochemistry* **2005**, *44* (30), 10423-10433.

29. Vejux, A.; Lizard, G. Cytotoxic effects of oxysterols associated with human diseases: Induction of cell death (apoptosis and/or oncosis), oxidative and inflammatory activities, and phospholipidosis. *Mol. Aspects Med.* **2009**, *30* (3), 153-170.
30. Murphy, R. C.; Johnson, K. M. Cholesterol, reactive oxygen species, and the formation of biologically active mediators. *J. Biol. Chem.* **2008**, *283* (23), 15521-15525.
31. Maor, I.; Kaplan, M.; Hayek, T.; Vaya, J.; Hoffman, A.; Aviram, M. Oxidized monocyte-derived macrophages in aortic atherosclerotic lesion from apolipoprotein E-deficient mice and from human carotid artery contain lipid peroxides and oxysterols. *Biochem. Biophys. Res. Comm.* **2000**, *269* (3), 775-780.
32. Bach, D.; Epand, R. F.; Epand, R. M.; Wachtel, E. Interaction of 7-ketocholesterol with two major components of the inner leaflet of the plasma membrane: Phosphatidylethanolamine and phosphatidylserine. *Biochemistry* **2008**, *47* (9), 3004-3012.
33. Lemaire-Ewing, S.; Prunet, C.; Montange, T.; Vejux, A.; Berthier, A.; Bessède, G.; Corcos, L.; Gambert, P.; Néel, D.; Lizard, G. Comparison of the cytotoxic, pro-oxidant and pro-inflammatory characteristics of different oxysterols. *Cell Biol. Toxicol.* **2005**, *21* (2), 97-114.
34. Leonarduzzi, G.; Poli, G.; Sottero, B.; Biasi, F. Activation of the mitochondrial pathway of apoptosis by oxysterols. *Front. Biosci.* **2007**, *12*, 791-799.
35. Phillips, J. E.; Geng, Y. J.; Mason, R. P. 7-Ketocholesterol forms crystalline domains in model membranes and murine aortic smooth muscle cells. *Atherosclerosis* **2001**, *159* (1), 125-135.
36. Niki, E. Lipid peroxidation: Physiological levels and dual biological effects. *Free Radical Biol. Med.* **2009**, *47* (5), 469-484.
37. Poirot, M.; Silvente-Poirot, S. Cholesterol-5,6-epoxides: Chemistry, biochemistry, metabolic fate and cancer. *Biochimie* **2013**, *95* (3), 622-631.
38. Pulfer, M. K.; Murphy, R. C. Formation of biologically active oxysterols during ozonolysis of cholesterol present in lung surfactant. *J. Biol. Chem.* **2004**, *279* (25), 26331-26338.
39. [http://en.wikipedia.org/wiki/Wikipedia:Featured\\_picture\\_candidates/Cell\\_membrane\\_\(diagrammatic\)#mediaviewer/File:Cell\\_membrane\\_detailed\\_diagram\\_en.svg](http://en.wikipedia.org/wiki/Wikipedia:Featured_picture_candidates/Cell_membrane_(diagrammatic)#mediaviewer/File:Cell_membrane_detailed_diagram_en.svg). [Online].
40. <http://www.intechopen.com/books/lipid-metabolism/overview-about-lipid-structure>.
41. Veldhuizen, E. J. A.; Batenburg, J. J.; van Golde, L. M. G.; Haagsman, H. P. The Role of Surfactant Proteins in DPPC Enrichment of Surface Films. *Biophys. J.* **2000**, *79* (6), 3164-3171.
42. Notter, R. H.; Taubold, R.; Mavis, R. D. Hysteresis in saturated phospholipid films and its potential relevance for lung surfactant function in vivo. *Exp. Lung Res.* **1982**, *3* (2), 109-127.
43. Hawco, M. W.; Davis, P. J.; Keough, K. M. W. Lipid fluidity in lung surfactant-monolayers of saturated and unsaturated lecithins. *J. Appl. Physiol.* **1981**, *51* (2), 509-515.

44. Lee, K. Y. C.; Lipp, M. M.; Zasadzinski, J. A.; Waring, A. J. Understanding the nature of interactions between lipids and engineered lung surfactant proteins for better replacement therapy. *Biophys. J.* **1997**, *72* (2), WP368-WP368.
45. Schurch, S.; Goerke, J.; Clements, J. A. Direct determination of surface-tension in lung. *Proc. Natl. Acad. Sci. U.S.A.* **1976**, *73* (12), 4698-4702.
46. Pastrana-Rios, B.; Taneva, S.; Keough, K. M.; Mautone, A. J.; Mendelsohn, R. External reflection absorption infrared spectroscopy study of lung surfactant proteins SP-B and SP-C in phospholipid monolayers at the air/water interface. *Biophys. J.* **1995**, *69* (6), 2531-2540.
47. Zhang, H.; Wang, Y. E.; Fan, Q.; Zuo, Y. Y. On the Low Surface Tension of Lung Surfactant. *Langmuir* **2011**, *27* (13), 8351-8358.
48. Zasadzinski, J. A.; Ding, J.; Warriner, H. E.; Bringezu, F.; Waring, A. J. The physics and physiology of lung surfactants. *Curr. Opin. Colloid Interface* **2001**, *6* (5-6), 506-513.
49. Schurch, S.; Qanbar, R.; Bachofen, H.; Possmayer, F. The surface-associated surfactant-reservoir in the alveolar lining. *Biology Neo* **1995**, *67*, 61-76.
50. Flach, C. R.; Cai, P.; Dieudonne, D.; Brauner, J. W.; Keough, K. M. W.; Stewart, J.; Mendelsohn, R. Location of structural transitions in an isotopically labeled lung surfactant SP-B peptide by IRRAS. *Biophys. J.* **2003**, *85* (1), 340-349.
51. Possmayer, F.; Keating, N.; Zuo, Y. Y.; Petersen, N. O.; Veldhuizen, R. A. Pulmonary Surfactant Reduces Surface Tension to Low Values near Zero through a Modified Squeeze-Out Mechanism. *Biophys. J.* **2012**, *102* (3, Supplement 1), 414a.
52. Kovacic, P.; Somanathan, R. Pulmonary Toxicity and Environmental Contamination: Radicals, Electron Transfer, and Protection by Antioxidants. *Revi. Environ. Contamina. Toxicol.* **2009**, *201*, 41-69.
53. Guardiola, F.; Codony, R.; Addis, P. B.; Rafecas, M.; Boatella, J. Biological effects of oxysterols: Current status. *Food Chem. Toxicol.* **1996**, *34* (2), 193-211.
54. Vallyathan, V.; Shi, X. The role of oxygen free radicals in occupational and environmental lung diseases. *Environ. Health Persp.* **1997**, *105* (SUPPL. 1), 165-177.
55. Klimenko, O. V.; Vobruba, V.; Martasek, P. Influence of the lung mechanical ventilation with injurious parameters on 7-ketocholesterol synthesis in Sus Scrofa. *BMB Reports* **2010**, *43* (4), 257-262.
56. Pulfer, M. K.; Taube, C.; Gelfand, E.; Murphy, R. C. Ozone exposure in vivo and formation of biologically active oxysterols in the lung. *J. Pharmacol. Exp. Ther.* **2005**, *312* (1), 256-264.
57. O'Callaghan, Y. C.; Woods, J. A.; O'Brien, N. M. Comparative study of the cytotoxicity and apoptosis-inducing potential of commonly occurring oxysterols. *Cell Biol. Toxicol.* **2001**, *17* (2), 127-137.
58. Kehrer, J. P. Free-radicals as mediators of tissue injury and disease. *Crit. Rev. Toxicol.* **1993**, *23* (1), 21-48.
59. Zuo, Y. Y.; Veldhuizen, R. A. W.; Neumann, A. W.; Petersen, N. O.; Possmayer, F. Current perspectives in pulmonary surfactant - Inhibition, enhancement and evaluation. *BBA - Biomembranes* **2008**, *1778* (10), 1947-1977.

60. McIntyre, R. C.; Pulido, E. J.; Bensard, D. D.; Shames, B. D.; Abraham, E. Thirty years of clinical trials in acute respiratory distress syndrome. *Crit. Care Med.* **2000**, *28* (9), 3314-3331.
61. <http://www.mayoclinic.com/health/ards/DS00944/DSECTION=causes>.
62. Ware, L. B.; Matthay, M. A. Medical progress - The acute respiratory distress syndrome. *New Engl. J. Med.* **2000**, *342* (18), 1334-1349.
63. Kopelman, A. E.; Mathew, O. P. Common respiratory disorders of the newborn. *Pediatr.* **1995**, *16* (6), 209-17.
64. <http://emedicine.medscape.com/article/165139-treatment>.
65. Sperber, J.; Lipcsey, M.; Larsson, A.; Sjolín, J.; Castegren, M. Lung Protective Ventilation Induces Immunotolerance and Nitric Oxide Metabolites in Porcine Experimental Postoperative Sepsis. *Plos One* **2013**, *8* (12).
66. O'Dowd, C. D.; De Leeuw, G. Marine aerosol production: a review of the current knowledge. *Philos. Trans. Roy. Soc. A* **2007**, *365* (1856), 1753-1774.
67. Rinaldi, M.; Decesari, S.; Finessi, E.; Giulianelli, L.; Carbone, C.; Fuzzi, S.; O'Dowd, C. D.; Ceburnis, D.; Facchini, M. C. Primary and Secondary Organic Marine Aerosol and Oceanic Biological Activity: Recent Results and New Perspectives for Future Studies. *Adv. Meteorology* **2010**.
68. O'Dowd, C. D.; Facchini, M. C.; Cavalli, F.; Ceburnis, D.; Mircea, M.; Decesari, S.; Fuzzi, S.; Yoon, Y. J.; Putaud, J. P. Biogenically driven organic contribution to marine aerosol. *Nature* **2004**, *431* (7009), 676-680.
69. Gill, P. S.; Graedel, T. E.; Weschler, C. J. Organic films on atmospheric aerosol-particles, fog, droplets, cloud droplets, raindrops and snowflakes. *Rev. Geophys.* **1983**, *21* (4), 903-920.
70. Donaldson, D. J.; Vaida, V. The influence of organic films at the air-aqueous boundary on atmospheric processes. *Chemical Reviews* **2006**, *106* (4), 1445-1461.
71. Ellison, G. B.; Tuck, A. F.; Vaida, V. Atmospheric processing of organic aerosols. *Journal of Geophysical Research-Atmospheres* **1999**, *104* (D9), 11633-11641.
72. McNeill, V. F.; Sareen, N.; Schwier, A. N. Surface-Active Organics in Atmospheric Aerosols. In *Atmospheric and Aerosol Chemistry*, McNeill, V. F.; Ariya, P. A., Eds., 2014; Vol. 339, pp 201-259.
73. Schmitt-Kopplin, P.; Liger-Belair, G.; Koch, B. P.; Flerus, R.; Kattner, G.; Harir, M.; Kanawati, B.; Lucio, M.; Tziotis, D.; Hertkorn, N.; Gebefuegi, I. Dissolved organic matter in sea spray: a transfer study from marine surface water to aerosols. *Biogeosciences* **2012**, *9* (4), 1571-1582.
74. Fu, P. Q.; Kawamura, K.; Chen, J.; Charriere, B.; Sempere, R. Organic molecular composition of marine aerosols over the Arctic Ocean in summer: contributions of primary emission and secondary aerosol formation. *Biogeosciences* **2013**, *10* (2), 653-667.
75. Tervahattu, H.; Juhanoja, J.; Vaida, V.; Tuck, A. F.; Niemi, J. V.; Kupiainen, K.; Kulmala, M.; Vehkamäki, H. Fatty acids on continental sulfate aerosol particles. *J. Geophys. Res-Atmos.* **2005**, *110* (D6).
76. Tervahattu, H.; Juhanoja, J.; Kupiainen, K. Identification of an organic coating on marine aerosol particles by TOF-SIMS. *J. Geophys. Res-Atmos.* **2002**, *107* (D16).

77. Brandsma, J.; Hopmans, E. C.; Philippart, C. J. M.; Veldhuis, M. J. W.; Schouten, S.; Damste, J. S. S. Low temporal variation in the intact polar lipid composition of North Sea coastal marine water reveals limited chemotaxonomic value. *Biogeosciences* **2012**, *9* (3), 1073-1084.
78. Gagosian, R. B.; Smith, S. O.; Nigrelli, G. E. Vertical transport of steroid alcohols and ketones measures in a sediment trap experiment in the equatorial atlantic ocean. *Geochim. Cosmochim. Ac.* **1982**, *46* (7), 1163-1172.
79. Barbier, M.; Tusseau, D.; Marty, J. C.; Saliot, A. Sterols in aerosols, surface microlayer and subsurface water in the northeastern tropical atlantic. *Oceanol. Acta* **1981**, *4* (1), 77-84.
80. Volkman, J. K. A review of sterol markers for marine and terrigenous organic matter. *Org. Geochem.* **1986**, *9* (2), 83-99.
81. Rontani, J.-F.; Charrière, B.; Sempéré, R.; Doxaran, D.; Vaultier, F.; Vonk, J. E.; Volkman, J. K. Degradation of sterols and terrigenous organic matter in waters of the Mackenzie Shelf, Canadian Arctic. *Org. Geochem.* **2014**, *75* (0), 61-73.
82. George, I. J.; Abbatt, J. P. D. Heterogeneous oxidation of atmospheric aerosol particles by gas-phase radicals. *Nat Chem* **2010**, *2* (9), 713-722.
83. Boggs, J. M. Intermolecular hydrogen-bonding between lipids: influence on the organization and function of lipids in membranes. *Can. J. Biochem.* **1980**, *58* (10), 755-770.
84. Wydro, P. The interactions between cholesterol and phospholipids located in the inner leaflet of humane erythrocytes membrane (DPPE and DPPS) in binary and ternary films-The effect of sodium and calcium ions. *Colloid Surface B* **2011**, *82* (1), 209-216.
85. Bruni, R.; Hernandez-Juviel, J. M.; Tanoviceanu, R.; Walther, F. J. Synthetic mimics of surfactant proteins B and C: In vitro surface activity and effects on lung compliance in two animal models of surfactant deficiency. *Mol. Genet. Metab.* **1998**, *63* (2), 116-125.
86. Li, X. M.; Momsen, M. M.; Smaby, J. M.; Brockman, H. L.; Brown, R. E. Cholesterol decreases the interfacial elasticity and detergent solubility of sphingomyelins. *Biochemistry* **2001**, *40* (20), 5954-5963.
87. Brezesinski, G.; Mohwald, H. Langmuir monolayers to study interactions at model membrane surfaces. *Adv. Colloid Interfac.* **2003**, *100*, 563-584.
88. Möhwald, H. Phospholipid monolayers. In *Handbook of Biological Physics*, R. Lipowsky, E. S., Ed.; Elsevier, (1995); Vol. 1, pp 161-211.
89. Guyot-sionnest, P.; Hunt, J. H.; Shen, Y. R. Sum-frequency vibrational spectroscopy of a langmuir film - study of monolayer-orientation of a two-dimensional system. *Phys. Rev. Lett.* **1987**, *59* (14), 1597-1600.
90. R.G. Dluhy; D.G. Cornell. In situ measurement of the infrared spectra of insoluble monolayers at the air/water interface. *J. Phys. Chem.* **1985**, *89*, 3195-3197.
91. Blaudez, D.; Buffeteau, T.; Cornut, J. C.; Desbat, B.; Escafre, N.; Pezolet, M.; Turllet, J. M. Polarization modulation FTIR spectroscopy at the air-water interface. *Thin Solid Films* **1994**, *242* (1-2), 146-150.
92. Weis, R. M.; McConnell, H. M. Two-dimensional chiral crystals of phospholipid. *Nature* **1984**, *310* (5972), 47-49.

93. Yu, H.; Hui, S. W. Methylation effects on the microdomain structures of phosphatidylethanolamine monolayers. *Chem. Phys. Lipids* **1992**, *62* (1), 69-78.
94. Wilkin, J.; Ping, Z.; Dluhy, R. A.; Weinbach, S.; Notter, R.; Losche, M. Spectroscopy & microscopy of aqueous lipid monolayers with applications to pulmonary surfactant: IR and fluorescence studies. *Biophys. J.* **1997**, *72* (2), MP271-MP271.
95. Sibug-Aga, R.; Dunn, R. C. High-resolution studies of lung surfactant collapse. *Photochem. Photobiol.* **2004**, *80* (3), 471-476.
96. Kjaer, K.; Alsn Nielsen, J.; Helm, C. A.; Laxhuber, L. A.; Mohwald, H. Ordering in lipid monolayers studied by synchrotron X-ray-diffraction and fluorescence. *Phys. Rev. Lett.* **1987**, *58* (21), 2224-2227.
97. Dutta, P.; Peng, J. B.; Lin, B.; Ketterson, J. B.; Prakash, M.; Georgopoulos, P.; Ehrlich, S. X-ray-diffraction studies of organic monolayers on the surface of water. *Phys. Rev. Lett.* **1987**, *58* (21), 2228-2231.
98. Ma, G.; Allen, H. C. DPPC Langmuir monolayer at the air-water interface: Probing the tail and head groups by vibrational sum frequency generation spectroscopy. *Langmuir* **2006**, *22* (12), 5341-5349.
99. Miller, C. E.; Busath, D. D.; Strongin, B.; Majewski, J. Integration of ganglioside GT(1b) receptor into DPPE and DPPC phospholipid monolayers: An x-ray reflectivity and grazing-incidence diffraction study. *Biophys. J.* **2008**, *95* (7), 3278-3286.
100. Dicko, A.; Bourque, H.; Pezolet, M. Study by infrared spectroscopy of the conformation of dipalmitoylphosphatidylglycerol monolayers at the air-water interface and transferred on solid substrates. *Chem. Phys. Lipids* **1998**, *96* (1-2), 125-139.
101. D. K. Chattoraj, K. S. B. *Adsorption and the Gibbs Surface Excess*; Plenum Press 1984.
102. Brown, T. E.; LeMay, H. H.; Bursten, B.; Murphy, C. *Chemistry: The Central Science* 11th ed.; Pearson Education, Inc. 2009.
103. Meunier, J. Why a Brewster angle microscope? *Colloids and Surfaces A : Physicochemical and Engineering Aspects* **2000**, *171*, 33-40.
104. Ducharme, D.; Max, J. J.; Salesse, C.; Leblanc, R. M. Ellipsometric study of the physical states of phosphatidylcholines at the air-water interface. *J. Phys. Chem.* **1990**, *94* (5), 1925-1932.
105. J. Peatross; Ware, M. *Physics of Light and Optics* 2008.
106. Lheveder, C.; Hénon, S.; Mercier, R.; Tissot, G.; Fournet, P.; Meunier, J. A new Brewster angle microscope. *Rev. Sci. Instrum.* **1998**, *69* (3), 1446-1450.
107. Zhuang, X.; Miranda, P. B.; Kim, D.; Shen, Y. R. Mapping molecular orientation and conformation at interfaces by surface nonlinear optics. *Physical Review B* **1999**, *59* (19), 12632-12640.
108. Verreault, D.; Hua, W.; Allen, H. C. From Conventional to Phase-Sensitive Vibrational Sum Frequency Generation Spectroscopy: Probing Water Organization at Aqueous Interfaces. *J. Phys. Chem. Lett.* **2012**, *3* (20), 3012-3028.
109. Velarde, L.; Zhang, X.-y.; Lu, Z.; Joly, A. G.; Wang, Z.; Wang, H.-f. Communication: Spectroscopic phase and lineshapes in high-resolution broadband sum frequency vibrational spectroscopy: Resolving interfacial inhomogeneities of "identical" molecular groups. *J. Chem. Phys.* **2011**, *135* (24), -.

110. Velarde, L.; Wang, H.-f. Unified treatment and measurement of the spectral resolution and temporal effects in frequency-resolved sum-frequency generation vibrational spectroscopy (SFG-VS). *Phys. Chem. Chem. Phys.* **2013**, DOI: 10.1039/C1033CP52577E.
111. Klopfer, K. J.; Vanderlick, T. K. Isotherms of dipalmitoylphosphatidylcholine (DPPC) monolayers: Features revealed and features obscured. *J. Colloid Interface Sci.* **1996**, 182 (1), 220-229.
112. Chattoraj, D. K.; Birdi, K. S. *Adsorption and the Gibbs Surface Excess*: New York 1984.
113. Kamel, A. M.; Felmeist, A.; Weiner, N. D. Surface pressure-surface area characteristics of a series of autoxidation products of cholesterol. *Lipid Res.* **1971**, 12 (2), 155-159.
114. Benvegnu, D. J.; McConnell, H. M. Surface dipole densities in lipid monolayers. *J. Phys. Chem.* **1993**, 97 (25), 6686-6691.
115. Dynarowicz-Latka, P.; Kita, K. Molecular interaction in mixed monolayers at the air/water interface. *Adv. Colloid Interface Sci.* **1999**, 79 (1), 1-17.
116. Chapman, D.; Owens, N. F.; Phillips, M. C.; Walker, D. A. Mixed monolayers of phospholipids and cholesterol. *Biochim. Biophys. Acta* **1969**, 183 (3), 458-465.
117. Kamal, M. A.; Raghunathan, V. A. Effect of ring-substituted oxysterols on the phase behavior of dipalmitoylphosphatidylcholine membranes. *Eur. Biophys. J. Biophys. Lett.* **2012**, 41 (10), 891-900.
118. Snik, A. F. M.; Kruger, A. J.; Joos, P. Dynamical behavior of monolayers of dipalmitoyl lecithin and cholesterol. *J. Colloid Interface Sci.* **1978**, 66 (3), 435-439.
119. McConlogue, C. W.; Malamud, D.; Vanderlick, T. K. Interaction of DPPC monolayers with soluble surfactants: electrostatic effects of membrane perturbants. *BBA-Biomembranes* **1998**, 1372 (1), 124-134.
120. Miñones, J.; Patino, J. M. R.; Conde, O.; Carrera, C.; Seoane, R. The effect of polar groups on structural characteristics of phospholipid monolayers spread at the air-water interface. *Colloids Surf. A-Physicochem. Eng. Aspects* **2002**, 203 (1-3), 273-286.
121. Hu, Y. F.; Lee, K. Y. C.; Israelachvili, J. Sealed minitrough for microscopy and long-term stability studies of Langmuir monolayers. *Langmuir* **2003**, 19 (1), 100-104.
122. Weis, R. M.; McConnell, H. M. Cholesterol stabilizes the crystal liquid interface in phospholipid monolayers. *Biophys. J.* **1985**, 47 (2), 4453-4459.
123. Yuan, C.; Johnston, L. J. Phase evolution in cholesterol/DPPC monolayers: atomic force microscopy and near field scanning optical microscopy studies. *J. Microsc.* **2002**, 205, 136-146.
124. Slotte, J. P.; Mattjus, P. Visualization of lateral phases in cholesterol and phosphatidylcholine monolayers at the air/water interface - A comparative-study with two different reporter molecules. *BBA-Lipid Lipid Met.* **1995**, 1254 (1), 22-29.
125. Su, Y.; Li, Q.; Chen, L.; Yu, Z. Condensation effect of cholesterol, stigmaterol, and sitosterol on dipalmitoylphosphatidylcholine in molecular monolayers. *Colloids Surf. A-Physicochem. Eng. Aspects* **2007**, 293 (1-3), 123-129.

126. Berring, E. E.; Borrenpohl, K.; Fliesler, S. J.; Serfis, A. B. A comparison of the behavior of cholesterol and selected derivatives in mixed sterol-phospholipid Langmuir monolayers: a fluorescence microscopy study. *Chem. Phys. Lipids* **2005**, *136* (1), 1-12.
127. McConnell, H. M.; Radhakrishnan, A. Condensed complexes of cholesterol and phospholipids. *Biochim. Biophys. Acta.* **2003**, *1610* (2), 159-173.
128. de Meyer, F.; Smit, B. Effect of cholesterol on the structure of a phospholipid bilayer. *Proc. Natl. Acad. Sci. U.S.A.* **2009**, *106* (10), 3654-3658.
129. Smondryev, A. M.; Berkowitz, M. L. Effects of oxygenated sterol on phospholipid bilayer properties: a molecular dynamics simulation. *Chem. Phys. Lipids* **2001**, *112* (1), 31-39.
130. Sabatini, K.; Mattila, J.-P.; Kinnunen, P. K. J. Interfacial behavior of cholesterol, ergosterol, and lanosterol in mixtures with DPPC and DMPC. *Biophys. J.* **2008**, *95* (5), 2340-2355.
131. Dynarowicz-Latka, P.; Hac-Wydro, K. Interactions between phosphatidylcholines and cholesterol in monolayers at the air/water interface. *Colloid Surface B* **2004**, *37* (1-2), 21-25.
132. Davies, J. T.; Rideal, E. K. *Interfacial phenomena*; 2nd ed.; Academic Press, New York 1963.
133. Aittoniemi, J.; Róg, T.; Niemelä, P.; Pasenkiewicz-Gierula, M.; Karttunen, M.; Vattulainen, I. Tilt: Major factor in sterols' ordering capability in membranes. *J. Phys. Chem. B* **2006**, *110* (51), 25562-25564.
134. Loomis, C. R.; Shipley, G. G.; Small, D. M. Phase behavior of hydrated cholesterol. *J. Lipid Res.* **1979**, *20* (4), 525-535.
135. Rapaport, H.; Kuzmenko, I.; Lafont, S.; Kjaer, K.; Howes, P. B.; Als-Nielsen, J.; Lahav, M.; Leiserowitz, L. Cholesterol monohydrate nucleation in ultrathin films on water. *Biophys. J.* **2001**, *81* (5), 2729-2736.
136. Craven, B. M. Crystal structure of cholesterol monohydrate. *Nature* **1976**, *260* (5553), 727-729.
137. McCourt, M. P.; Ashraf, K.; Miller, R.; Weeks, C. M.; Li, N. Y.; Pangborn, W.; Dorset, D. L. X-ray crystal structure of cytotoxic oxidized cholesterol: 7-ketocholesterol and 25-hydroxycholesterol. *J. Lipid Res.* **1997**, *38* (5), 1014-1021.
138. McConnell, H. M. Structures and transitions in lipid monolayers at the air-water interface. *Annu. Rev. Phys. Chem.* **1991**, *42*, 171-195.
139. Keller, D. J.; McConnell, H. M.; Moy, V. T. Theory of superstructures in the lipid monolayer phase transitions. *J. Phys. Chem.* **1986**, *90* (11), 2311-2315.
140. Somerharju, P.; Virtanen, J. A.; Cheng, K. H.; Hermansson, M. The superlattice model of lateral organization of membranes and its implications on membrane lipid homeostasis. *Biochim. Biophys. Acta* **2009**, *1788* (1), 12-23.
141. Huang, J. Y.; Feigenson, G. W. A microscopic interaction model of maximum solubility of cholesterol in lipid bilayers. *Biophys. J.* **1999**, *76* (4), 2142-2157.
142. Ohvo-Rekila, H.; Ramstedt, B.; Leppimäki, P.; Slotte, J. P. Cholesterol interactions with phospholipids in membranes. *Progress in Lipid Research* **2002**, *41* (1), 66-97.

143. Massey, J. B. Membrane and protein interactions of oxysterols. *Curr. Opin. Lipidol.* **2006**, *17* (3), 296-301.
144. Mabrey, S.; Sturtevant, J. M. Investigation of phase transitions of lipids and lipid mixtures by high sensitivity differential scanning calorimetry. *P. Natl. Acad. Sci. USA* **1976**, *73* (11), 3862-3866.
145. Mannock, D. A.; Lewis, R. N. A. H.; McMullen, T. P. W.; McElhaney, R. N. The effect of variations in phospholipid and sterol structure on the nature of lipid-sterol interactions in lipid bilayer model membranes. *Chem. Phys. Lipids* **2010**, *163* (6), 403-448.
146. McMullen, T. P. W.; Lewis, R.; McElhaney, R. N. Differential scanning calorimetric study of the effect of cholesterol on the thermotropic phase behavior of a homologous series of linear saturated phosphatidylcholines. *Biochemistry* **1993**, *32* (2), 516-522.
147. Khelashvili, G.; Pabst, G.; Harries, D. Cholesterol orientation and tilt modulus in DMPC bilayers. *J. Phys. Chem. B* **2010**, *114* (22), 7524-7534.
148. Wallace, E. J.; Hooper, N. M.; Olmsted, P. D. Effect of hydrophobic mismatch on phase behavior of lipid membranes. *Biophys. J.* **2006**, *90* (11), 4104-4118.
149. Pandit, S. A.; Bostick, D.; Berkowitz, M. L. Complexation of phosphatidylcholine lipids with cholesterol. *Biophys. J.* **2004**, *86* (3), 1345-1356.
150. Veatch, S.; Polozov, I.; Gawrisch, K.; Keller, S. Liquid domains in vesicles investigated by NMR and fluorescence microscopy. *Biophys. J.* **2004**, *86* (5), 2910-2922.
151. Bagatolli, L. A.; Gratton, E. A correlation between lipid domain shape and binary phospholipid mixture composition in free standing bilayers: A two-photon fluorescence microscopy study. *Biophys. J.* **2000**, *79* (1), 434-447.
152. Ma, G.; Allen, H. C. Condensing effect of palmitic acid on DPPC in mixed Langmuir monolayers. *Langmuir* **2007**, *23* (2), 589-597.
153. Velarde, L.; Wang, H.-f. Capturing inhomogeneous broadening of the -CN stretch vibration in a Langmuir monolayer with high-resolution spectra and ultrafast vibrational dynamics in sum-frequency generation vibrational spectroscopy (SFG-VS). *J. Chem. Phys.* **2013**, *139* (8).
154. Kett, P. J. N.; Casford, M. T. L.; Davies, P. B. Structure of Mixed Phosphatidylethanolamine and Cholesterol Monolayers in a Supported Hybrid Bilayer Membrane Studied by Sum Frequency Generation Vibrational Spectroscopy. *J. Phys. Chem. B* **2011**, *115* (20), 6465-6473.
155. Kett, P. J.; Casford, M. T.; Davies, P. B. Sum Frequency Generation Vibrational Spectroscopy of Cholesterol in Hybrid Bilayer Membranes. *J. Phys. Chem. B* **2013**, *117* (21), 6455-6465.
156. Liu, J.; Conboy, J. C. Phase behavior of planar supported lipid membranes composed of cholesterol and 1, 2-distearoyl-sn-glycerol-3-phosphocholine examined by sum-frequency vibrational spectroscopy. *Vib. Spectrosc.* **2009**, *50* (1), 106-115.
157. Ma, S.; Li, H.; Tian, K.; Ye, S.; Luo, Y. In Situ and Real-Time SFG Measurements Revealing Organization and Transport of Cholesterol Analogue 6-Ketocholestanol in a Cell Membrane. *J. Phys. Chem. Lett.* **2014**, *5* (3), 419-424.

158. Alwarawrah, M.; Dai, J.; Huang, J. A molecular view of the cholesterol condensing effect in DOPC lipid bilayers. *J. Phys. Chem. B* **2010**, *114* (22), 7516-7523.
159. Smondyrev, A. M.; Berkowitz, M. L. Structure of dipalmitoylphosphatidylcholine/cholesterol bilayer at low and high cholesterol concentrations: molecular dynamics simulation. *Biophys. J.* **1999**, *77* (4), 2075-2089.
160. Oldfield, E.; Meadows, M.; Rice, D.; Jacobs, R. Spectroscopic studies of specifically deuterium labeled membrane systems. Nuclear magnetic resonance investigation of the effects of cholesterol in model systems. *Biochemistry* **1978**, *17* (14), 2727-2740.
161. Kett, P.; Casford, M.; Davies, P. Orientation of cholesterol in hybrid bilayer membranes calculated from the phases of methyl resonances in sum frequency generation spectra. *J. Chem. Phys.* **2013**, *138* (22), 225101.
162. Hirose, C.; Yamamoto, H.; Akamatsu, N.; Domen, K. Orientation analysis by simulation of vibrational sum frequency generation spectrum: CH stretching bands of the methyl group. *J. Phys. Chem.* **1993**, *97* (39), 10064-10069.
163. Wang, H.-F.; Gan, W.; Lu, R.; Rao, Y.; Wu, B.-H. Quantitative spectral and orientational analysis in surface sum frequency generation vibrational spectroscopy (SFG-VS). *Int. Rev. Phys. Chem.* **2005**, *24* (2), 191-256.

## APPENDIX

### Appendix A BAM Images of Mixed DPPC/Sterols Monolayers

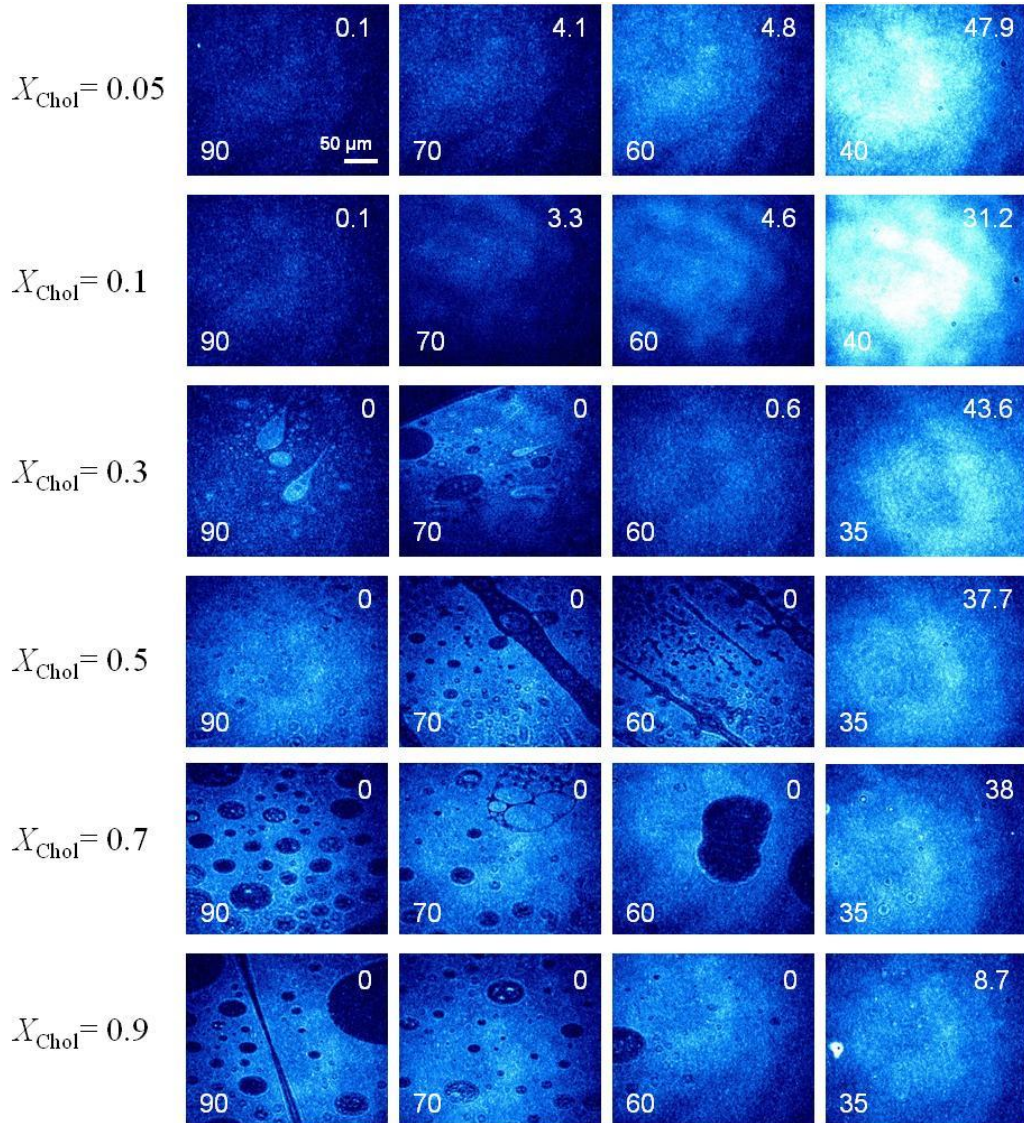


Figure A.1 BAM images of a DPPC monolayer mixed with Chol at different stages of compression. Numbers in the lower left and upper right corners indicate the mean molecular and the surface pressure, respectively.

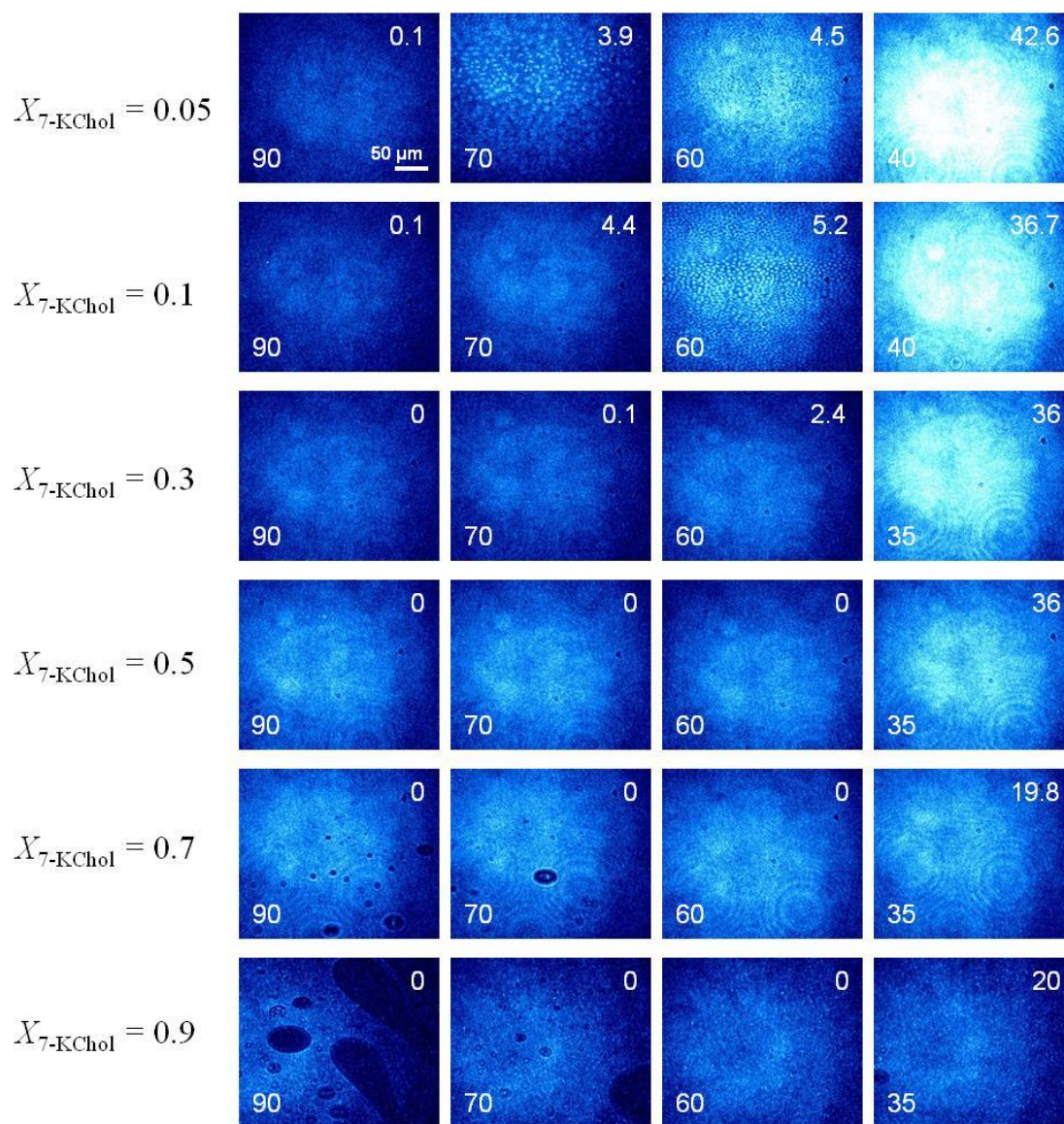


Figure A.2 BAM images of a DPPC monolayer mixed with 7-KChol at different stages of compression. Numbers in the lower left and upper right corners indicate the mean molecular and the surface pressure, respectively.

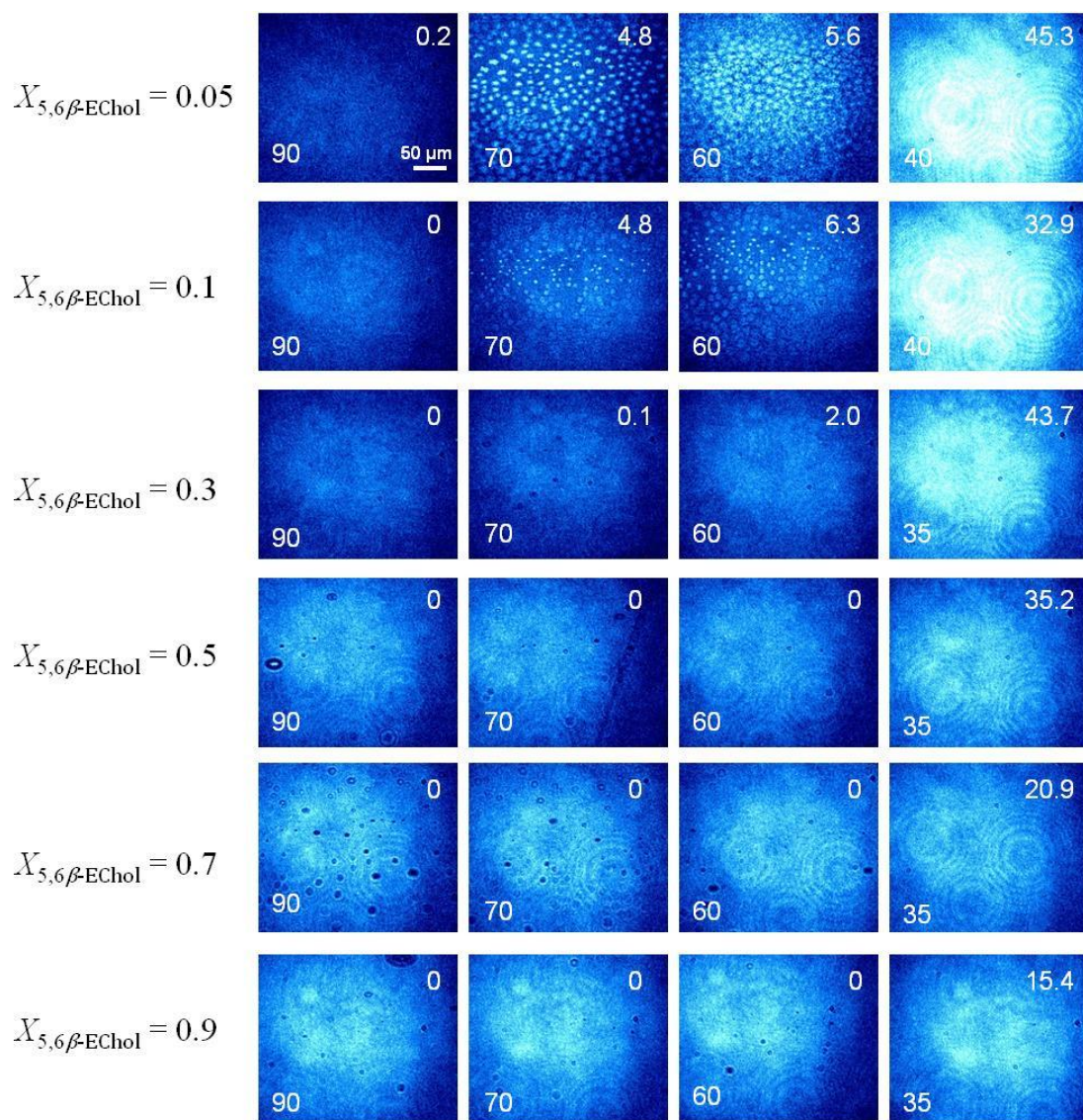


Figure A.3 BAM images of a DPPC monolayer mixed with 5,6 $\beta$ -EChol at different stages of compression. Numbers in the lower left and upper right corners indicate the mean molecular and the surface pressure, respectively.

Appendix B BAM Images of Mixed DLPC and DMPC/5,6 $\beta$ -EChol Monolayers

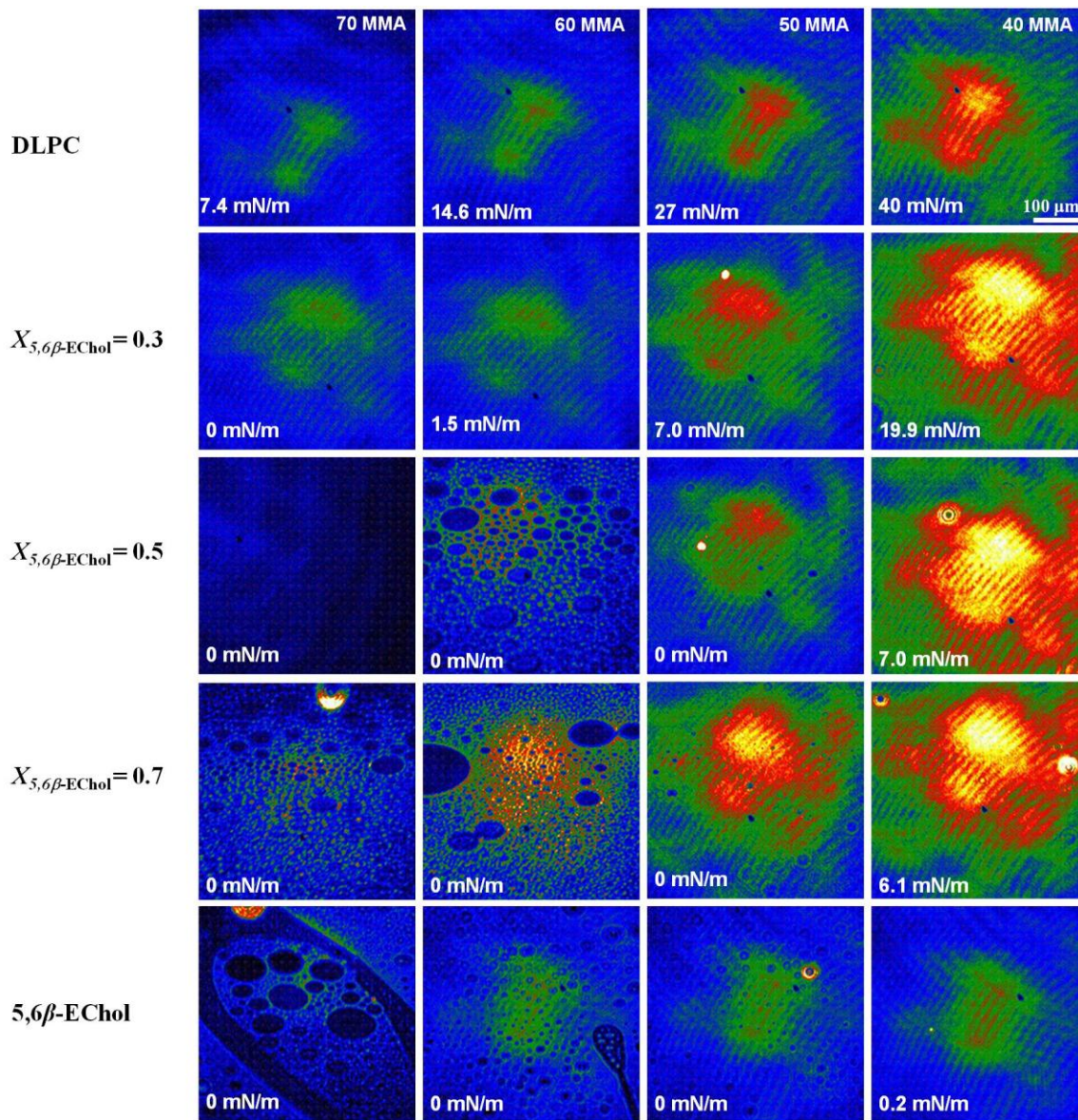


Figure B.1 BAM images of DLPC and DLPC/5,6 $\beta$ -EChol monolayers with  $X_{5,6\beta\text{-EChol}} = 0.3\text{--}0.5$  and Chol at different stages of compression. Numbers in the lower left and upper right corners indicate the mean molecular area and the surface pressure, respectively.

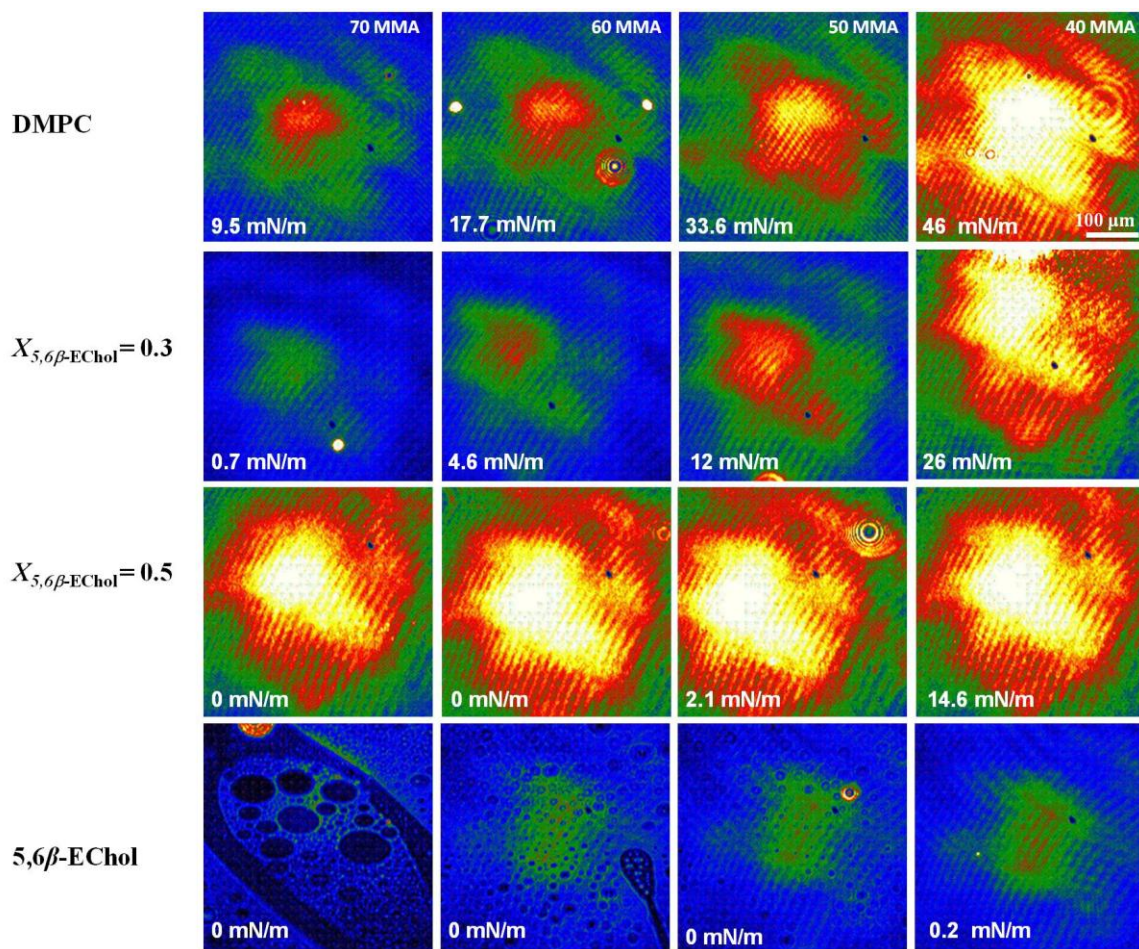


Figure B.2 BAM images of DMPC and DMPC/5,6 $\beta$ -EChol monolayers with  $X_{5,6\beta\text{-EChol}} = 0.3$ – $0.5$  and Chol at different stages of compression. Numbers in the lower left and upper right corners indicate the mean molecular area and the surface pressure, respectively.